The Dissertation Committee for Juntao Yuan
certifies that this is the approved version of the following dissertation:

Unification of QSOs via Black Hole and Accretion Properties

Committee:

Beverley J. Wills, Supervisor

Neal J. Evans II, Supervisor

Gregory A. Shields

Derek Wills

Ari Laor

Unification of QSOs via Black Hole and Accretion Properties

by

Juntao Yuan, B.S., M.A.

DISSERTATION

Presented to the Faculty of the Graduate School of

The University of Texas at Austin

in Partial Fulfillment

of the Requirements

for the Degree of

DOCTOR OF PHILOSOPHY

THE UNIVERSITY OF TEXAS AT AUSTIN

August 2004

To my wife Ju,
my sister Joan, my mother Mary
and my late father ChengChang

Acknowledgments

This thesis is the result of many people's hard work. First of all, I want to thank my advisor Dr. Bev Wills for her clear scientific vision to start this project and relentless pursue of the truth in the process. Bev and I first met in Shanghai in 1996, where she introduced me to the wonderful world of Active Galactic Nuclei (AGN). In the following 7 years, she has guided me through several AGN related research projects including this one. Bev's vision has put us at the forefront of the international AGN research. When I encounter difficulties, Bev encourages me to think creatively and critically, but she has always insisted on the highest possible standards when it comes to the scientific results. Bev made sure that this thesis will pass the test of time and she is the true hero behind this project. From Bev, I learned the essential knowledge of astrophysics, the scientific method and the skill of critical thinking. Even if I might not continue to work in the field of astrophysics, the positive altitude and skills Bev passed on to me will serve me well in the future. So, thank you, Bev.

My committee members also provided very valuable input to the thesis. Dr. Neal Evans, my co-supervisor, helped guide me through the important scientific questions and made sure that I met various deadlines leading to the defense of the thesis. Dr. Greg Shields helped me with the important theoretical background of the thesis and had a lot discussion with me about the observational results. Dr. Ari Laor is a world leading expert in my thesis field. He gave valuable comments to my manuscript and clarified some confusing

Unification of QSOs via Black Hole and Accretion Properties

Publication No. _____

Juntao Yuan, Ph.D.
The University of Texas at Austin, 2004

Supervisors: Beverley J. Wills
               Neal J. Evans II

Although the orientation-based AGN unification scheme can success-fully explain many QSO observational phenomena, orientation does not ad-dress all the object-to-object differences in QSOs. Physical differences of the underlying engine, such as luminosity, black hole mass (M_{BH}) and Eddington ratio (L/L_{Edd}), are crucial to our understanding of QSO central engines. Broad Absorption Line (BAL) QSOs are a particularly interesting type of QSO that exhibits both orientation and intrinsic property-related observational features. In this thesis, I studied a large QSO sample, including 16 BAL QSOs at $z \sim 2$, with new spectroscopy data for the Hβ region. This sample covers a luminosity range substantially wider than similar studies in the past and hence enables us to differentiate luminosity from other underlying mechanisms driving QSO observational properties.

I found that overall, QSOs accrete at close to Eddington rate. Due to the narrow range of L/L_{Edd}, the QSO luminosity is almost directly propor-tional to the M_{BH}. The slight increase of L/L_{Edd} at high luminosity suggests

that the QSO M_{BH} distribution has a high mass cut-off near $10^9 M_{\odot}$. Compared with radio quiet QSOs, radio loud QSOs tend to have higher M_{BH} for the same luminosity. The [O III] versus Fe II anti-correlation discovered from low luminosity QSOs (BGEV1) extends to high luminosity objects with BAL QSOs at the weak [O III] strong Fe II end of the trend, and radio loud QSOs at strong [O III] weak Fe II end of the trend. Both [O III] and Fe II strengths are well correlated with L/L_{Edd} over the entire luminosity range, indicating that L/L_{Edd} is the physical driver behind the BGEV1 correlations. Although BAL QSOs have higher L/L_{Edd} than most QSOs, they do not stand out when compared with high luminosity non-BAL QSOs. One interpretation is that [O III] and Fe II are indirectly linked to L/L_{Edd} via the availability of accretion fuel. Even with the expanded luminosity coverage, I could not confirm the existence of an Hβ Baldwin Effect. An [O III] "Baldwin Effect" is observed, suggesting a limited amount of [O III] NLR gas in all QSO systems.

Table of Contents

List of Tables

List of Figures

xvi

Chapter 1

Introduction

Quasi-stellar objects (QSOs)[1] are among the most luminous objects in the universe. They are characterized by large luminosity ($M_B < -21.5 + 5 \log h_0$ and/or $\geq 10^{44}$ erg/s), star-like appearance and very broad spectral energy distributions (SEDs) from X-ray to radio (Peterson 1997). The continua of many QSOs can vary 0.3 to 0.5 mags in several months or even days (e.g. Smith and Hoffleit 1963). Such variability suggests that QSO's continuum source can be as small as a few light-days — much smaller than one parsec.

Several physical models for the QSO central engine, including the nuclear starburst model (Terlevich et al. 1992) and super-massive black hole model, have been developed to account for the large luminosity in such small volume. Currently, the black hole model can best explain most of the observed phenomena and hence is most widely accepted by QSO researchers (e.g. Peterson 1997). We will focus on the black hole model exclusively in this research. In this model, QSOs are active galactic nuclei (AGNs) with super-massive ($\sim 10^8 M_\odot$) black holes in the middle. A hot accretion disk surrounding a super-massive black hole can provide the energy source for QSOs. When the

---

[1] Note that the terms "QSO" and "quasar" are virtually interchangeable in this thesis, although historically, quasar refers to radio selected quasi-stellar objects, and QSO refers to optically-selected objects. I will use "radio-loud" or "radio-quiet" to specify their radio properties when needed (see definition later).

gas materials in the accretion disk fall into the black hole, the gravitational energy is converted to radiative energy. To understand the inner working of the QSO central engine is a major challenge in astronomical research. Important research questions on this topic include the following:

- Is there a characteristic black hole mass or accretion rate that triggers QSO activity?

- What are the geometry and structure of the accretion flow?

- Where are the sources of the accretion fuel?

- What are the location and physical conditions of the accreting fuel?

- What is the outflow's origin, geometry and structure?

- How do the radiation and magnetic fields interact with the inflow and outflow?

The answers to these questions are not only important in QSO research, they could help advance our understanding of other astronomy fields, such as those listed below, as well.

- Since QSOs are mostly discovered at high redshifts and our nearby galaxies (e.g., the Milky Way Galaxy itself) have dormant super-massive black holes in the middle (Eckart and Genzel 1997; Genzel, Eckart, Ott and Eisenhauer 1997), it has been suggested that the active black hole is one stage of galaxy evolution (Marconi, Risaliti, Gilli, Hunt et al. 2004). From knowledge of the accretion process and fuel supply, we can study how and when the accretion is turned on or off. We could further link

observable parameters to evolution stages. This allows us to study early evolution of galaxies, and possibly the origin and growth of super-massive black holes.

- If we can understand the physics of QSO central engine and find a way to figure out QSO luminosity from other spectral properties, we can use QSOs as standard candles to measure cosmological distances to very high redshift.

In this research project, we will compile a sample of QSOs with diverse observational characteristics (e.g., different continuum shapes and spectral features). We will use recently developed diagnostic methods to derive their physical properties such as the black hole mass and accretion rate using data from the literature or new observations. Then, we will investigate how the intrinsic physical properties affect QSOs' observational appearances. Our goal is to understand and constrain the physical processes in QSO central engines.

1.1 QSO Observational Properties

1.1.1 The Continuum Source

The overall SED of QSOs span over a wide range of wavelengths and can be crudely characterized by a powerlaw function, which indicates non-thermal radiation.

$$F_\nu \propto \nu^\alpha$$

The spectral index α for most QSOs is in the range of -1 to 0 (Peterson 1997). The overall non-thermal SED differentiates QSOs from stars

and other thermal sources observationally. However, thermal emission can still contribute a lot to some QSO spectral regions locally. Elvis et al. (1994) gives an atlas of SEDs for normal UV selected QSOs. The QSO continuum shape gives us insight into the emission mechanism of the central engine.

For most QSOs, the radiation energy distribution peaks in the UV-optical band. A typical QSO emits one third of its total bolometric energy between 1.2 μm and 800Å (Laor and Draine 1993). Almost another 25% of the bolometric energy comes from the far-UV (shortward of 800Å to 0.4 keV) region although the exact SED shape of this region is unclear. Vanden Berk et al. (2001) studied QSO composite spectra from a large sample of Sloan Digital Sky Survey (SDSS) QSOs. Regardless of their luminosity, redshift and radio properties, all optically selected QSOs have remarkably similar continuum shapes in the UV-optical spectral region. The UV-optical spectral shape can be approximated by a broken powerlaw function. The two powerlaw components cover a wavelength range from 1300 Å to 8555 Å (redward of Lyα) and join each other at 5000 Å. To the blue the spectral index is $\alpha_\nu = -0.44$ and to the red the spectral index is $\alpha_\nu = -2.45$ (Vanden Berk et al. 2001). The abrupt change of slope in the red component is explained by the combination of hot dust and contamination of star light in the host galaxy.

On top of the underlying blue powerlaw continuum, a very broad spectral feature, known as the "Big Blue Bump", dominates the spectral region shortward of 4000 Å (Shields 1978). The high energy tail of the Big Blue Bump might extend to as far as the soft X-ray spectral region. The Big Blue Bump is probably a result of thermal radiation from the accretion disk with a black body temperature in the order of 10^5 K. On top of the big blue bump between $\sim 2000 - 4000$Å, there is a weaker emission feature known as the

"small blue bump". The small blue bump is thought to be a mix of Balmer continuum and many Fe II emission lines belended together.

A typical QSO emits another one third of its bolometric luminosity in the infrared band between 1.2 μm and 100 μm (Laor and Draine 1993). On top of the underlying continuum, the infrared SED is characterized by a bump to the redward of 1 μm. The continuum (in νF_ν) reaches a minimum at 1 μm where the infrared bump joins the UV-optical part of the spectrum (Peterson 1997). The infrared bump, peaked at 3 μm, suggests a thermal component with black body temperature of $T \leq 2000$ K, which signals the existence of warm dust grains in the QSOs.

QSOs are among the most luminous X-ray emission sources in the universe although the X-ray flux between 0.4 keV to 12 keV range only accounts for less than 10% of the total luminosity (Laor and Draine 1993). QSOs emit in both soft and hard X-ray bands. In the soft X-ray region (below 1 keV), there is a sharp rise toward the UV big blue bump. That feature is known as the "soft X-ray excess" and it is thought to originate from high-energy Compton scattering of big blue bump photons.

The radio power of QSOs is much weaker than in the higher energy bands. Radio flux between 1 cm to 10 cm accounts for less than 1% of the total bolometric luminosity even for radio loud QSOs (Elvis et al. 1994). Radio loud QSOs are defined to have specific flux ratio density between 5 GHz and 4400 Å in the rest frame, R^*, greater than 10 (Sramek and Weedman 1978; Kellermann et al. 1989).

$$R^* \equiv \frac{F_\nu(5\text{GHz})}{F_\nu(4400\text{Å})} > 10$$

Radio-loud and radio-quiet QSOs have comparable energy output in UV, optical and IR bands, but differ by a few orders of magnitude in radio power. The QSO radio spectrum is characterized by a powerlaw and originates from synchrotron radiation.

The composite SED described above applies to the majority of optically selected radio loud and radio quiet QSOs. There are QSOs that do not conform to the average SED. For example, BL Lac objects and blazars can have very strong synchrotron radiation in the radio and to the optical bands; some QSOs have reddened continua indicating obscuring dusty gas; some QSOs are very luminous in the infrared bands suggesting large amount of warm dust in the system; For low luminosity AGNs, the host galaxy star light might also contaminate the near infrared part of the continuum. In addition, QSO continuum flux is known to vary in the time scale of several days or weeks. Objects with strong synchrotron radiation components tend to be more variable.

1.1.2   Radio Morphology and Spectral Characteristics

Although QSOs have star-like appearance in the UV-optical band, their radio emission is much more extended (up to Mpcs in physical scale) and can be resolved by radio telescopes. The resolved radio structures give us insights into the physical structure of the QSO central engine. With the milli-arcsecond resolution VLBI technologies, we can peek into the QSO central engine at a scale of several parsecs (assuming $z \sim 0.5$). Such resolution is impossible with UV-optical observations. QSOs, and AGNs in general, have two radio morphological types: lobe dominant and core dominant. Like the QSO overall SED, QSOs' radio spectra are characterized by powerlaw distributions. It is consistent with the hypothesis that the mechanism for radio emission is

synchrotron radiation. Different QSO radio morphological type corresponds to different powerlaw spectral index α.

- The radio maps for some objects are dominated by two extended lobes symmetrically distributed about a weak central core. The separation of the lobes could be many arcminutes corresponding to Mpc scale structure in a $z \sim 0.5$ system. For some lobe dominant objects, we can see two jets connecting the core to the lobes (FR I type); for others, we can only see a one-sided jet (FR II type). The outer edges of the lobes in FR II objects are brightened and show hot-spots. FR II objects generally have higher luminosity ($\geq 10^{23}$ W at centimeter wavelengths) than FR I objects. For the integrated radio spectra from the entire object structure, including lobes, jets and the core, the lobe dominant QSOs typically have steep radio spectral index $\alpha < -0.5$ at the rest frame 5 GHz.

- The radio maps for other radio loud QSOs are dominated by a strong compact core unresolved at the arcsecond scale. They often show strong one-sided jet at the arcsecond scale as well. High resolution radio maps from VLBI can resolve the core itself into a jet at milli-arcsecond scale. The milli-arcsecond jet is typically aligned with or perpendicular to the arcsecond scale jet. Further analysis shows that optical polarization angle is typically aligned with milli-arcsecond scale radio jet. The core dominant QSOs typically have flat radio spectral index $\alpha > -0.5$ for the integrated spectrum at rest frame 5 GHz.

There is strong observational evidence to support that the jets in core dominant objects are relativistically beamed toward our line-of-sight.

- VLBI observations have found that components in the milli-arcsecond scale jet in core dominant sources move at an apparent speed faster than the speed of the light in the projected sky plane. The apparent superluminal motion could be explained by relativistic motion close to the line-of-sight. Photons emitted at time t_1 and t_2 would arrive earth in an interval much smaller than $t_2 - t_1$ since the light emitting material has moved closer to earth by t_2 and the second photon needs to travel less distance to reach us.

- The continuum flux of core dominant objects varies much faster than lobe dominant objects. That is consistent with the time abbreviation effect caused by a highly beamed jet.

- In core dominant objects, only one side of the jet is visible. That is consistent with the hypothesis that the other side of jet is beaming away from us.

- The small size of jets in core dominant objects is consistent with the less projection onto the sky plane

1.1.3 Emission Lines

The most prominent features in the UV-optical spectral region are emission lines. Except for a small number of BL Lac objects, all QSOs show strong emission lines, which are thought to arise from gas photoionized by the continuum. There are two types of QSO emission lines.

1.1.3.1 Broad Emission Lines

Most QSO emission lines are broad with a typical full width half maximum (FWHM) of ~ 5000 km s^{-1}. Some broad emission lines could be as broad as a few times 10^4 km s^{-1}. All broad lines are permitted or semi-forbidden lines, such as Balmer lines, Lyα, N v, He ii, C iv, C iii], UV and optical Fe ii lines and many other lines. Some lines, such as the Lyα and N v pair, and the Hβ and the optical Fe ii complex, are heavily blended.

It is known that QSO broad line intensity changes with the continuum level with a time lag. That indicates a causal relationship between the continuum and the line, and supports the hypothesis that the broad lines are emitted by gas photoionized by the central continuum source. The time lag indicates the distance light has to travel from the continuum source to the BLR. AGN reverberation mapping projects monitor low redshift AGNs over several months to several years in order to calculate BLR sizes for various emission lines. The results show that high ionization lines originate closer to the center (several light days) than the low ionization lines (tens of light-days). That is consistent with the photoionization assumption. Peterson and Wandel (1999) also found that the broad line width increases with the shorter lags. That is consistent with the hypothesis that gas in the BLR is bound by the gravitational field of the central black hole.

Since C iii] $\lambda 1909$ is among the broad lines while [O iii] is not, critical density analysis of those two semi-forbidden and forbidden lines indicates that the BLR density is of order 10^{10} cm^{-3}. However, recent models based on reverberation mapping studies, indicated that the BLR might have multiple zones each with different densities. The zone for the broad semi-forbidden C iii] line has lower density than the permitted line zones in the BLR. Based

on data from NGC 5548, Ferland et al. (1992) calculated the electron density the Lyα and C IV BLR zone to be $\sim 10^{11}$ cm^{-3}. Because it is photoionized, the temperature of the BLR is in the order of 10^4 K.

Statistical analysis of the broad line profiles has also suggested that the BLR might have velocity structure. Broad UV emission lines appear to be composed of two profiles: a component with width ~ 2000 km s^{-1} and a component with width as large as ≥ 7000 km s^{-1}. The second component could be blueshifted by ≥ 1000 km s^{-1}. It has been suggested that the two components are emitted from different physical zones inside the traditional BLR (Brotherton, Wills, Francis and Steidel 1994). It has been suggested that the components of the Hβ broad line vary in relative strength and/pr width from object to object (Shang et al. 2003).

The total mass of the line emitting gas in the BLR can be calculated from the line luminosity. It is much smaller than the product of the BLR density and the BLR volume which is calculated from the reverberation mapping size. The "filling factor", which indicates how much of the BLR volume is filled with line emitting gas, is estimated to be around 10^{-6} (e.g. Netzer 1990). There are two kinds of models to describe the physical states of the BLR emitting gas.

- The broad line emitting gas could exist in numerous small clumps (BLR clouds). Since each of those clouds has mass of only $10^{-7} M_\odot$, it can not be held together by self-gravity. Some external confinement, such as a hot intercloud medium (Krolik, McKee and Tarter 1981) or magnetic field (Rees 1987), is necessary to avoid the evaporation of the clouds. Currently, no confinement model is widely accepted. The smooth profile

of the broad line requires a large number of discrete clouds. Using high resolution spectral data, it has been estimated that $\sim 10^8$ clouds are needed to produce the smooth Balmer broad line profiles (Arav et al. 1998; Dietrich et al. 1999). The large number of BLR clouds required eliminates one type of models which hypothesizes that the clouds are bloated stars (Alexander and Netzer 1994).

- An alternative model for the BLR is that the emission gas is continuous and embedded inside a hydrodynamic flow, such as the radiatively driven wind from the accretion disk (e.g. Murray, Chiang, Grossman and Voit 1995; Murray and Chiang 1997). Arav et al. (1998) and Dietrich et al. (1999) did not detect any cross-correlation micro-structure between Hα and Hβ emission lines. That is consistent with the continuous flow of emission line gas in disk wind models. But perhaps the biggest advantage of the disk wind model is its ability to explain both the emission line and absorption line features in QSO spectra (see section 1.1.4).

Although the BLR gas can exist in a variety of physical states (e.g., density and temperature), photoionization calculations have shown that given an input ionizing continuum, only the BLR gas within a narrow range of physical parameters can emit line photons efficiently and dominate the observed emission line flux (Baldwin, Ferland, Korista and Verner 1995). The broad emission line relative intensities are determined by the shape of the ionizing continuum and the gas metallicity, and less by the actual distribution of physical conditions inside the BLR (Korista, Baldwin and Ferland 1998). That strong selection effect of the emitting gas conditions explains the apparent similarity in BLR parameters derived from line observations.

11

1.1.3.2 Narrow Emission Lines

The narrow emission lines in QSO spectra typically have FHWM of $200 - 900$ km s^{-1}. The strongest narrow emission lines in QSO UV-optical spectrum are the [O III] $\lambda\lambda$4959,5007 forbidden lines. The [N II] $\lambda\lambda$6548, 6583 and [S II] $\lambda\lambda$6716, 6731 lines are also sometimes detectable although they are often blended with the broad Hα line. Permitted lines, such as Balmer lines, can also be narrow lines or have narrow components in addition to the broad line.

For nearby AGNs, high resolution narrow band imaging has been able to resolve the extended narrow line region (NLR) for major narrow emission lines such as the [O III]. The results have indicated that the NLR size is generally ≥ 100 pc (Pogge 1989).

The physical condition of the NLR gas can be diagnosed from the forbidden line ratios. The [S II]λ6716/λ6731 line ratio analysis suggests that the NLR has a typical density of order 10^3 cm^{-3}. Assuming the above density, we can estimate that the temperature is ~ 10000 K based on the ratio of [O III]λ4959 $+ \lambda$5007$/\lambda$4363 (Koski 1978). However, just as the BLR, the NLR has different zones for different emission lines. The density of the entire NLR ranges from 10^3 cm^{-3} to 10^6 cm^{-3}. The temperature is still of the order 10^4 K given the fact that the NLR is photoionized.

Studies have shown that the narrow line width is correlated with nuclear stellar velocity dispersion of QSO's host galaxy (e.g. Nelson and Whittle 1996); the NLR gas is gravitationally bound by the bulge of the host galaxy not the black hole.

1.1.4   Absorption Lines

1.1.4.1   Broad Absorption Lines

In addition to emission lines, about 20% of optically selected QSOs display broad absorption lines in their UV-optical spectra (Weymann et al. 1991; Foltz et al. 1990; Hewett and Foltz 2003). Known as the Broad Absorption Line (BAL) QSOs, those objects have extremely wide ($\sim 10^4$ km s^{-1}) and deep, sometimes black, absorption troughs in the UV bands. The absorption lines are blueshifted up to 30,000 km s^{-1}(e.g. Weymann et al. 1991). All BAL QSOs have the high ionization BALs (hiBALs) such as Lyα, N V and C IV. About 15% of all BAL QSOs also have low ionization BALs (loBALs) such as Mg II and Al III $\lambda\lambda$1855,1863 (Voit, Weymann and Korista 1993). LoBAL QSOs has both high and low ionization absorption lines. HiBAL QSOs have high ionization absorption lines only.

The "balnicity index" defined in Weymann et al. (1991) is a quantitative measure to distinguish BAL QSOs from NAL QSOs. A QSO must have a non-zero balnicity index to be classified as a BAL QSO in Weymann et al. (1991) paper. A non-zero balnicity index requires that, in the spectral region 3000 km s^{-1} blueward of the emission line peak, the broad absorption feature must span at least 2000 km s^{-1}. The balnicity index measures the absorption equivalent width beyond the initial 2000 km s^{-1} but only count the absorption trough that dips below 90% of the estimated continuum level. It is a conservative measure that eliminates the possible NAL contribution for sure.

The balnicity index is intended for the C IV BAL. It is too conservative for absorptions like Mg II in the loBAL QSOs since the Mg II broad absorption lines tends to be weaker, narrower and less detached from the emission

line. So, the SDSS BAL QSO catalog uses an alternative definition for Mg II balnicity index. The absorption line width requirement for Mg II is relaxed to 1000 km s^{-1} from 2000 km s^{-1} for C IV and the low-velocity exclusion limit is reduced to zero from 3000 km s^{-1}(Reichard et al. 2003b). In the FIRST survey BAL QSO catalog, no strict balnicity definition was used. Becker et al (2000) stated that they simply picked out QSOs with significant absorptions blueward of C IV or Mg II emission lines.

BAL QSOs have heavily absorbed soft X-ray radiation and the X-ray absorber column density in BAL QSOs is $\geq 10^{23}$ cm^{-2} (Gallagher, Brandt, Chartas and Garmire 2002). Based on the presence of the P V $\lambda 1118,1128$ doublet in BALs, Hamann, Sabra, Junkkarinen, Cohen and Shields (2002) concludes that the BAL column density for the C IV line could reach 10^{22} to 10^{23} cm^{-2}, which is as large as the X-ray absorbers.

Detection of line locking and locked double trough in the C IV lines in many BAL QSOs indicates that the BAL outflow maybe driven by radiation from the central source (e.g. Foltz, Weymann, Morris and Turnshek 1987; Korista, Voit, Morris and Weymann 1993). From X-ray weak QSOs, which include a high percentage of BAL QSOs, Laor and Brandt (2002) found that the maximum outflow velocity (v_{max}) of absorption lines is correlated with luminosity, which is consistent with the radiatively driven BAL outflow. The heavy absorption of N V BALs over the Lyα emission line indicates that the BAL region must reside outside of the BLR and covers almost the entire BLR as seen from the observer's line-of-sight (Turnshek 1987). Murray, Chiang, Grossman and Voit (1995) proposed a model that could account for both BALs and broad emission lines in a single radiatively driven flow from the accretion disk.

1.1.4.2 Narrow Absorption Lines

Although BALs exist only in high luminosity QSOs, narrow absorption lines (NAL or associated absorbers) with widths of ~ 1000 km s^{-1} have been observed in high and low luminosity AGNs. About 50% of all QSOs have NAL systems. NALs are typically high ionization lines in UV and optical bands. They have blueshifts up to several hundreds of km s^{-1}. The NAL outflow material is also thought to be radiatively driven based on line locking analysis (Peterson 1997).

1.2   Key Correlations

Although QSOs show very diverse observational properties, many of those properties are correlated, indicating a small number of common mechanisms and latent variables that govern the the appearance and classification of QSOs. In this section, we will review the two sets of most important correlations that account for most of object-to-object variations among QSOs.

1.2.1   The Boroson and Green's Eigenvector 1 Relationship

Boroson and Green (1992) used the Principal Component Analysis (PCA) to study Hβ spectral region line measurements of a sample of 87 low z QSOs from the Large Bright QSO Survey (LBQS). The results showed that the correlation matrix of a large number of spectral properties can be reduced to several eigenvectors, each containing a set of correlated variables. The correlations in the most significant eigenvector (Eigenvector 1, hereafter, BGEV1) account for almost 30% of the object-to-object variations in the Hβ region: The decreasing broad Hβ line width corresponds to stronger Fe II op-

tical emission (Fe II(opt)), weaker [O III] $\lambda 5007$ emission, and Hβ asymmetry from stronger red to stronger blue wings.

Subsequent studies by Laor et al. (1994), Laor et al. (1997) and Grupe et al. (1999) extend the BGEV1 to X-ray band. They had shown that the decreasing broad Hβ line width corresponds to steeper soft X-ray spectral index α_x. Wills et al. (1999) further extend the BGEV1 to the UV spectral region. For instance, the decreasing broad Hβ line width corresponds to a larger ratio of Si III] $\lambda 1892$/C III] $\lambda 1909$ indicating higher densities, weaker C IV $\lambda 1549$, stronger N V $\lambda 1240$, and stronger Si IV+O IV] $\lambda 1400$.

If all correlations in the set of variables are linear, each eigenvector represents an independent set of correlations. It is reasonable to assume that all correlations in BGEV1 are connected to a latent variable, which represents a state of the underlying system (see section 1.4.2.2).

1.2.2 BGEV2 and Baldwin Effect

The second eigenvector component in Boroson and Green (1992) (BGEV2) contributes about 20% of the object-to-object variation in the Hβ region. BGEV2 is dominated by the bolometric luminosity. Some line features, such as the [O III] equivalent width, contribute to both BGEV1 and BGEV2. Extending BGEV2 to UV wavelength using spectral principal component analysis on a complete sample of low redshift QSOs, Shang et al. (2003) suggested that well-known QSO luminosity effect, Baldwin Effect, is in fact a key component in BGEV2. Based on QSO UV and soft X-ray properties, Wills et al. (1999) have also concluded the the Baldwin Effect is an luminosity relationship independent of BGEV1.

The Baldwin Effect generally refers to the inverse relation between the

equivalent widths of QSOs' broad emission lines and the continuum luminosity. This inverse relation was first discovered by Baldwin (1977) between the C IV $\lambda1549$ line equivalent width and the continuum luminosity at 1549 Å. Subsequent studies have shown that similar relationships exist for a variety of other strong UV emission lines including Lyα, C III], Al III and Mg II for a variety of different samples (Baldwin, Wampler and Gaskell 1989; Kinney, Rivolo and Koratkar 1990; Green, Forster and Kuraszkiewicz 2001). Baldwin, Wampler and Gaskell (1989) studied the Baldwin Effect for radio quiet and flat spectrum radio loud QSOs separately and did not find significant difference between those two groups. The Baldwin relation has a powerlaw shape with each line having a different powerlaw index β.

$$EW_{line} \propto L^{\beta}$$

Kinney, Rivolo and Koratkar (1990) studied the Baldwin effect for QSOs and Seyfert galaxies spanning a luminosity range of about seven orders of magnitude and found the powerlaw index of $\beta = -0.16 \pm 0.06$ for C IV. Croom et al. (2002) studied a sample of 22000 2dF (Two degree field survey) and 6dF (Six degree field survey) QSOs to look for Baldwin Effects. They binned objects into small redshift bins ($\Delta z = 0.25$) to separate the dependence on luminosity and redshift. The results confirm that Baldwin Effect is a genuine luminosity effect and is not dependent on redshifts.

Most UV broad emission lines show strong Baldwin effects with β ranging from -0.05 to -0.3 (Espey and Andreadis 1999). The Baldwin slope of a given emission line appears to increase with the ionization potential of the emitting ion (the "slope of the slopes"). In the optical region, Hβ and Hγ have low ionization potentials and hence display very shallow powerlaw slope

if there is a correlation at all. However, the N v line has been suggested to display a "reverse" Baldwin effect, which is a positive correlation between its equivalent width and luminosity. The different β values for different lines indicate that Baldwin Effect is probably not a result of the selection effect for including QSOs with highly variable continua in the sample.

In order to explain the dependence between ionization potential and Baldwin Effect slopes, Mushotzky and Ferland (1984) suggested a weak anti-correlation between luminosity and ionization parameter. Netzer, Laor and Gondhalekar (1992) and Wandel (1999a) suggested that QSOs might have luminosity dependent SEDs. Since the physical condition of the dominant BLR emission cloud is selected by the ionizing continuum shape (Baldwin, Ferland, Korista and Verner 1995), there is a natural dependence between the SED (and luminosity) and the line equivalent width. If the ionizing flux decreases with luminosity, we could explain both the Baldwin effect and the "slope of the slopes" (Korista, Baldwin and Ferland 1998).

Other alternative interpretations, such as covering factor or even orientation, have also been suggested (Ferland and Baldwin 1999). Korista (1999) used detailed photoionization models to show that "reverse Baldwin Effect" for the N v line is probably caused by the metal abundance of the gas.

1.3   Deriving QSO Intrinsic Properties

From observational results, we can derive intrinsic properties of the central engine such as the black hole mass and Eddington ratio. Those intrinsic properties are key to understanding the physics inside the central engine and constrains the models. In this section, we will first review methods to calculate

bolometric luminosity and BLR size. Then, we will discuss how to use those two quantities to derive black hole mass and Eddington ratio.

1.3.1 Calculating the Bolometric Luminosity

Based on the QSO SED given by Laor and Draine (1993), we can approximately calculate the bolometric luminosity of any QSO using a universal formula.

$$L_{\text{bol}} = 3 \cdot L_{0.1-1\mu m}$$

Using the same SED, we can replace the integral with the luminosity at a specific wavelength (Laor 1998)

$$L_{\text{bol}} = 8.3 \cdot \lambda L_\lambda(3000\text{Å})$$

where the L_λ(3000 Å) is the luminosity per unit wavelength at the rest wavelength of 3000Å.

In order to calculate L_λ(3000 Å), we have to first obtain the flux at rest wavelength close to 3000Å extrapolate it to F_λ(3000 Å) and then transform it into luminosity using distance calculated from redshift assuming a cosmological model. The detailed calculation steps for our sample is described in section 3.3.

1.3.2 Calibrating the BLR Size

Reverberation mapping of broad emission lines is the most reliable way to figure out the BLR size. Unfortunately, reverberation mapping consumes a lot of telescope time and can only be done to a small number of relatively bright

AGNs. Most of the objects we want to study do not have direct reverberation mapping results.

If the BLR is photoionized, there should be a simple relationship between luminosity and the BLR size.

$$r_{\text{BLR}} \propto L^{1/2}.$$

Reverberation mapping results could be used to calibrate the above relationship. That would allow us to calculate BLR size directly from the luminosity. Kaspi et al. (2000) utilized 7.5 years of reverberation mapping data on 28 PG QSOs to calibrate the Hβ BLR size r_{BLR} versus L relationship. As it turns out, the powerlaw index is different from the 0.5 predicted by simple photo-ionization models.

$$r_{\text{BLR}} = 32.9 \times \left(\frac{\lambda L_\lambda(5100\text{Å})}{10^{44}\text{erg/s}} \right)^{0.700\pm0.033} \text{light days}$$

where $L_\lambda(5100)$ is the luminosity per wavelength at rest wavelength of 5100Å. Vestergaard (2002) re-analyzed the Kaspi et al. (2000) data using an improved technique and gave the following relationship.

$$r_{\text{BLR}} = 30.2 \times \left(\frac{\lambda L_\lambda(5100\text{Å})}{10^{44}\text{erg/s}} \right)^{0.66} \text{light day}.$$

1.3.3 Estimating the Black Hole Mass

We can estimate the black hole mass M_{BH} by applying Newtonian kinematics of the broad emission line region (BLR). Peterson and Wandel (1999) studied several different emission lines and found Keplerian motion of the line

emitting clouds, conforming to the relationship $v \propto r^{-1/2}$, where v is the line width and r is the BLR size determined by reverberation mapping. If we assume that the BLR emission clouds are bound by gravity, the motion can be described by the virial formula,

$$M_{\text{BH}} = \frac{v_{\text{RMS}}^2 \cdot r_{\text{BLR}}}{G},$$

where the BLR size r_{BLR} is the orbital radius of a typical cloud and v_{RMS} is the virial velocity at r_{BLR}. The v_{RMS} is the RMS of the width variation of the monitored emission line in the reverberation mapping process. Vestergaard (2002) indicated that we can use single epoch line FWHM to substitute for the RMS velocity with no apparent side effect. Converting the virial formula to more friendly units, we have

$$M_{\text{BH}} = 1.464 \times 10^5 \times \left(\frac{r_{\text{BLR}}}{\text{light day}} \right) \times \left(\frac{v_{\text{FWHM}}(H\beta)}{1000 \text{km/s}} \right)^2 M_{\odot}.$$

Substituting r_{BLR} with the calibrated r_{BLR} versus L formula, we can calculate black hole mass directly from the object's luminosity and Hβ line width. Vestergaard (2002) also attempted to calibrate the black hole mass calculation method for C IV lines with less accuracy.

For samples of low redshift QSOs, Laor (1998) and McLure and Dunlop (2001) used Hβ line width to calculate AGN black hole mass and then used high resolution host galaxy images to calculate bulge luminosity and velocity dispersion. They found the M_{BH} versus M_{Bulge} and M_{BH} versus σ relationships agree well with existing relationships from normal galaxies, where M_{BH} can be measured reliably using stellar motion. This agreement independently validates our black hole mass calculation method.

1.3.4 Eddington Ratio

The Eddington luminosity limit is the maximum luminosity a spherical accretion powered light source can sustain without creating too much radiative force to drive away its own accretion material. The Eddington ratio, defined as the ratio between the actual luminosity and the Eddington limit luminosity, indicates how close the system is to accreting to its maximum capability. The Eddington ratio is calculated as follows

$$\frac{L}{L_{\text{Edd}}} = \frac{L_{46}}{12.9 \times M_9},$$

where L_{46} is the bolometric luminosity in unit of $10^{46} erg/s$ and M_9 is the black hole mass in unit of $10^9 M_\odot$.

1.4 QSO Central Engine Models

So far, we have reviewed QSO observation characteristics and how to derive physical parameters of the central engine from those observable. In this section, we will review theoretical frameworks used to explain those observational phenomena and the challenges we address in this research.

1.4.1 Unification via Orientation

Based on their spectral properties, QSOs can be categorized into different types. However, the observed differences in QSO spectra do not always reflect the physical differences in the underlying central engine. If we look at the same QSO system from different line-of-sight directions, we could perceive it very differently based on the direct observation data. The AGN unification scheme states that, to first order, all AGN systems have the same structure

and the same internal physical processes. Our observation results depend our viewing angle.

1.4.1.1   The Relativistic Jet

As we had discussed in section 1.1.2, direct observational evidence support the existence of a relativistic jet component in many QSO systems. By its definition, the jet is not spherically symmetric and can have different appearance when viewed from different angles.

The jet emits highly beamed synchrotron radiation within 5—10 degrees of solid angle along its direction. If the jet directly points at us, the radio morphology appears core dominated. Section 1.1.2 details core dominant objects' observational characteristics that can be explained by a beamed jet. The spectrum is flat because it is the sum of many complex emission components, each with a different cut-off frequency, along the line-of-sight. In another words, we are looking into the complex jet internal structure to a large optical depth when the jet is face-on toward us. In fact, the integrated (including both the lobe and core) radio spectral index has been used as an indicator for the jet orientation angle.

The BL Lac objects, high polarization QSOs and rapidly optically variable QSOs are thought to be QSOs with large jet contributions in the UV-optical bands. Those objects are highly variable, have small emission line equivalent widths and high degrees of optical polarization. The beamed synchrotron continuum from the jet adds to the overall continuum level and reduces the emission line equivalent widths. Since the synchrotron radiation is highly polarized in UV-optical, it boosts the overall degree of polarization of the continuum to above 3%. The relativistic beaming not only enhances flux

but also abbreviates time. Hence the variability time scale for continuum that contains a significant beamed component is short.

If we view the QSO outside of the beaming angle, the object appears to have steep radio spectrum. In this case, we will see the jet side-ways and the AGN has a lobe dominated radio morphology, which is produced when the jet impacts the intergalactic medium. Between the FR I and FR II objects, the one-sided jets in FR II objects suggest that they are more beamed and closer to our line-of-sight. The higher radio luminosity of FR II objects is consistent with the beaming effect of the jet.

Since the jet is powered by the central engine, the axis defined by the jet is thought to be the spin axis of the accretion flow (i.e., the accretion disk) that feeds into the central black hole. The accretion disk plane provides another special orientation.

1.4.1.2 The Dusty Torus

The 3 μm bump in QSO SED indicates significant amount relatively cool ($\sim$ 1000K) material in these systems. Since the $\sim$ 1000K temperature coincides with the peak temperature for dust evaporation, it is suggested that the IR emitting gas in QSO system is dusty. Thermal equilibrium calculations indicate that the dusty gas is located at around 1pc from the central continuum source. That is a location between the BLR and NLR. By assuming a special geometric shape of the dusty gas distribution, researchers have constructed an orientation model to explain the emission line differences in two types of QSOs.

Historically, studies of low luminosity Seyfert galaxies have identified two types of AGNs based on their spectral characteristics. The objects that

have both broad and narrow emission lines are Seyfert 1 galaxies (type 1 AGN) and the objects that have only narrow emission lines are Seyfert 2 galaxies (type 2 AGN).

The unification scheme hypothesizes that there is the dusty gas between BLR and NLR is torus shaped. Seen from the black hole, the torus has a large covering factor than the BLR and hence it could block our view to the BLR along certain viewing angles. The torus has a size smaller than or similar to the size of the NLR and hence does not block the NLR from any viewing angle. If the torus blocks our line-of-sight from the inner BLR, we will only see the narrow emission lines (type 2). Since from the view point of the central source, the torus covers only part of the sky, there are directions we can see both the narrow and broad line regions (type 1). This view is supported by results from spectropolarimetry and reddening studies.

- Spectropolarimetry studies discovered broad emission lines in the polarized light from type 2 AGNs. Since polarized flux is often a result of electron or dust scattering, it is believed that the polarized broad emission lines are scattered light from the hidden BLR. The dust clouds above the torus plane scatter the BLR light and redirect some of it to our line-of-sight.

- If our line-of-sight goes through the edge of the torus, the BLR might not be complete obscured. We might still see heavily reddened broad emission lines via the relatively low density dusty clouds near the torus surface. Those systems are known as Seyfert 1.5 to 1.9 AGNs. Goodrich (1990) showed that the Balmer line reddening is likely to be caused by dust obscuring.

Most QSOs are type 1 objects with views directly to the central continuum source and the BLR. That is probably a selection effect since QSOs are selected in UV-optical surveys which tend to pick out objects with exposed central continuum source. Type 2 QSOs are among luminous infrared galaxies that are missed in UV-optical surveys (Low, Cutri, Huchra and Kleinmann 1988; Wills and Hines 1997).

1.4.1.3 Disk Wind Outflow

The torus and jet do not explain the absorption line features. It has long been argued that the BAL might also be an orientation dependent feature because the BAL outflow only covers part of the sky as seen from the QSO center.

- Weymann et al. (1991) suggested that BAL QSOs have statistically the same emission line properties as the non-BAL QSOs. It is improbable to find an underlying physical parameter that would affect absorption lines alone but has no effect on the emission lines.

- If the BLR is completely surrounded by BAL materials that scatter line photons, we would expect the emission line equivalent width and absorption line equivalent width to be equal to reflect the conservation of photons. Based on analysis of emission line and absorption line ratios, Hamann, Korista and Morris (1993) suggested that the BAL outflow covering factor is well below 100% in BAL QSOs. They also concluded that the covering factor of BAL and non-BAL differs by less than 0.2. However, the Hamann, Korista and Morris (1993) study did not consider the effects of dust absorption.

26

- Although the BAL trough in some objects could saturate and have a flat bottom, the flux level inside the trough does not always reach zero, suggesting that there are multiple light paths from the central source to our line-of-sight (Korista, Voit, Morris and Weymann 1993). Spectropolarimetry studies done by Hines and Wills (1995) and Ogle, Cohen, Miller, Tran et al. (1999) have found that the polarized continuum of BAL QSOs rises to the blue. That indicates the contribution of scattered light. The alternative light path for scattered light require a BAL covering factor below 100% of the central object.

If every QSO has a BAL outflow, the 20% occurrence rate of BAL QSOs in the optically selected QSO population indicates that the BAL outflow has a covering factor of 0.2. Based on the disk wind model developed by Murray, Chiang, Grossman and Voit (1995), Elvis (2000) proposed a geometrical unification model that takes into account the BLR, BAL and NAL regions. It attempts to explain both emission line and absorption properties in a single orientation model. In his model, both the emission and absorption materials are embedded in the disk wind. The wind starts off going up vertically from the disk and then bends toward the disk plane due to the radiative pressure from the central source. In each quadrant the final direction of the outflow poses a 30 degrees angle from the disk plane and the opening angle of the outflow itself is 6 degrees. If our viewing angle is within 30 degrees from the disk plane, our line-of-sight would cut through the horizontal branch of the outflow and perceive a projected narrow line velocity of 1000 km s^{-1}. If the viewing angle is between 30 degrees and 36 degrees, we look down the outflow and see the maximum velocity of the BAL outflow.

In addition, the wind itself is not in a uniform physical condition. The part of the flow that is close to the continuum source faces the full continuum and is the source of high ionization emission and absorption lines. The X-ray absorber also resides inside the high ionization zone. The part of the flow that is away from the continuum source receives filtered continuum that passes through the ionized zone. It produces low ionization emission and absorption lines.

1.4.2   Unification via Black Hole Properties

The orientation based unification scheme can explain many but not all observed QSO phenomena. We know that all QSOs do not have exact the same central engines. A complete unification model must describe how the differences in intrinsic parameters, such as luminosity, black hole mass and accretion rate also reflect on QSO observable properties. For any given QSO, its appearance is determined by both the orientation and black hole intrinsic properties. In this section, we will review differences in QSO properties that are not thought to be directly related to orientation.

1.4.2.1   Black Hole Mass and the Onset of the Jet

The radio emission in radio loud QSOs is produced by synchrotron radiation inside the jet and in the lobe. Radio quiet QSOs do not have strong jets compared with those for radio loud QSOs. The difference between radio loud and radio quiet QSOs is clearly not an orientation effect. Since the jet power is an intrinsic physical property of the QSO central engine, it is probably related to the more fundamental black hole and accretion parameters.

- Laor (2000) found that the jet could be turned on in high black hole mass systems and turned off in low black hole mass systems. He suggests that the black hole mass has a threshold value for jet creation, and the jet is either turned on or off.

- As more objects with intermediate radio loudness ($R^* \sim 10$) are found in the FIRST Bright Quasar Survey (FBQS) Reichard et al. (2003b), the radio loud and radio quiet dichotomy view of QSOs has been challenged. Lacy et al. (2001) found that radio luminosity increases continuously with the black hole mass in a sample of FBQS QSOs.

- However, a recent study by Woo and Urry (2002) shows no dependence of radio loudness on the black hole mass.

The relationship between black hole mass and radio loudness is a key research question to address in this thesis.

1.4.2.2 Accretion Rate and the Emission Lines

Orientation is not likely to be the driving factor behind important emission line relationships, such as BGEV1, BGEV2 and the Baldwin Effect, since key components in those relationships are orientation independent.

The [O III] NLR is probably isotropic, causing orientation-independent [O III] emission line in BGEV1.. Boroson (2002) suggested that BGEV1 could be linked to the Eddington accretion ratio L/L_{Edd}. Two key arguments support this hypothesis:

- A narrower Hβ FWHM corresponds to a smaller virial velocity of the BLR gas and hence smaller M_{BH}. For a given luminosity, the smaller

M_{BH} indicates a larger L/L_{Edd}.

- Done, Pounds, Nandra and Fabian (1995) have shown that the steep X-ray slope resembles the outburst state of accretion disks in galactic black holes, which corresponds to higher L/L_{Edd}.

BGEV2 and Baldwin Effect are luminosity relationships. Except for QSOs with strong relativistic beaming, luminosity is not strongly orientation dependent. Boroson (2002) suggested that the underlying physical parameter for BGEV2 is the accretion rate, which is equivalent to luminosity given a fixed accretion efficiency. As we had discussed, the cause for Baldwin Effect could be luminosity dependent ionizing spectrum shapes.

1.4.2.3 Eddington Ratio and the BAL Outflow

As we had mentioned before, the BAL outflow covering factor is smaller than 100%. That means BAL QSOs do have special orientations when the BAL outflow happens to block our line-of-sight. However, orientation alone does not explain all spectral properties of BAL QSOs. There is evidence that BAL QSOs are intrinsically different from the general QSO population.

- Stocke, Morris, Weymann and Foltz (1992) suggested that BAL QSOs are exclusively drawn from radio quiet QSOs. Becker et al (2000) discovered that BAL QSOs can be radio loud or radio quiet. However, the radio detected BAL QSOs tend to have lower radio loudness compared with other radio loud QSOs. It has been suggested that BAL QSOs could fill in the gap between the traditional radio loud and radio quiet QSOs since they are overabundant in the radio-moderate QSO population (Francis, Hooper and Impey 1993).

- Although Weymann et al. (1991) suggested that the emission line properties of BAL QSOs do not differ drastically from the rest of the QSOs, Boroson and Green (1992) suggested that radio quiet QSOs with weak [O III] and strong Fe II are more likely to exhibit BALs. Turnshek, Monier, Sirola and Espey (1997) has found a higher likelihood of finding BAL QSOs in a [O III] weak QSO sample than in a general QSO sample. Boroson and Meyers (1992) found that the Hα broad emission lines in loBAL QSOs tend to have large blue asymmetries. Since the [O III], Fe II line strengths and Balmer line asymmetries are key components in the BGEV1, which is thought to be linked with Eddington ratio L/L_{Edd} rather than orientation, the BAL QSOs might have higher Eddington ratios than the average non-BAL QSO.

- Using 224 BAL QSOs from the SDSS, Reichard et al. (2003a) found that both hiBAL and loBAL QSOs have reddened continua compared with normal QSOs. Consistent with results from Weymann et al. (1991); Sprayberry and Foltz (1992); Low, Cutri, Huchra and Kleinmann (1988); Becker et al (2000), loBAL QSOs are significantly more reddened than hiBAL QSOs and non-BAL QSOs. It has been suggested that the differences in reddening and absorption features between non-BAL, hiBAL and loBAL QSOs may indicate differences in physical properties, such as the slope of the unreddened continuum, between those objects (Reichard et al. 2003a).

In addition, understanding the true nature of BAL QSOs could also help us understand the big picture of QSO evolution. On radio morphology maps, BAL QSOs are compact although their radio spectral index can be

either flat or steep (Becker et al 2000). That suggests that BAL QSOs might be intrinsically small and not yet fully developed. It has been suggested that BAL QSOs might be enshrouded young QSOs in the process of becoming a radio loud QSO by developing the jet and blowing away surrounding materials (Fabian 1999; Haehnelt, Natarajan and Rees 1998).

1.5 My Research

BAL QSOs are important objects for both the orientation-based and intrinsic black hole property-based QSO unification schemes. Since the covering factor of the BAL outflow is not 100%, not all QSOs with BAL outflows would display BALs. BAL QSOs' emission line properties suggest that their orientation parent population (i.e., all QSOs with BAL outflows) are physically different from the rest of the QSO population. However, with only limited BAL QSO observation data today, we do not have concrete proof that BAL QSOs do have distinct orientation-independent emission line properties, such as BGEV1 properties in the optical $H\beta$ spectral region, when compared with the rest of the QSOs. Those distinguished emission line properties, if any, would help us to determine the characteristics of BAL QSO's parent population. In order to link the emission line properties with black hole properties, we need to obtain QSOs' $H\beta$ widths and luminosities.

However, BAL QSOs' $H\beta$ spectral regions have been rarely observed in the past due to their high redshifts (see more details on the selection effect in chapter 2). I have done near infrared spectroscopy observations for the $H\beta$ spectral region on 16 new BAL QSOs. For the first time, we are able to do conclusive statistical studies on BAL QSO's emission line properties in the feature-rich $H\beta$ region and calculate black hole mass and Eddington ratios for

32

those BAL QSOs.

In order to place BAL QSOs in the black hole-based unification scheme, we need to compare them with other non-BAL QSOs. Boroson and Green (1992) investigated a complete low redshift ($z < 0.5$ and $M_B < -23$) QSO sample that is the basis for the BGEV1 and BGEV2 relationships. I added a complete sample of infrared-selected QSOs from Boroson and Meyers (1992) to the sample because it contains Hβ region spectra for low redshift BAL QSOs to compare with our new high redshift BAL QSOs. In both cases, I obtained the digital spectra from the authors and re-measured the Hβ region emission line properties using the same non-linear spectral fitting method I used for my BAL QSO sample to avoid systematic errors.

Compared with Boroson and Green (1992) and Boroson and Meyers (1992) samples, my BAL QSO sample has different redshift and different luminosity ranges. In order to minimize the potential luminosity dependences of emission lines, I also compared BAL QSOs with McIntosh et al. (1999a)'s high redshift QSOs, which have Hβ region spectra observed in the near infrared bands. The Brotherton (1996) and Brotherton (2004) samples are also included to fill the luminosity gap between the high redshift BAL and non-BAL QSOs, and the low redshift Boroson and Green (1992) and Boroson and Meyers (1992) objects, so that I can study how emission lines change with luminosity in more detail.

As a result, I have selected the largest QSO sample to date, spanning 5 orders of magnitudes in luminosity, that have direct Hβ region spectral data. My sample includes BAL QSOs, non-BAL radio quiet QSOs, steep spectrum radio loud QSOs and flat spectrum radio loud QSOs. That allows us to complete the unification picture by studying the Hβ region emission line

33

properties and derived black hole properties for different classes QSOs over a large range of luminosity.

My most important results include that the BGEV1 relationship is closely related to QSO Eddington ratio and extends well into high luminosity objects with BAL QSOs at the weak [O III] strong Fe II end (high Eddington ratio) and radio loud QSOs at the other end; individual BGEV1 properties such as [O III] and Fe II strengths are probably indirectly linked to Eddington ratio via the availability of accretion fuel; BAL QSOs' parent population consists of all QSOs with high luminosity and abundant fuel. Although Eddington ratio is a major differentiating intrinsic property, compared with their luminosity and black hole mass distribution, QSOs have a remarkably small range of Eddington ratios from 0.1 to 1.

The thesis is organized as follows. Chapter 2 describes the sample and data collection methods. Chapter 3 covers the measurement processes including spectral fitting, bolometric luminosity determination and black hole mass and Eddington ratio calculation. Chapter 4 and 5 reports the results and discusses the results in a bigger picture.

Chapter 2

Sample and Observation

2.1 Samples

2.1.1 General Requirements

As I had discussed in the Introduction, BAL QSOs are special objects with a narrow range of orientation angles or extreme black hole accretion parameters. The geometry and physical states of the BAL outflow are key constraints for popular QSOs models (e.g. Murray, Chiang, Grossman and Voit 1995; Elvis 2000). One of the research goals is to understand the physical conditions and processes inside BAL QSOs. By including both BAL QSOs and non-BAL QSOs in a statistical study, I get a wide dynamic range of spectral parameters, which would help understanding the underlying physics that produces different spectral features.

In addition to BAL QSOs, I also try to select a variety of normal UV-optically selected QSOs over a large range of luminosity. Those QSOs include radio quiet, steep spectrum radio loud and flat spectrum radio loud objects. Their diversity allows us to investigate how different classes of QSOs can fit into a consistent physical model. The wide range of luminosity is crucial since that gives us a wide range of black hole masses and possibly different accretion models. The selection requirement for the non-BAL QSO comparison objects is that they all must have good quality Hβ region spectra for reliable black hole, Eddington ratio and BGEV1 parameter measurements.

2.1.2 Selecting BAL QSOs

To archieve the research goals, I would include as many BAL QSOs as possible in the sample. Then I can calculate their black hole masses and Eddington ratios from the bolometric luminosity and Hβ line width. The Hβ line is best calibrated for calculating black hole mass from the reverberation mapping results (Kaspi et al. 2000, e.g.). Although Vestergaard (2002) further calibrated the C IV line width against the Hβ width, I can not use C IV width for BAL QSOs due to the large BAL absorption. An alternative to Hβ is Hα since the Hα width very closely resembles the Hβ width (Stirpe 1991, e.g.). The advantage of Hα line is that it is much stronger than Hβ and is not heavily contaminated by the optical Fe II complex (Boroson and Green 1992).

In addition to providing the Hβ width, the Hβ region spectra also help us to determine BGEV1 properties, such as the optical Fe II and [O III] strengths, for BAL QSOs to compare with normal QSOs. An advantage of the Hβ region over the Hα region is in providing the Fe II and [O III] information.

BAL QSOs with direct Hβ or Hα spectral data are rare. Most BAL QSOs are discovered by UV-optical surveys from their large C IV absorption troughs. In order to detect the C IV line in optical bands, the BAL QSOs are selected to have redshifts ~ 2. The Mg II and Al III loBAL QSOs have less significant redshift selection bias since those absorption lines are closer to the optical bands. However, loBAL QSOs are much rarer too. Due to the large redshift, the Hβ or Hα spectral region of most BAL QSOs is only available in infrared bands, which is not accessible to most telescopes.

In this study, I assemble a sample of BAL QSOs and try to obtain infrared spectroscopy observations of their Hβ and possibly Hα regions. BAL QSOs in this study are selected from the Large Bright QSO Survey, the

Table 2.1. Redshift selection windows for Hβ and Hα lines

Redshift	J	H	K
0.64 – 0.98	Hα		
1.28 – 1.43		Hα	
1.43 – 1.59	Hβ	Hα	
1.59 – 1.67		Hα	
2.05 – 2.09			Hα
2.09 – 2.49		Hβ	Hα
2.49 – 2.66			Hα

FIRST/NVSS Bright QSO Survey (Becker et al 2000), the Sloan Digital Sky Survey (Reichard et al. 2003b) and the Weymann et al. (1991) paper. I select QSOs that have the right redshifts to place the Hβ or Hα region inside the J, H or K atmosphere window (Table 2.1).

I gave priority to objects with detected H magnitude from the 2MASS survey. Those QSOs are brighter and hence tend to have better signal-to-noise results on limited telescopes. That biases this sample against low luminosity QSOs. As a backup plan, I also included several non-BAL QSOs with redshifts similar to the BAL QSOs in this sample. They will contribute to the BAL QSO versus non-BAL QSO comparison study.

2.1.3 The Comparison Sample

For the comparison sample, this study needs Hβ region spectra for all types of QSOs of redshifts from 0 to $\sim$ 2. From the literature, I tried to select representive QSO samples in low ($z < 0.5$), medium ($z \sim 1$) and high ($z \sim 2$) redshifts. A key literature selection criteria is that sample must have raw spectra available or the published line property measurements were based on proper deblending of Hβ, [O III] and optical Fe II emission lines in the Hβ region.

- The McIntosh et al. (1999a) sample is the first high redshift ($z \sim 2$) QSO sample with Hβ region spectroscopy. The objects were observed with near infrared instruments on the MMT. This sample is selected by optical brightness ($V < 18$ mag). This is a flux limited sample for high redshift QSOs. Those objects serve as comparison objects for the BAL QSOs since they are in the sample luminosity range and hence minimizes the intrinsic differences caused by luminosity.

- The Boroson and Green (1992) sample consists 87 optically selected PG QSOs with redshifts below 0.5. This is a flux limited complete QSO sample and is the basis for the discovery of the Principle Components in QSO emission properties. This sample provides a normal, low redshift UV selected QSO population to compare against.

- The Brotherton (1996) sample consists of 60 radio loud QSOs from the Veron-Cetty Veron catalog. They are selected to have $V < 18$ mag and $z < 0.95$. It is not a complete sample. Among them, 41 were observed using optical instrument on the McDonald Observatory 2.7m telescope and 19 were from the literature.

- The Brotherton (2004) sample consists of 32 optically bright ($V <$ 17.5 mag) radio loud and radio quiet QSOs with intermediate redshifts ($1 < z < 2$). The Hβ region of those objects were observed using the optical instrument on the McDonald Observatory 2.7 telescope, near infrared instruments at Kitt Peak National Observatory (KPNO) 2.1m telescope and infrared spectrometer at the Cerro Tololo Interamerican Observatory (CTIO) 4m telescope. This sample fills the gap between the low and high luminosity QSOs in the sample.

- The Boroson and Meyers (1992) sample consists of 19 infrared luminous QSOs with warm infrared colors from the IRAS survey. Those objects are known as warm extragalatic objects (WEO) (Low, Cutri, Huchra and Kleinmann 1988). All the objects in this sample have low redshifts ($z < 0.5$). This sample contains an unusually large proportion of low redshift BAL QSOs, especially loBAL QSOs.

- The Shields et al. (2003) paper re-measured the Hβ region of two of Dietrich et al (2002)'s high redshift ($z > 3$) radio quiet QSOs. Those are among the highest redshift QSOs that have the Hβ region spectra.

The entire sample and the basic characteristics of each object can be found in tables in appendix A.

2.2   Telescopes and Instruments

I used the United Kingdom InfraRed Telescope (UKIRT) 3.8m and NASA's InfraRed Telescope Facility (IRTF) 3m telescopes to obtain infrared spectral data in the Hβ or Hα emission line region for the high luminosity,

39

high redshift QSOs. Both are dedicated ground-base infrared telescopes and both have thermal characteristics suitable for J, H, and K band observations. Hence, I choose the high redshift and BAL QSOs with redshifts such that their Hα or Hβ lines are shifted into those windows.

I had two observation runs with UKIRT and one observation run with IRTF during 2001.

- I observed the Hβ spectra for 16 BAL QSOs and 2 non-BAL RQ QSOs using the CGS4 spectrometer on UKIRT. Some of the QSOs are observed multiple times across different days at the same or different bands. I typically co-adds exposures from different days to improve the signal-to-noise ratio of the final spectrum, unless one exposure is particularly bad and only increases noise in the co-added spectrum. All those QSOs have redshift at around 2. The observation log for the UKIRT runs is available in Table 2.2. All the RA and DEC values are epoch 2000.

- I observed 5 BAL QSOs, all of which are from the FBQS catalog Becker et al (2000), using the Spex spectrograph on IRTF. Those observations have yield useful data on Hα measurements. Those objects have redshifts around 1. The observation log for the IRTF run is available in Table 2.3.

The weather conditions for each day is listed in Table 2.4. In this section, I will discuss the instruments used and their limitations.

Table 2.2.   New Infrared Observations from UKIRT CGS4

R.A 2000	Dec. 2000	Date UT	Exposure Time (s)	z	H mag	Type	Observation Band
005135	−010709	2001.08.15	1080	1.56	16.0	RQ	J
072418	+415914	2001.03.13	480	1.56	15.9	loBAL	J
091328	+394444	2001.03.12	600	1.57	15.8	hiBAL	J
093404	+315331	2001.03.14	480	2.42	15.7	hiBAL	H
101342	+085126	2001.03.11	840	2.26	15.1	loBAL	H
101342	+085126	2001.03.14	600	2.26	15.1	loBAL	H
105427	+253600	2001.03.11	540	2.39	16.2	loBAL	H
123356	+130409	2001.03.14	600	2.38	15.7	BAL	H
123458	+130855	2001.03.14	600	2.36	15.9	BAL	H
142013	+253404	2001.03.11	600	2.20	15.7	hiBAL	H
144515	−002359	2001.03.14	1200	2.22	16.6	hiBAL	H
144515	−002359	2001.03.12	600	2.22	16.6	hiBAL	H
144545	+012912	2001.03.12	720	2.44	16.2	hiBAL	H
151636	+002941	2001.03.15	960	2.25	15.7	loBAL	H
170919	+281835	2001.08.17	600	2.38	15.7	BAL	H
170919	+281835	2001.08.16	360	2.38	15.7	BAL	H
171124	+593121	2001.08.15	1800	1.49	18.7[a]	loBAL	J
172341	+555340	2001.08.17	1440	2.11	15.3	loBAL	H
173523	+554611	2001.08.15	900	1.59	15.7	hiBAL	J
213623	+154508	2001.08.16	480	2.13	14.9	RQ	H
221511	−004549	2001.08.17	600	1.48	14.9	loBAL	H
221511	−004549	2001.08.15	900	1.48	14.9	loBAL	J
232224	−000719	2001.08.15	720	1.54	15.7	RQ	J

Note — Some objects are objects over multiple nights. The co-added spectra are used whenever possible.

[a]No 2Mass data available. Used the z' magnitude from the SDSS survey.

Table 2.3.   New Infrared Observations from IRTF Spex

R.A	Dec.	Date	Exposure Time	Redshift	H mag	Type
080901	+275342	2001.04.28	720	1.23[a]	15.6	hiBAL
104459	+365605	2001.04.27	3840	0.70	15.1	loBAL
131213	+231959	2001.04.27	7200	1.52	15.4	hiBAL
132422	+245222	2001.04.28	7200	2.36	15.9	loBAL
140806	+305448	2001.04.28	2400	0.84	15.6	loBAL

[a]The redshift from Becker et al (2000) is incorrect.

Table 2.4.   Observation Condition Notes

Date	Seeing	Notes
2001.03.10	$\sim 1.5''$	Partly cloudy
2001.03.11	$\sim 1''$	Windy and partly cloudy at latter half of the night
2001.03.12	$\sim 0.5''$	Cirrus at sunset, clear at sunrise
2001.03.13	$\sim 0.7''$	Patchy cloudy
2001.03.14	$\sim 0.7''$	Cirrus
2001.03.15	$\sim 1''$	Clear
2001.04.27	$\sim 1''$	Clear
2001.04.28	$\sim 0.6''$	Cirrus
2001.08.15	$\sim 0.5''$	Clear
2001.08.16	$\sim 1''$	Very cloudy
2001.08.17	$\sim 2''$	Cloudy

2.2.1 UKIRT and CGS4

UKIRT has a primary mirror of 3.8m. It is the biggest telescope dedicated to near-infrared observations. From its low-latitude location, UKIRT covers both northern and southern skies. However, due to its mount position, only objects with declinations from -40° to $+60^o$ are accessible. An additional requirement for UKIRT target selection is that the target has to be at least 18m bright in V band. Although the main scientific instrument records infrared photons, UKIRT uses optical images to locate the object and point the telescope.

I used the CGS4 near infrared spectrograph, with a 256x256 InSb NICMOS array detector. The 40 l mm^{-1} low-resolution grating was used because it provides the best compromise between wavelength coverage, spectral resolution and limiting magnitudes. It covers the entire J or H or a large part of K band in a single observation. The 2-pixel wavelength resolution (R$\sim$ 300) provided by the 40 l mm^{-1} is sufficient to allow measurement of the width of Hβ broad lines, which are typically more than 1000 km/s. Most importantly, the low-resolution configuration allows us to detect H=16 objects in a reasonable integration time. Using the 300 mm long focus camera, each detector pixel corresponds to a slit width of 0.6″. The slit can be opened to project widths of 1, 2, or 4 pixels wide, corresponding to 0.6, 1.2 and 2.4″ on the sky. The slit can also be rotated toward any position angle in the sky.

During the exposure, UKIRT uses a star in the optical acquisition camera field to guide the telescope. The star is also used by the tip-tilt control of the secondary mirror to improve seeing. That guide star needs to be at least 18 magnitudes in V band and within 5′ from the target. In addition, various parts of the guide field are obscured by components of the optical instruments

(e.g., the dichroic). I cannot use any guide star that happens to fall into the obscured part. Finding a suitable guide star for the QSO targets is a challenging task since most of them are at high galactic latitude. I used the UKIRT observation preparation software ORAC-OT to plot star survey catalog images on a simulated guide field and choose the guide star prior to the actual observation. With tip-tilt guiding, UKIRT can achieve typical seeing of $0.5''$ on an average night.

2.2.2   IRTF and SpeX

The IRTF telescope is a 3 m telescope. The telescope can reach declinations from -51° to $+66^o$. The HA range is ± 5 hours. Within 60 degrees from zenith, the telescope has a pointing accuracy of $2''$. The SpeX observation is conducted by Michael Brotherton. He used the SpeX instrument to take the target spectrum. In the observation mode used, SpeX covers from 0.8 micron to 2.5 micron using a prism cross disperser. The spectral resolution is 2000 in J band. Since IRTF/SpeX is a smaller telescope and has a higher spectral resolution, it does not go as deep as UKIRT/CGS4 under the same observation conditions. We used IRTF/SpeX to observe the relatively brighter $z \sim 1$ objects.

The cross-dispersed spectra of different orders are recorded on a 1024x1024 InSb array. A 512x512 slit viewer infrared InSb array is used to target acquisition. The slit viewer has a field of view of $60''$x$60''$. SpeX uses an infrared star image in the slit viewer field to guide the telescope. The guide star must be brighter than 18m in J band. When there is no guide star available in the field and the target is bright ($J < 15m$), the IRTF observer can also guide directly on the slit using the infrared target image.

2.3 Observation Procedures

The UKIRT-CGS4 and IRTF-SpeX observations follow similar procedures.

2.3.1 Target Acquisition and Guiding

Since both telescopes can point to an accuracy of $1''$-$2''$, I can place the target object very close to the slit using the catalog coordinates. On UKIRT-CGS4, I perform a "peak up" with the main spectrograph to position the infrared image inside the slit once the telescope is pointed to the specified position. The "peak up" procedure is to take 7 short exposures (10 to 30 seconds each) along a line perpendicular to the slit on both sides of the slit and figure out the position that results in the maximum photon counts. The photon counts from the peak up procedure helps us to determine the exposure time of the object. Some objects are so faint in infrared that they require longer than 30 seconds for each peak-up step exposure. My experience is that if an object is not visible in a 30-second exposure, I will not be able to get good enough spectral signal-to-noise to calculate Hβ width in a 2-hour integration. On IRTF-SpeX, we can see the target in the infrared field and place it into the slit using the slit viewer camera. After the target is acquired, we select a bright star in the guider field and keep the telescope tracking for the spectral exposures.

During the UKIRT-CGS4 observations, I chose the slit width from $0.6''$ to $1.2''$ (1 or 2 pixels wide) depending on the seeing measured from a K-band monitoring camera. The $1.2''$ slit is used in most cases to gather as much light from the target as possible. On IRTF-SpeX, a $0.8''$ wide slit was used throughout the observing run.

Since the slit in both instruments can be rotated, I could have used a different slit position angle for each target to trace the atmospheric refraction angle, which minimizes the leak of spectral flux caused by the position offsets between the acquisition image, the red wavelength image and the blue wavelength image. However, since I acquired the target through infrared images and the wavelength coverage is small, the atmospheric refraction is not a big problem in my observations. In addition, slit rotation is an expensive operation. I would have to re-acquire the target and redo the CCD calibration tests after each rotation. Hence, I only rotate 90 degrees to avoid light from a nearby star, which would otherwise fall into the slit and confuse with the QSO light at offset positions.

2.3.2 Exposure

Both the CGS4 and SpeX operated in 4-exposure nodding cycles. The first exposure in the cycle is taken at the telescope position where the target is originally acquired in the slit; Second, telescope is moved to an offset position along the slit and two more exposures are taken; Then, the telescope is moved back to its original position and the last exposure is taken to complete the 4-exposure cycle. All exposures have the same exposure time. The exposure time is limited by two factors. First, the exposure time must be short enough so that the sky does not undergo drastic changes during the 4-exposure cycle. If the sky has non-linear changes, the subtraction step in the subsequent reduction process would not be able to take out the background. Second, the exposure time must be chosen so that the atmosphere emission lines do not saturate the detector array. Otherwise, the saturated regions would completely cancel out during the subtraction and eliminate target spectral information. As a result,

I choose 120 seconds exposure time for almost all target QSO observations in both UKIRT-CGS4 and IRTF-SpeX. Standard star exposure time is shorter to reduce the risk of saturating.

If the sky background does not change or only change linearly over time during the 4-exposure cycle, I can subtract the offset position images from the original position images and completely cancel out strong infrared background radiation. So, the co-added target spectral image for each object has two sets of parallel spectra. The spectra taken at the original nod positions have positive values while the spectra taken at the offset nod positions have negative values. The two sets of parallel spectra are separated by the nodding distance on the detector image.

2.3.3 Standard Stars

The light from the QSO passes through the atmosphere and then gets recorded by the detector before I can get the digital spectrum. The atmosphere and the detector respond to photons differently at different wavelength. Hence, they alter the shape of the spectrum. The raw observed spectrum recorded is the true spectrum from the QSO multiplied by the atmospheric absorption curve and the detector response curve.

To calculate the effects of the atmosphere and detector sensitivity curve, I choose standard stars that have known intrinsic spectral shapes as comparison objects. I record the standard star spectra under the same atmospheric condition and using the same detector setting as the target QSO observations. By comparing the resultant spectra with the known shape, I can calculate the sensitivity functions and then apply them to correct the target QSO spectra. In near infrared observations, there are two types of standard stars used in the

two-step continuum shape calibration process.

- To correct atmospheric absorption, I need a standard star that has intrinsically smooth spectrum with weak and few stellar absorption lines. The atmospheric absorption curve is hence the multiplier function that is needed to bring to the observed spectrum to a smooth overall shape. F or G type stars have weak intrinsic absorption lines and are good candidates for atmospheric comparison stars. In order to minimize the changes in atmosphere conditions, I try to observe the comparison stars within 0.1 airmass from the target's mean airmass during the integration.

- To remove the detector sensitivity function, I need to have a standard star whose intrinsic continuum spectral energy distribution is accurately known. Since the known spectral shape is expressed in wavelength against flux density, I also convert the observed photon counts to flux density in this correction step. The O and B type stars are great candidates for such standard stars since they have spectral shapes very close the black body. The intrinsic absorption lines in O and B stars do not matter much here since I only need to know that continuum bands follow the black body function and can simply interpolate across any absorption feature. If the O and B standard stars have spectrophotometry data, I can use them to calibrate the target QSO's flux to absolute levels.

However, in the observations, I have decided to use F and G stars to remove both the atmospheric absorption and detector sensitivity curve for the following reasons.

- Since the observation condition was not photometric and I did not use very large slit width, it is impractical to absolutely flux calibrate the spectra. In addition, I have gathered infrared photometric data for almost all QSOs in the sample from 2MASS, making absolute flux calibration less important.

- The O and B type stars are shorted lived and hence are rare in stellar populations. Since most the target objects have high galactic latitudes, it is difficult to find O or B stars nearby. Studies (Strecker, Erickson and Witteborn 1979) have shown that the F or G star's continuum deviates from the perfect black body shape by about 2-3% in the spectral coverage range. That is well within the uncertainties of the flux calibration.

So, my procedure is to first observe a F or G star close to the target QSO and manually remove the visible stellar absorption lines. I divide the black body shape, determined by the temperature corresponding to the spectral type, by the observed spectrum to get the overall correction function which is the product of the atmospheric absorption function and the detector response curve. At last, I multiply the overall correction function to the target QSO spectrum to get the flux calibrated (in the relative scale) spectra.

2.3.4   Wavelength Calibration Lamps

The CGS4 has three internal calibration lamps. I select the Argon lamp for the J band observations and the Xenon lamp for the H band observations. The selection of calibration lamps is primarily based on the number of sharp lines in the given spectral region and whether those lines are evenly distributed. The IRTF-SpeX instrument uses an Argon lamp for all wavelength calibration

purposes. The calibration spectrum is typically taken after a long integration period. I move the telescope back to its median RA in the previous integration to minimize the effects of telescope and spectrograph flexure flexing before taking the calibration lamp spectrum.

I use the calibration spectrum to determine the actual spectral resolution of the instrument. With a slit width of 1.2″ CGS4 yielded a resolution of 3 pixels as measured from Argon and Xenon comparison lamp spectra ($\sim$ 600 km s^{-1} in J band and $\sim$ 750 km s^{-1} in H band, see Figures 2.1 and 2.2). The actual spectral resolution of the target object should be better than the above value since, in good seeing and stable tracking conditions, the actual target image is not likely to fill the entire 1.2″ slit as the comparison lamp light does.
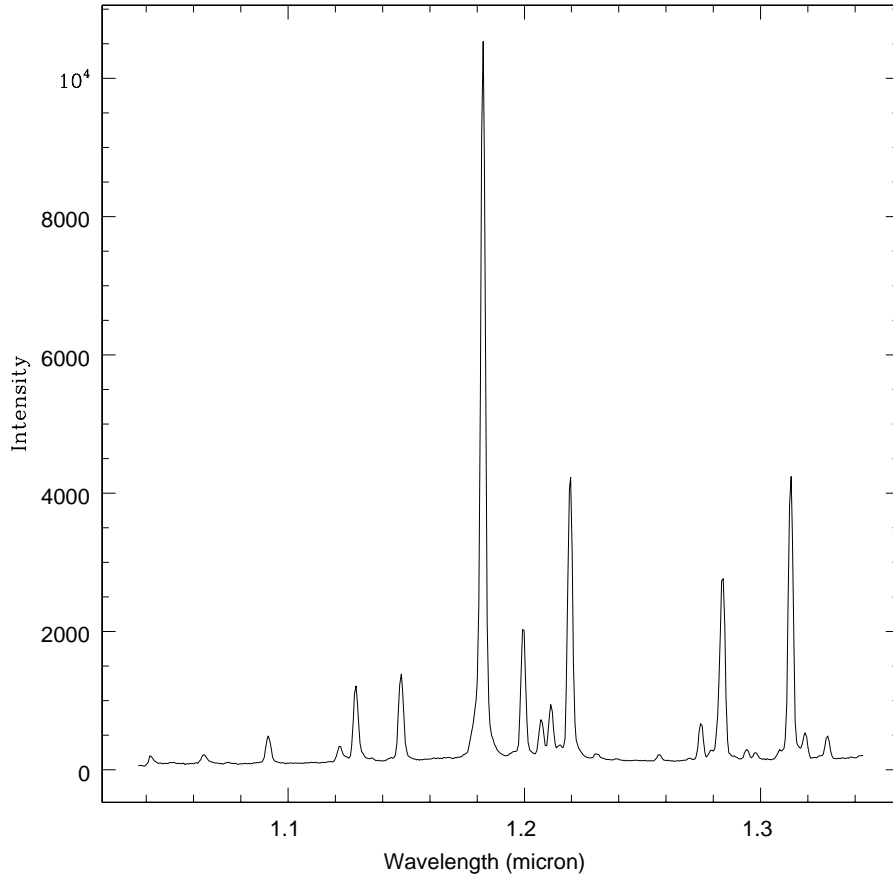
Figure 2.1 The spectral resolution in UKIRT/CGS4's J band is ~ 600 km s^{-1}.
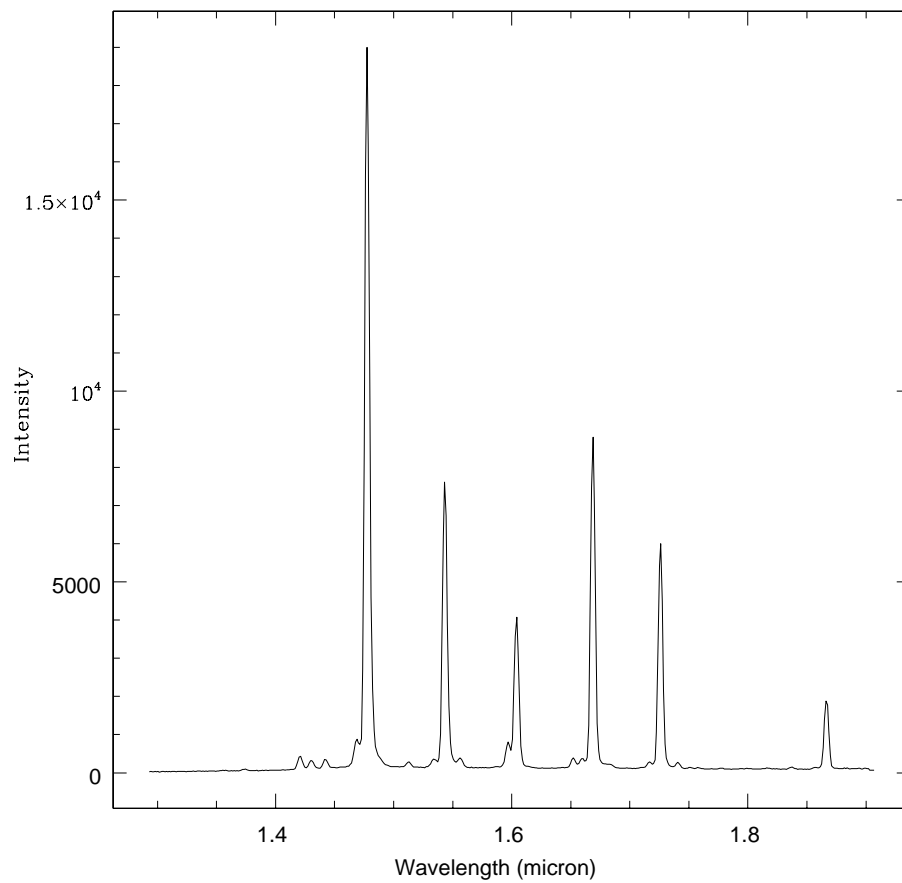
Figure 2.2 The spectral resolution in UKIRT/CGS4's H band is ~ 750 km s^{-1}.

Chapter 3

Data Analysis and Measurements

3.1 Infrared Spectral Reduction

The UKIRT/CGS4 raw spectral images were automatically processed to correct for CCD bias, dark field and flat field at the observation site using the ORAC pipeline software. The IRTF/SpeX images have to be processed after the observation using the Spextool software package. The CGS4 data reduction pipeline and the Spextool also combine frames taken from the offset positions and subtract them from the combined frame taken at the original position. The final frame for each target shows both the positive and negative dispersed image of the object in the slit.

3.1.1 Extracting Target Spectra

The UKIRT/CGS4 spectra are extracted using the IRAF spectral data reduction tasks. Since IRAF's aperture finding algorithm can only locate positive peaks, I make a negative copy of each frame. The IRAF spectra extraction task finds the original and offset apertures respectively on the two frames. The central positions of the aperture along the dispersion axis are traced using a 3-5 order Spline function. Once the aperture peak is found, I define an aperture width that extends to at least 95% of the peak flux level to both sides of the peak. Within the aperture width, IRAF's optimal extraction method is used to extract a one-dimensional spectrum. The background level is

54

fitted using a straight line across sample points on both sides of the spectrum. The background sample points are 10 to 12 pixels from the center trace.

The IRTF/SpeX spectra were extracted using the Spextool software version 2.1. The apertures of different orders were located and traced using its internal template that is specific to the IRTF/SpeX instrument. The background is also fitted and subtracted for both positive and negative aperture images.

If the target is very faint, both the IRAF and Spextool algorithms might have difficulty in finding and tracing the apertures. If that is the case, I use the fitted aperture trace function from a close-by atmospheric star as a template to extract the spectral data from the target frame.

3.1.2 Wavelength Calibration

The target frame extraction parameters are used as templates to extract spectra from the calibration lamp frames and noise frames with the exact same positions and the exact same aperture widths. Using IRAF, I have to first identify the calibration lamp emission lines from at least one spectrum. A 3 to 5 order smooth curve is fitted to map pixel coordinates to wavelength coordinates. I only do the line identification and manual fitting for one comparison lamp spectrum per night. All the rest are assumed to have only a shift from the first one, which can be easily determined by cross-correlation. I apply the calculated wavelength to pixel number mapping function to the target spectra and re-calculate their flux density in a linear observed wavelength space. The wavelength calibrated spectra from the original and offset apertures are then added in the wavelength space to give us the total spectrum of the target object. The noise spectra are processed the same way.

Using Spextool, it is much simpler since most of the algorithms have been tuned to match the data characteristics of the instrument. I just need to review the line identification and fitted dispersion curve. The software then automatically applies the wavelength correction to the target spectra.

3.1.3 Flux Calibration

For the reasons I had discussed in section 2.3.3, I do not attempt absolute flux calibration. Assuming that both the QSO spectrum and the F or G standard star spectrum are affected by the same atmospheric absorption and detector response functions, I divide the observed QSO spectrum by the standard star spectrum to remove the effect of the absorption and response functions. Then, I multiply the result with the assumed black body spectrum of the standard star to get the flux density spectrum of the target QSO. Possible source of uncertainties in this step are as follows.

- The removal of stellar absorption lines from the standard star, especially in the atmosphere absorbed parts of the spectrum, might be incomplete. Since the absorption lines in F and G stars are very weak and their peak intensity is less than 5% of the continuum level in most cases, this only produces <5% spikes in the noisy regions of the final spectrum.

- The F and G standard star's intrinsic continuum shape might deviate from the black body function. As I had mentioned in section 2.3.3, this only introduces about 2−3% of error in the continuum shape in my sample's wavelength coverage.

3.1.4   Reduced Spectra

The UKIRT/CGS4 final reduced spectra have a continuum signal-to-noise ratio of 10 to 20 per resolution element in the Hβ region. The final reduced UKIRT/CGS4 spectra are available in appendix III.

For each IRTF/SpeX object, I have to combine spectra of different orders to form a 1-D continuous spectrum. I verify that the regions with overlapping wavelengths agree with each other within 3σ of the noise. In those overlapping spectral regions, I calculate average values of the flux for the combined spectrum. As expected, the combined spectra show very high noise levels outside the atmospheric windows. For most objects, both Hβ and Hα spectral regions are covered in the combined spectrum. I do not have enough signal-to-noise ratio to deblend lines in the Hβ region. However, the Hα region for most objects has typical signal to ratio of 15 in the emission line and hence yield reliable results on Hα line FWHM. The reduced and combined IRTF/SpeX spectra are available in appendix III.

3.2   Hβ Region Line Decomposition

Measuring line and continuum properties in the Hβ region is complicated by the blending of many broad optical Fe II lines. The deblending is done as follows.

- For the new UKIRT infrared observations, I used the SPECFIT (Kriss 1994) program within IRAF to deblend spectral components.

- To ensure consistency, I applied the same SPECFIT procedure to deblend lines from McIntosh et al. (1999a) and Boroson and Green (1992)

57

spectra because the published line measurements of those two studies were derived from other methods.

- The Brotherton (1996) and Brotherton (2004) spectra were deblended using SPECFIT in the same way as I did. Hence I took published values in the literature for objects in those two papers.

- For most of my IRTF/SpeX objects, the signal-to-noise ratio in the Hβ region is too low for SPECFIT deblending. In that case, I only measure the Hα FWHM and use it as an indicator for Hβ FWHM (Stirpe 1991).

I decomposed each Hβ region spectrum into a powerlaw continuum, broad (BLR) and narrow (NLR) Hβ components, a broad Hγ component, a narrow-line [O III] $\lambda\lambda$4959,5007 doublet and Fe II emission blends. I estimated the slope and level of the power-law continuum by eye using the lowest points in the spectrum, and then put them into the fitting process as fixed parameters. If the initial estimates cannot result in acceptable fits, I would adjust the continuum accordingly within the range of possible values determined by visual inspection and refit the model. This procedure allows us to avoid unrealistic continuum fits resulted from fitting processes that have too many free parameters.

Besides the continuum slope and level, the other fixed parameters are the [O III] $\lambda\lambda$4959,5007 doublet ratio of 2.94, the Hγ versus Hβ ratio of 0.36, and the narrow Hβ to [O III] λ5007 ratio of 0.1 (Veilleux and Osterbrock 1987). Except for some M99a spectra with known broad [O III] lines, the narrow component in Hβ and the [O III] line were represented by single Gaussians with width equal to the instrumental resolution (Boroson and Green 1992). The Fe II emission blends were represented by Boroson and Green (1992)'s

I Zw 1 template. All broad lines including Fe II were assumed to have the same Gaussian profile. Rest wavelength ratios were constrained except for some M99a objects with shifted [O III] lines (McIntosh et al. 1999b). Free parameters were the intensities of [O III], broad Hβ, the Fe II blends, and broad line widths. Using line intensities and the underlying continuum levels, I can calculate equivalent widths for Hβ and [O III] lines. I also measured the Fe II component equivalent width between 4434Å, and 4484Å(as measured in the original template).

In many cases, a single Gaussian profile was inadequate to represent the broad Hβ line. To correct for this, I adopted the following procedure after running SPECFIT. I first subtracted all fitted components except broad Hβ and smoothed the remaining Hβ by fitting multiple Gaussian profiles to it, each at least as wide as the instrumental resolution. Then, I measured the integrated flux and FWHM of the smoothed profile. I tested the measurement method described here on BG92 spectra, finding no systematic difference from their results.

The line measurements for all QSOs in the sample are available in appendix A.

3.2.1 Upper Limits

For objects that do not have detectable [O III] or Fe II emission lines, I determine an upper limit for the line flux empirically. The upper limit of the [O III] line equivalent width is set to be three times the signal-to-noise ratio multiplied by the spectral resolution of the instrument. The upper limit for Fe II equivalent width is harder to determine: For all spectra except for those from Brotherton (1996) and Brotherton (2004), I visually inspect the model
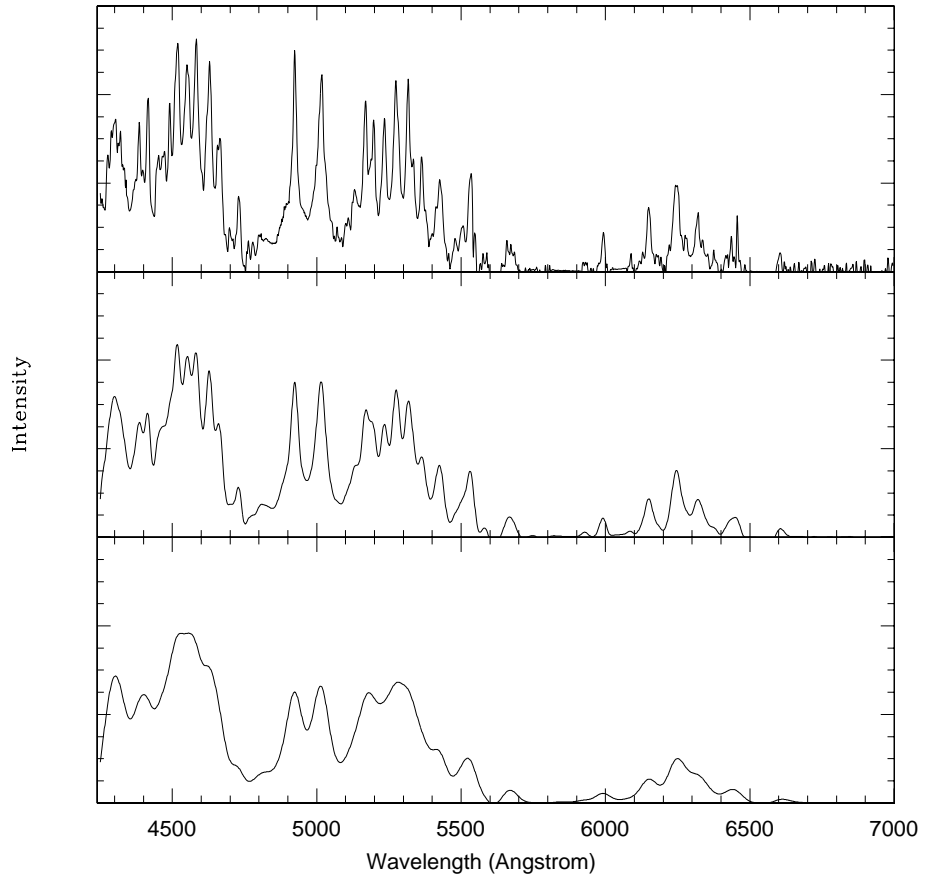
Figure 3.1 From top to bottom are the original I Zw 1 Fe II template, the template broadened to 1500 km s^{-1} and the template broadened to 3000 km s^{-1}.
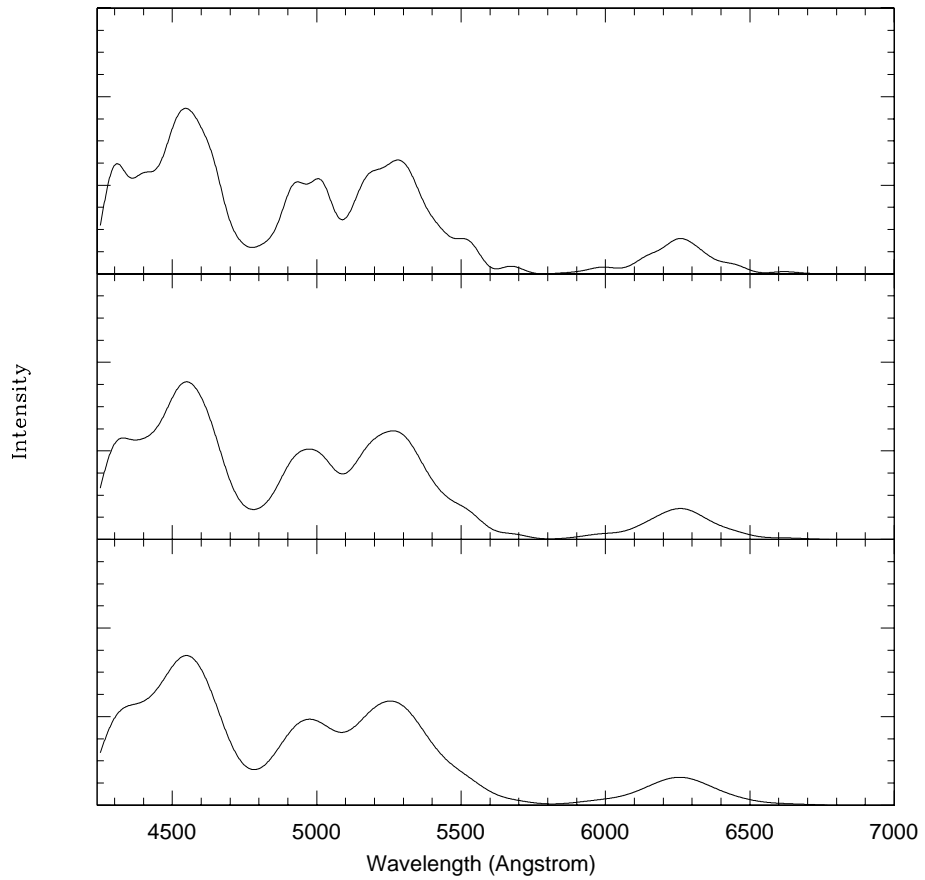
Figure 3.2 From top to bottom are the I Zw 1 Fe II template broadened to 5000 km s^{-1}, 7000 km s^{-1} and 9000 km s^{-1} respectively.

fit and then gradually increase the strength of the Fe II template while keeping all other model parameter values fixed at the results given by SPECFIT. The upper limit of the Fe II strength is determined when the resultant model clearly rises above the noise level of the spectrum. For the Brotherton spectra, I chose the smallest detected Fe II equivalent width in his sample, which is 10Å, as the Fe II equivalent width upper limit for the objects with non-detectable Fe II lines.

3.2.2   Measurement Uncertainties

It is very difficult to estimate line measurement uncertainties in a spectral region dominated by multiple broad and intervening components, such as the Hβ region of QSOs in my study. Most previous works do not give error estimates on all line measurements (e.g. Boroson and Green 1992), or only give rough estimates based on signal-to-noise (e.g. Osterbrock 1979), or give uncertainty estimates based on artificial spectral components in linear fitting procedures (McIntosh et al. 1999a). Here, I investigate to see how to improve the uncertainty estimate.

SPECFIT (Kriss 1994) is a multiple parameter nonlinear fitting program. In this application, I have 8 free parameters. Uncertainties given by SPECFIT are derived from the error matrix. Uncertainty for each parameter is calculated as if that parameter is the only one interesting parameter in the fitting (Kriss 1994). To adjust those one-interesting-parameter uncertainties to realistic multiple interesting parameters case, requires complex analysis of the inter-dependence among parameters (Avni 1976). If I try to determine "upper limits" of uncertainties by pretending that all the 8 interesting parameters are independent of each other, I will have to multiply an unusually

large factor (more than a factor of ten) to each error bars given by SPECFIT (Avni 1976). The resultant uncertainties are unstable and useless as uncertainty "upper limits". In fact, the fitting uncertainties do not come equally from all parameters. For example, the uncertainty on continuum level has a large impact on the uncertainty levels of other parameters.

I decide to estimate the measurement uncertainty through a trial-and-error process and determine the boundary conditions by visual inspection. This method is similar to BG92's method of goodness of the fit judgment. Use SPECFIT to refit two representative spectra with strong Fe II. The two spectra are chosen to have both broad and narrow Hβ emission profiles. Then, I shift the fitted continuum up and down and refit all other components until the overall fit become unacceptable. I calculate how much the line measurements vary in the process. That has given us a 15% and 10% 1-σ uncertainties on a typical emission line strength and FWHM respectively.

3.3 Continuum Luminosities

As I had discussed in the Introduction, in order to calculate the total bolometric luminosity, black hole mass and Eddington ratio, I need to calculate the per wavelength luminosity at 3000Å (L_{3000}) and 5100Å (L_{5100}). I extrapolate flux densities derived from observed magnitudes assuming that all QSOs have the same intrinsic SED with spectral index of -0.5.

$$f_\nu \propto \nu^{-0.5}$$

I minimize the extrapolation uncertainties by choosing photometric points close to rest wavelength 4000Å. Since this sample covers a wide range

63

of redshifts, I collected photometric observation points from several different sources for each object and then select the closest match to use. The photometric data sources include the following.

- The 2MASS point source catalog is used for J, H and K magnitudes for high redshift objects.

- The SDSS second data release is used for optical magnitudes for low redshift objects.

- However, since the SDSS second data release has a limited sky coverage, some low redshift QSOs in my sample do not have photometric data available from SDSS. For many Boroson and Green (1992) objects, I obtained spectrophotometric data points in optical range from the Neugebauer et al. (1987) paper.

- If a low redshift QSO is covered by neither SDSS nor Neugebauer et al. (1987), I adopt the published magnitude from the Veron-Cetty-Veorn catalog.

When calculating the QSO luminosity, I assumed that we are viewing the isotropic thermal radiation source from an unobstructed angle. If the flux in our viewing direction is absorbed by material along the line of sight, we will calculate the luminosity incorrectly. BAL QSOs, especially loBAL QSOs, tend to have reddened continua compared with the average QSO composite continuum. Using the most recent BAL QSO colors derived from the Sloan Digital Sky Survey (Tolea, Krolik and Tsvetanov 2002), I estimate a generous upper limit for extinction at rest wavelength 4000Å corresponding to ~0.8 mag, corresponding to under-estimates of black hole mass and Eddington ratio

by factors of $< 10^{-0.2}$ and $< 10^{-0.1}$ respectively. No correction was applied. I assumed a cosmological model with $H_0 = 70\ km\ s^{-1}\ Mpc^{-1}$, $\Omega_m = 0.3$ and $\Omega_\Lambda = 0.7$ (Freedman 2002).

The bolometric luminosities and subsequent black hole mass and Eddington ratio results for all QSOs in the sample are available in appendix A.

3.4   Radio and Absorption Line Properties

In order to investigate how the black hole mass and Eddington ratio fit into QSO unification schemes, I also collected radio loudness and radio spectral index data for QSOs in my sample. Although some past studies have used the flux density radio between 5GHz to 4400Å in the observed frame to calculate radio loudness R^* (Kellermann et al. 1989), I choose to use rest frame specific flux ratio because of the large redshift range in my sample. Radio loud QSOs have $R^* > 10$.

For each object, I looked up NED for radio flux measurements. If multiple measurements are available, I choose one that has the smallest measurement uncertainty around rest wavelength 5 GHz. For objects that do not have radio flux measurement, I look up the FIRST/NVSS sky map. If the object is covered by those surveys but does not have concrete detection in the map, I adopt the survey limit of 3.4 mJy (White, Becker, Helfand and Gregg 1997) as its flux upper limit. The observed radio flux is extrapolated to 5GHz rest wavelength assuming a spectral index of -0.75 (Benn, Grueff, Vigotti and Wall 1988). For objects with multiple radio flux measurements at different wavelengths, I also measured their radio spectral index at rest frequency 5GHz.

For BAL QSOs, I am interested in how the absorption strength correlates with emission line and black hole properties. Instead of using the Weymann et al. (1991) balnicity index, which does not work well with loBALs (see chapter 1), I measured the broad absorption line equivalent width for each BAL QSO.

The radio and BAL property measurements are available in appendix A.

3.5 Uncertainties in Calculating Black Hole Mass and Eddington Ratio

The standard reverberation method for calculating black hole mass and Eddington ratios from FWHM(Hβ) and bolometric luminosity has been verified and calibrated for typical type 1 AGNs (see the Introduction). However, my QSO sample contains a number of objects with atypical properties. In particular, I will discuss the reverberation method's applicability for BAL QSOs and steep spectrum radio loud QSOs in my sample.

In BAL QSOs, the outward force due to radiation pressure exceeds the gravitational force and drives the massive outflow (e.g. Arav, Li and Begelman 1994). It has been suggested that the BAL outflow could be launched from a radius close to the BLR. If the BLR gas is not shielded from the radiation pressure, it could become part of the outflow, which has terminal velocity up to 0.1c. That would violate the assumption that the BLR gas is gravitationally bound in Keplerian orbits and therefore render the black hole mass and Eddington ratio estimates in BAL QSOs inaccurate. However, the emission line emissivity decreases drastically in a diverging flow as the distance between the gas and the central radiation source increases. The emission line profile is determined by BLR gas that has just escape velocity, which is close to the

Keplerian velocity at the emission radius (e.g. Murray and Chiang 1998). To further support this argument, my BAL QSO's Hβ line profiles do not display large blue wings, which is the signature of BLR gas in a high-speed outflow. Although Boroson and Meyers (1992) have suggested that BAL QSO Hβ lines might have excess emission in the blue wing compared with normal QSOs, the excess wing only accounts for a small percentage of the line flux. The small and low intensity blue wing does not have any effect on the emission line FWHM since it never rises above the half intensity point of the profile. Based on the above analysis, I do not apply any correction to BAL QSOs' black hole mass and Eddington ratio calculated from the FWHM — L method.

According to AGN orientation unification picture, flat spectrum radio loud objects are normal QSOs with their relativistic jets pointing toward us. The jet beams the synchrotron radiation and inflates the QSO continuum level. Padovani and Urry (1992) demonstrated that in rest wavelength optical regions, up to half of the observed flux could come from the beamed synchrotron radiation. In another word, I could have over-estimated the luminosity for flat spectrum QSOs by a factor 2.

The face-on orientation of the jet may also mean that we are viewing the accretion disk face-on as well. It has been suggested that the BLR has a flat shape (Rokaki, Boisson and Collin-Souffrin 1992) and it is close to the accretion disk (Murray and Chiang 1997). If we view a disk shaped BLR face-on, the Hβ line profile would not reflect the virial motion inside the disk. The observed BLR velocity is expressed as follows.

$$\sqrt{v_r^2 + v_p^2 \sin^2 \theta},$$

where v_r is the random velocity of the gas clouds, v_p is the Keplerian velocity inside the disk and θ is the viewing angle from the disk axis. Wills and Browne (1986) reported that a model with $v_r = 4000$ km s^{-1} and $v_p = 13000$ km s^{-1} would be able to explain the observed broad line FWHM versus radio core dominance distribution. The objects with extreme beaming (i.e., superluminal motion objects and optically violent variables) have an mean Hβ FWHM of 3000 km s^{-1} while the steep spectrum and lobe dominant objects with edge on viewing angle have mean Hβ FWHM of 6000 km s^{-1}(Wills and Browne 1986). Hence, I conservatively estimate that the Hβ FWHM for flat spectrum radio loud objects in my sample might be under-estimated by a factor of 2. As we will see in section 4.3.2, this is a very conservative estimate.

Since $M_{\rm BH} \propto v_{\rm FHWM}^2 \cdot L^{0.66}$ and $L/L_{\rm Edd} \propto v_{\rm FHWM}^{-2} \cdot L^{0.34}$, I could have under-estimated the $M_{\rm BH}$ by a factor of 2.5 and over-estimated the $L/L_{\rm Edd}$ by a factor of 5 for flat spectrum radio loud objects.

Chapter 4

Results

The QSO sample in this thesis consists of objects from several different papers and observation runs (see more about the sample selection in chapter 2). Each of those sources has a different selection redshift range and chooses different types of QSOs for its specific research purposes. In this sample, I have BAL QSOs, including hiBAL and loBAL QSOs, radio loud QSOs (including steep spectrum and flat spectrum objects), and radio quiet non-BAL QSOs (I simply refer to them as radio quiet QSOs in this thesis). Refer to the Introduction chapter for the definition of those QSO types.

Although some QSO sub-samples in the overall sample might be complete by themselves (e.g., the Boroson and Green (1992) sample is complete for QSOs with $z < 0.5$ and absolute magnitude $M_B > -23$), the mixed sample I have is certainly not. I have a different mixture of QSO types at different redshifts or luminosity. For example, many radio loud objects are selected at $z \sim 1$ (Brotherton 1996, 2004) and BAL QSOs are primarily selected at $z > 2$ (new observations). In order to study the relationship between any spectral property and a luminosity derivative, such as the black hole mass and Eddington ratio, I carefully eliminate the possible selection effect caused by different types of QSOs selected at different luminosities. For example, if property X is intrinsically independent of luminosity but is dependent on QSO type, with BAL QSOs having unusual levels of X, the apparent correlation between X

and luminosity in the entire sample may simply be because BAL QSOs tend to be selected at high luminosity. For any pair of properties X and Y, artificial correlations could be created by the selection effect, if X is linked to QSO types and Y is linked to luminosity. To minimize selection effects, I study correlations within each QSO type. Figure 4.1 shows the symbols for each QSO type used in plots throughout this thesis.

Tables 4.1, 4.2, 4.5 and 4.6 list the Pearson or generalized Kendall tau correlation coefficients between each pair of properties for the radio quiet, radio loud and BAL QSOs sub-samples and the entire combined sample. I correlated the logarithmic values of the measured or derived QSO property. All data points that are upper limits are adjusted using survival analysis before the generalized Kendall tau method is used derive the correlation coefficient. For each significant correlation, the two-tailed probability of the correlation to arise from unrelated variable (the null probability) is listed in parenthesis below it.

$\times$ Steep spectrum radio loud QSOs

☉   Flat spectrum radio loud QSOs

$\square$ Radio quiet non−BAL QSOs

$\blacktriangle$ Low ionization BAL QSOs

$\blacksquare$ High ionization BAL QSOs

⬟   Unclassified BAL QSOs

Figure 4.1 Symbols representing different types of QSOs. Those symbols are used in plots throughout this paper.

Table 4.1.   Correlation table for the radio quiet objects

	L	FWHM Hβ	EW [O III][a]	Fe II/Hβ [a]	M_{BH}	L/L_{Edd}	EW Hβ
FWHM Hβ	0.509 (0.000)						
EW[a] [O III]	−0.590 (0.000)	−0.176					
Fe II/Hβ[a]	0.125	−0.105	−0.604 (0.000)				
M_{BH}	0.905 (0.000)	0.826 (0.000)	−0.523 (0.000)	0.053			
L/L_{Edd}	0.200 (0.051)	−0.742 (0.000)	−0.301 (0.032)	0.308 (0.027)	−0.235 (0.021)		
EW Hβ	−0.138	0.315 (0.002)	0.708 (0.000)	−0.521 (0.000)	0.068	−0.463 (0.000)	
EW[a] Fe II	0.111	0.068	−0.369 (0.008)	0.898 (0.000)	0.121	−0.005	0.050

[a]The correlation coefficients in those columns or rows are generalized Kendall's tau.

If not otherwise noted, the correlation coefficients in this table for Pearson coefficients.

Table 4.2. Correlation table for the radio loud objects

	L	FWHM Hβ	EW^a [O III]	Fe II/Hβ ^{a}	M_{BH}	L/L_{Edd}	EW Hβ	EW^a Fe II	Radio loudness
FWHM Hβ	0.114								
EW^a [O III]	−0.527 (0.001)	0.077							
Fe II/Hβ^a	0.122	−0.290 (0.036)	−0.590 (0.000)						
M_{BH}	0.832 (0.000)	0.646 (0.000)	−0.369 (0.014)	−0.090					
L/L_{Edd}	0.514 (0.000)	−0.794 (0.000)	−0.372 (0.013)	0.301 (0.030)	−0.049				
EW Hβ	−0.296 (0.006)	0.476 (0.000)	0.531 (0.000)	−0.347 (0.012)	0.039	−0.592 (0.000)			
EW^a Fe II	0.003	−0.064	−0.460 (0.001)	0.802 (0.000)	−0.058	0.028	0.028		
Radio loudness	0.247 (0.022)	−0.112	−0.084	0.052	0.128	0.248 (0.022)	−0.256 (0.018)	−0.034	

Table 4.2—Continued

	L	FWHM Hβ	EW [O III] [a]	Fe II/Hβ [a]	M_{BH}	L/L_{Edd}	EW Hβ	EW Fe II [a]	Radio loudness
Radio S.I.	0.353 (0.001)	−0.307 (0.005)	−0.474 (0.002)	0.222	0.089	0.460 (0.000)	−0.357 (0.001)	−0.090	0.028

[a]The correlation coefficients in those columns or rows are generalized Kendall's tau.

If not otherwise noted, the correlation coefficients in this table for Pearson coefficients.

Table 4.3. Correlation table for the steep spectrum radio loud objects

	L	FWHM Hβ	EW [a] [O III]	Fe II/Hβ [a]	$M_{\rm BH}$	$L/L_{\rm Edd}$	EW Hβ	EW [a] Fe II	Radio loudness
FWHM Hβ	0.210								
EW[a] [O III]	−0.587 (0.006)	−0.016							
Fe II/Hβ[a]	0.026	−0.283	−0.706 (0.000)						
$M_{\rm BH}$	0.842 (0.000)	0.704 (0.000)	−0.485 (0.022)	−0.035					
$L/L_{\rm Edd}$	0.433 (0.005)	−0.791 (0.000)	−0.286	0.249	−0.121				
EW Hβ	−0.185	0.354 (0.025)	0.330	−0.230	0.060	−0.442 (0.004)			
EW[a] Fe II	−0.056	−0.100	−0.541 (0.006)	0.891 (0.000)	−0.070	0.051	0.033		
Radio loudness	0.232 (0.022)	−0.022	−0.135	0.160	0.157	0.166	−0.338 (0.033)	0.042	

Table 4.3—Continued

	L	FWHM Hβ	EW [O III] [a]	Fe II/Hβ [a]	M_{BH}	L/L_{Edd}	EW Hβ	EW Fe II [a]	Radio loudness
Radio S.I.	−0.126	−0.325 (0.041)	−0.317	0.397 (0.042)	−0.271	0.220	0.139	0.369 (0.062)	−0.156

[a]The correlation coefficients in those columns or rows are generalized Kendall's tau.

If not otherwise noted, the correlation coefficients in this table for Pearson coefficients.

Table 4.4.   Correlation table for the flat spectrum radio loud objects

	L	FWHM Hβ	EW [O III][a]	Fe II/Hβ [a]	M_{BH}	L/L_{Edd}	EW Hβ	EW Fe II [a]	Radio loudness
FWHM Hβ	0.085								
EW[a] [O III]	−0.222	−0.019							
Fe II/Hβ[a]	0.129	−0.258	−0.454 (0.033)						
M_{BH}	0.795 (0.000)	0.672 (0.000)	−0.133	−0.117					
L/L_{Edd}	0.478 (0.002)	−0.834 (0.000)	−0.057	0.315	−0.153				
EW Hβ	−0.154	0.545 (0.000)	0.419 (0.072)	−0.438 (0.038)	0.218	−0.565 (0.000)			
EW[a] Fe II	0.096	0.081	−0.476 (0.032)	0.759 (0.000)	0.030	0.006	0.039		
Radio loudness	0.109	−0.273 (0.085)	−0.114	0.015	−0.085	0.301 (0.056)	−0.200	−0.042	

Table 4.4—Continued

	L	FWHM Hβ	EW [O III] [a]	Fe II/Hβ [a]	M_{BH}	L/L_{Edd}	EW Hβ	EW Fe II [a]	Radio loudness
Radio S.I.	0.290 (0.066)	−0.130	−0.324	0.027	0.137	0.275 (0.082)	−0.096	0.054	−0.066

[a] The correlation coefficients in those columns or rows are generalized Kendall's tau.

If not otherwise noted, the correlation coefficients in this table for Pearson coefficients.

Table 4.5.   Correlation table for the BAL QSOs

	L	FWHM $H\beta$	EW [a] [O III]	Fe II/Hβ [a]	M_{BH}	L/L_{Edd}	EW $H\beta$
FWHM $H\beta$	0.638 (0.000)						
EW[a] [O III]	−0.231	−0.019					
Fe II/Hβ[a]	0.137	−0.097	−0.739 (0.001)				
M_{BH}	0.907 (0.000)	0.903 (0.000)	−0.125	0.004			
L/L_{Edd}	−0.147	−0.855 (0.000)	−0.198	0.288	−0.551 (0.001)		
EW $H\beta$	−0.297 (0.099)	0.019	0.572 (0.010)	−0.621 (0.011)	−0.156	−0.222	
EW[a] Fe II	−0.117	−0.155	−0.367 (0.090)	0.826 (0.000)	−0.069	0.149	0.269

[a]The correlation coefficients in those columns or rows are generalized Kendall's tau.

If not otherwise noted, the correlation coefficients in this table for Pearson coefficients.

Table 4.6.   Correlation table for all QSOs

	L	FWHM Hβ	EW [O III] [a]	Fe II/Hβ [a]	M_{BH}	L/L_{Edd}	EW Hβ
FWHM Hβ	0.481 (0.000)						
EW[a] [O III]	−0.484 (0.000)	0.008					
Fe II/Hβ[a]	0.130	−0.249 (0.006)	−0.808 (0.000)				
M_{BH}	0.899 (0.000)	0.817 (0.000)	−0.340 (0.000)	−0.024			
L/L_{Edd}	0.217 (0.001)	−0.751 (0.000)	−0.398 (0.000)	0.409 (0.000)	−0.233 (0.001)		
EW Hβ	−0.304 (0.000)	0.202 (0.003)	0.659 (0.000)	−0.504 (0.000)	−0.099	−0.454 (0.000)	
EW[a] Fe II	−0.042	−0.163 (0.076)	−0.597 (0.000)	0.858 (0.000)	−0.111	0.151	0.033

[a]The correlation coefficients in those columns or rows are generalized Kendall's tau.

If not otherwise noted, the correlation coefficients in this table for Pearson coefficients.

4.1 The Luminosity Relationships

In this section, I discuss how QSO observational and central engine properties correlate with the bolometric luminosity. I will also discuss how luminosity related selection biases might affect my results since different types of QSOs in my sample are primarily chosen from sub-samples taken at different redshifts.

Luminosity itself is highly dependent on redshift due to the well-known selection effects that low luminosity objects are missed out at high redshifts in flux limited samples. It is potentially difficult to separate out emission properties that are correlated with luminosity from those that are correlated with redshift. However, Corbett et al. (2003) have shown that there is little dependence between QSO emission properties and redshift at a given luminosity. So, I do not worry about redshift effects in this analysis.

4.1.1 Luminosity versus Hβ Broad Line Equivalent Width

The anti-correlation between QSO luminosity and broad emission line equivalent width is one of the key relationships governing QSO emission spectral properties (Baldwin Effect, see chapter 1). Past studies have been inconclusive on whether the Baldwin Effect exists for lines in the Hβ region. In this section, I will take advantage of the large luminosity coverage in the sample and investigate Baldwin Effect correlations for Hβ and Fe II broad lines.

Since past studies have not found differences in Baldwin Effect for different types of QSOs (see Chapter 1), I first correlate EW(Hβ) against L for my overall sample in order to take advantage of the large sample size and luminosity coverage. At first glance, I found a strong anti-correlation between EW(Hβ) and L. The probability of such anti-correlation to arise from un-

correlated random variables (i.e., the null probability) is less than 0.1%. The regression formula for EW(Hβ) on L is shown below and the regression line for EW(Hβ) over L is plotted in Figure 4.2. The percentage uncertainty of EW(Hβ) is same as the percentage uncertainty of L. For all QSOs,

$$\log(EW(H\beta)) = (4.75 \pm 0.64) - (0.0636 \pm 0.0138) \times \log(L).$$

The four outliers with small EW(Hβ) are as follows.

- PG 1351+236 (a.k.a. Mrk 0662): This is a radio quiet object from the Boroson and Green (1992) sample. It appears to have genuinely small Hβ broad line with a large narrow peak on the broad profile.

- HB89 0955+326: This is a flat spectrum radio loud object from the Brotherton (1996) sample. Its continuum and Hβ emission line profile are known to vary with large amplitudes (Neugebauer et al. 1989).

- HB89 1156+295 and 1641+399 (a.k.a. 3C 345): Those two are flat spectrum radio loud objects from the Brotherton (1996) sample. They are well-known blazars with large, variable synchrotron emission in the optical bands. Those objects illustrate how the synchrotron beaming could cause systematic scatter in L or emission line equivalent width related diagrams (e.g., Figure 5.1).

However, there are two possible biases that could influence the strong anti-correlation observed in the entire sample.
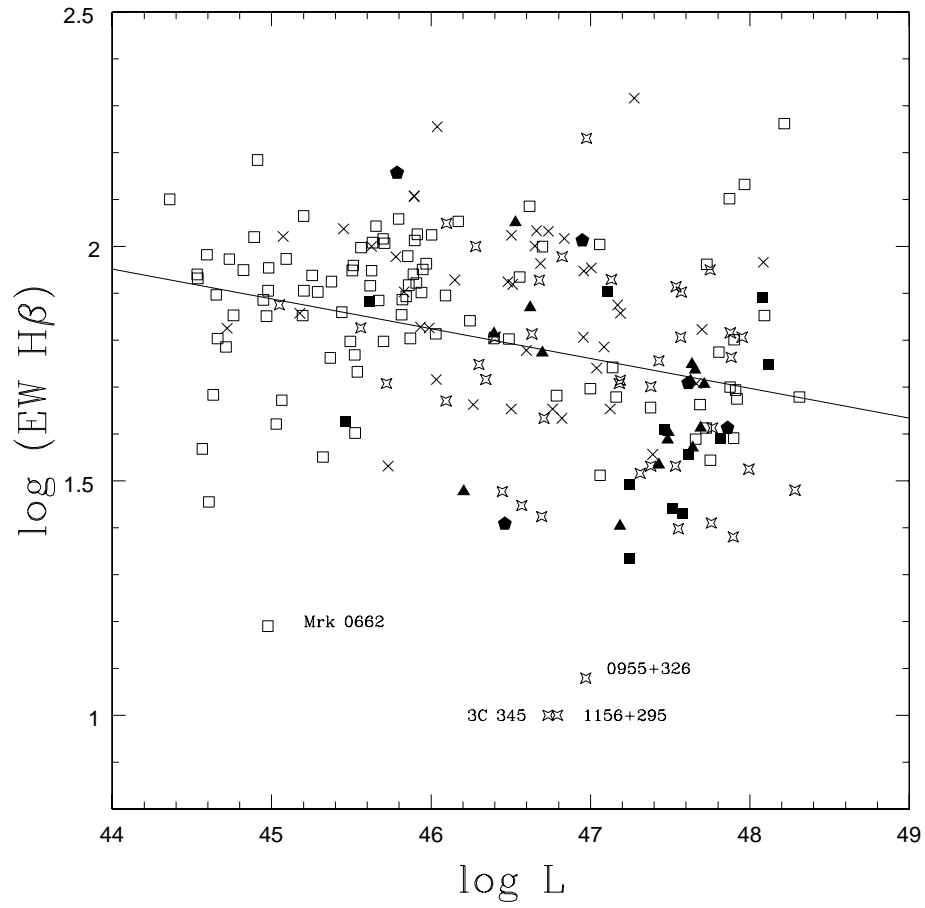
Figure 4.2 The *L* versus EW(Hβ) anti-correlation for all QSOs. The solid line is the regression result. The four outliers with small EW(Hβ) are discussed in the text.

- The inclusion of flat spectrum radio loud objects: A flat spectrum radio loud object could have a strong beamed synchrotron component in its continuum, which results in artificially inflated L values and reduced EW(Hβ) (see Section 3.5).

- The inclusion of BAL QSOs: BAL QSOs in my sample are predominantly selected at high redshift (see Chapter 2) and hence they have high luminosity. From Figure 4.2, BAL QSOs seem to have smaller EW(Hβ) compared with other high luminosity QSOs. The mean value of $\log(EW(H\beta))$ is 1.769 ± 0.044 for non-BAL radio quiet QSOs with $\log(L) > 47$, and 1.615 ± 0.032 for BAL QSOs with $\log(L) > 47$.

To eliminate the above possible biases in the Hβ Baldwin Effect, I re-did the correlation and regression without flat spectrum radio loud objects and BAL QSOs. The anti-correlation is no longer significant with a null probability of 17% and the regression slope consistent with zero at 1.5σ level for EW(Hβ) on L. The intrinsic scatter of the EW(Hβ) distribution might be caused by parameters independent of L (BGEV1, see Section 4.2.4). The regression line is plotted in Figure 4.3. For all QSOs excluding the flat spectrum radio loud objects and BAL QSOs,

$$\log(EW(H\beta)) = (2.82 \pm 0.68) - (0.0206 \pm 0.0148) \times \log(L).$$

To further investigate the Hβ Baldwin Effect, I analyzed the anti-correlation for different sub-samples of QSOs. For the non-BAL radio quiet objects, flat spectrum radio loud QSOs and steep spectrum radio loud QSOs,
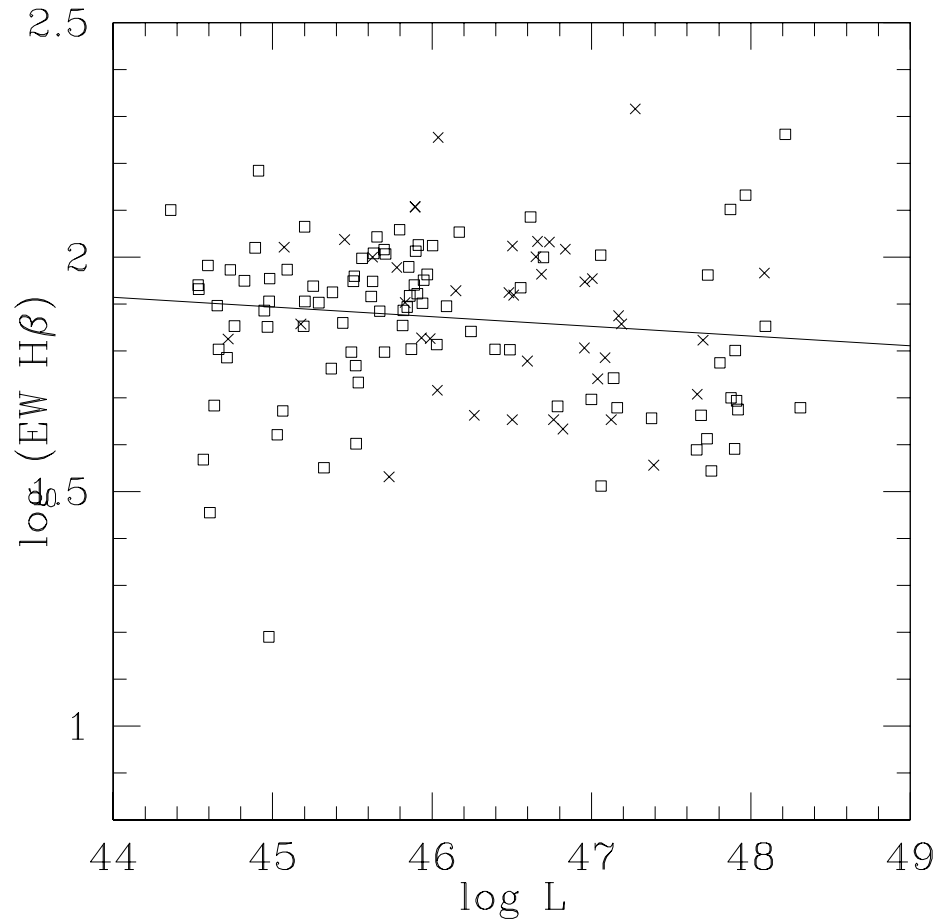
Figure 4.3 The L versus EW(Hβ) anti-correlation for all QSOs excluding flat spectrum radio loud and BAL QSOs. The solid line is the regression result for EW(Hβ) on L. The anti-correlation is insignificant and the regression slope is consistent with zero at 1.5σ.

such anti-correlation is not significant. For BAL QSOs, the anti-correlation is marginal with a null probability of 10%.

For optical Fe II lines, there is no correlation between the equivalent width and luminosity within the radio loud, radio quiet, BAL QSO sub-samples or the overall QSO samples.

4.1.2   Luminosity and [O III] Line Equivalent Width

I discovered a very strong anti-correlation between EW([O III]) and L (the [O III] "Baldwin Effect") with the null probability less than 0.1% for the overall sample. Figure 4.4 shows the anti-correlation with the EW([O III]) on L regression line plotted. The regression formula is

$$\log(EW(O[III])) = (9.36 \pm 1.39) - (0.176 \pm 0.030) \times \log(L).$$

However, the Figure 4.4 also indicates the radio loud QSOs (red symbols) are displaced to have stronger EW([O III]) and BAL QSOs (solid symbols) are displaced to have weaker EW([O III]) compared with the overall regression line. Those displacements are scatters in the luminosity relationships (BGEV2) introduced by the orthogonal BGEV1 relationships since EW([O III]) is an important BGEV1 property (see later in this chapter, section 4.2). Since radio loud and BAL QSOs are selected at different luminosity ranges (see Chapter 2), such scatter could cause systematic bias in the EW([O III]) versus L anti-correlation. So, I decide to further study the [O III] Baldwin Effect for each QSO sub-samples. For radio quiet non-BAL QSOs, the null probability for the anti-correlation is less than 0.1%. The slope of the EW([O III]) on L regression for non-BAL radio quiet QSOs is consistent with the slope for the
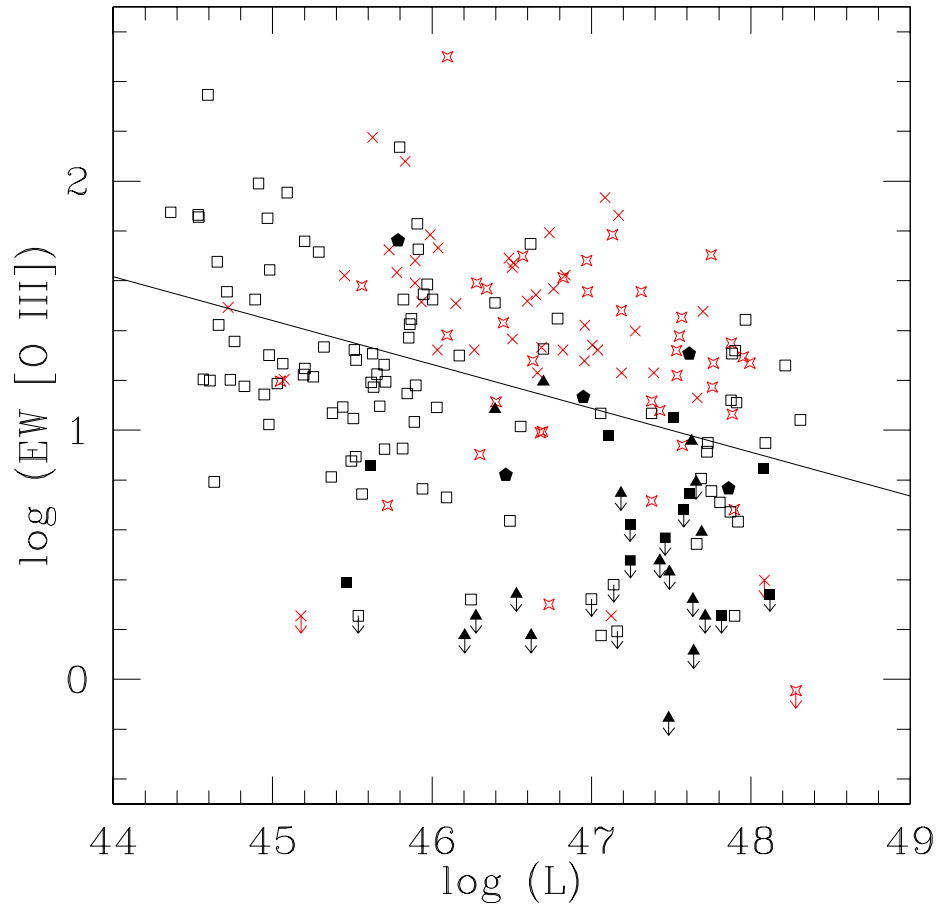
Figure 4.4 There is a strong anti-correlation between [O III] and L for the overall QSOs sample. The solid line is the regression result for EW([O III]) on L. The red symbols are radio loud objects.

overall sample within 1σ uncertainty. The regression formula for EW([O III]) on L and vice versa are as follows.

$$\log(EW(O[III])) = (9.79 \pm 1.70) - (0.187 \pm 0.037) \times \log(L).$$

$$\log(L) = (47.41 \pm 0.29) - (1.168 \pm 0.230) \times \log(EW(O[III])).$$

For BAL QSOs, most of the EW([O III]) measurements are upper limits only and hence I do not run the regression. For radio loud QSOs, the null probability of the anti-correlation is 0.1%. However, the flat spectrum radio loud objects might still bias the results with beamed continuum luminosity. The anti-correlation is not significant among the flat spectrum objects sub-sample but is significant in the steep spectrum objects with a null probability less than 1%. The steep spectrum radio loud QSOs' EW([O III]) on L regression slope is still consistent with those from the overall sample and from the non-BAL radio quiet sample within $1-\sigma$ uncertainty. For steep spectrum radio loud QSOs, the regression formula for EW([O III]) on L and vice versa are as follows.

$$\log(EW(O[III])) = (9.17 \pm 3.75) - (0.166 \pm 0.081) \times \log(L).$$

$$\log(L) = (47.33 \pm 0.41) - (0.567 \pm 0.274) \times \log(EW(O[III])).$$

The [O III] Baldwin Effect has been suggested in the past. Steiner (1981) found that [O III]/Hβ is anti-correlated with X-ray luminosity for low

Figure 4.5 There is a strong anti-correlation between [O III] and L for the non-BAL radio quiet QSOs sample. The solid line is the regression result for EW([O III]) on L and the dashed line is the regression result for L on EW([O III]).
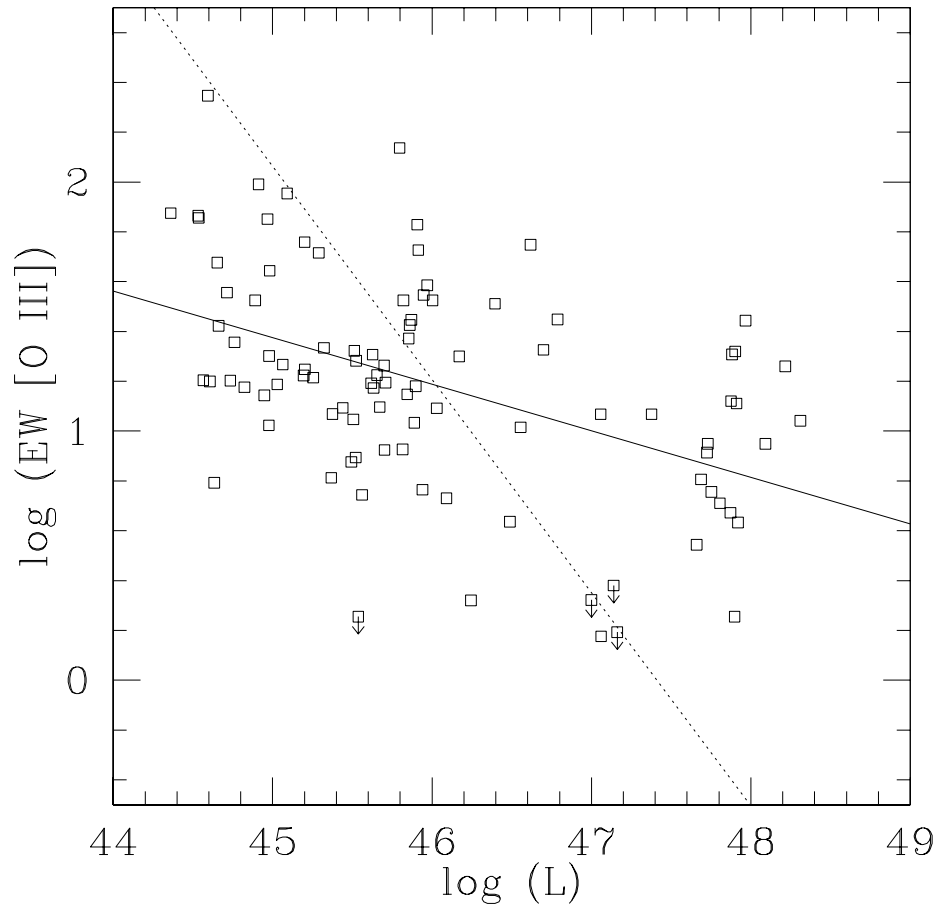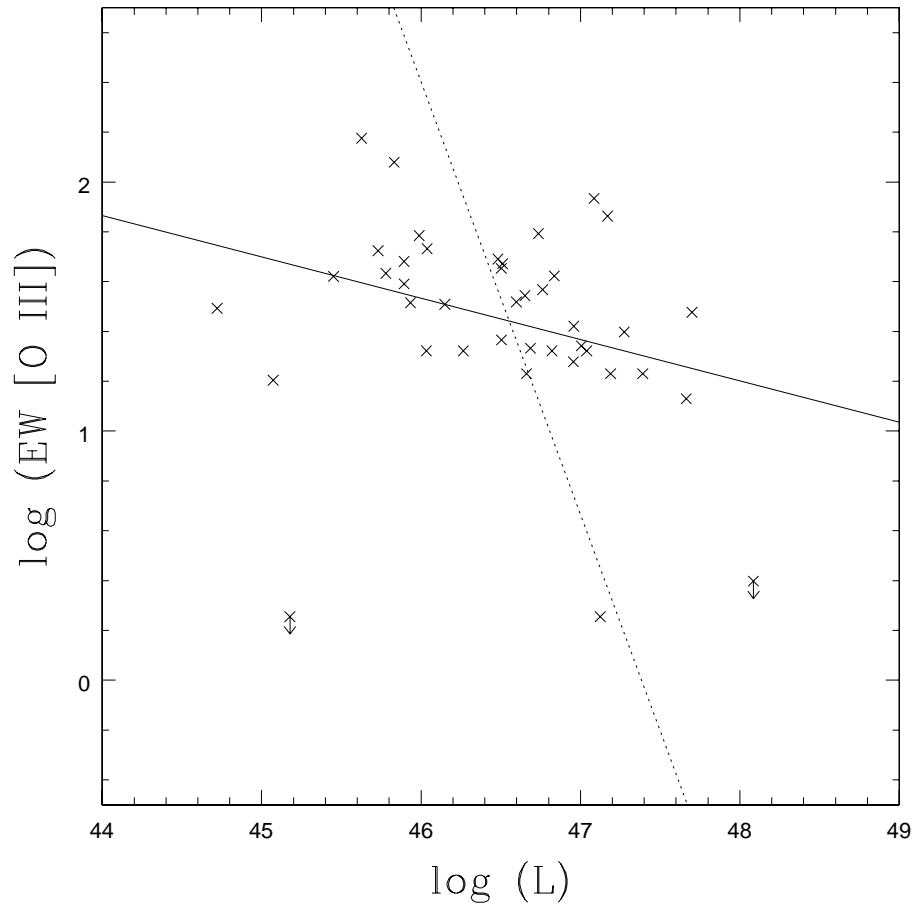
Figure 4.6 There is a strong anti-correlation between [O III] and L for the flat spectrum radio loud QSOs sample. The solid line is the regression result for EW([O III]) on L and the dashed line is the regression result for L on EW([O III]).

90

luminosity QSOs, especially for radio quiet QSOs with relatively strong optical
Fe II emission lines. Although that was not [O III] Baldwin Effect by itself, if
we consider that EW(Hβ) is not correlated with L, [O III] Baldwin Effect
is a natural extension from that result. Brotherton (1996) found a weak
anti-correlation between EW([O III]) and L for a sample of radio loud QSOs.
However, Boroson and Green (1992) did not find significant [O III] Baldwin
Effect probably because of the limited luminosity range of their sample. This
study provides the most conclusive evidence for the [O III] Baldwin Effect on
a variety of QSOs and over a large luminosity range.

4.1.3   Luminosity versus Hβ Broad Line Width

In my sample, the bolometric luminosity and FWHM(Hβ) are highly
correlated. The null probability for the correlation is less than 0.1% for the
entire sample as well as for the radio quiet and BAL QSO sub-samples. The
correlation is less pronounced inside the radio loud sub-sample. However, the
radio loud objects' distribution is consistent with the overall trend defined by
the radio quiet QSOs.

Joly, Collin-Souffrin, Masnou and Nottale (1985) noticed a similar
correlation using Hβ and C IV lines, with a slope close to mine. However, as I
will discuss in section 5.1.1, I extend Joly, Collin-Souffrin, Masnou and Nottale
(1985) results in several important ways and provide a different interpretation
based on new BLR size measurements. Veron-Cetty, Veron and Goncalves
(2001) noticed a correlation between Hβ FWHM and Hβ line luminosity in
a sample of Narrow Line Seyfert 1 Galaxies. However, their sample consists
of low luminosity objects and the Hβ line luminosity is not the same as the
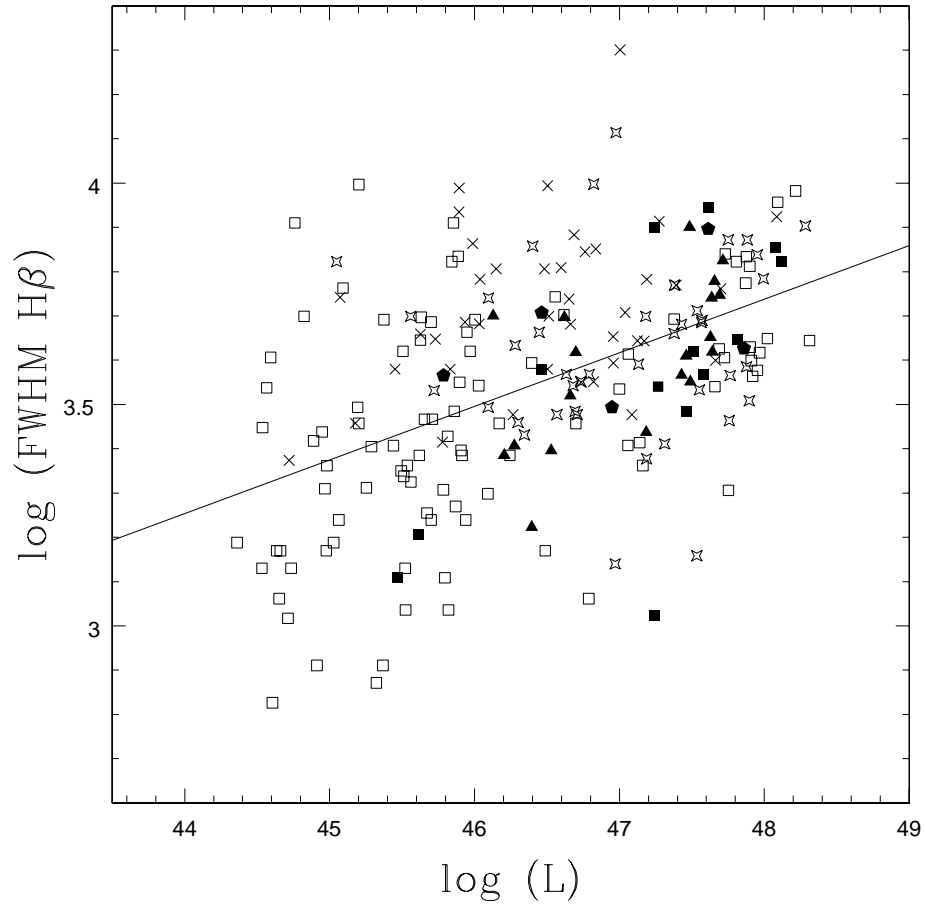bolometric luminosity. Figure 4.7 shows the correlation plot.

Figure 4.7 There is a strong correlation between L and FWHM(Hβ) for all QSOs across a wide range of luminosities. The solid line is the regression result.

92

Since there is no observational or selection bias against low FWHM at high luminosity or high FWHM at low luminosity, this correlation reveals physically meaningful properties in QSOs. This correlation is probably the result of the limited range of Eddington ratios among QSOs (see Section 5.1.1).

4.1.4 Luminosity versus Black Hole Mass

In the QSO sample in this thesis, the black hole mass M_{BH} is strongly correlated with the bolometric luminosity L. Since the beamed continuum in flat spectrum radio loud QSOs could cause over-estimates of both L and M_{BH} (see Section 3.5). They are excluded from this study. The probably for this correlation to arise from unrelated variables is less than 0.1% for all QSOs as well as for the radio loud and radio quiet sub-samples.

Corbett et al.   (2003); Netzer   (2003) found a mass to luminosity relationship exists among QSOs. My results support those findings. Consistent with Netzer   (2003), the M_{BH} on L log-log regression line for the $M_{\mathrm{BH}} \propto L^{\beta}$ relationship for the entire sample yields a slope of $\beta = 0.9$ (Figure 4.8). For all QSOs excluding flat spectrum radio loud QSOs, the regression lines for both M_{BH} on L and vice versa are as follows.

$$\log(M_{\mathrm{BH}}) = (-34.06 \pm 1.59) + (0.92 \pm 0.03) \times \log(L).$$

$$\log(L) = (38.82 \pm 0.28) + (0.88 \pm 0.03) \times \log(M_{\mathrm{BH}}).$$

The radio loud QSOs, indicated by red symbols in Figure 4.8, are displaced to have larger M_{BH} compared with radio quiet and BAL QSOs of the same luminosity. In fact, almost all radio loud objects are located above the

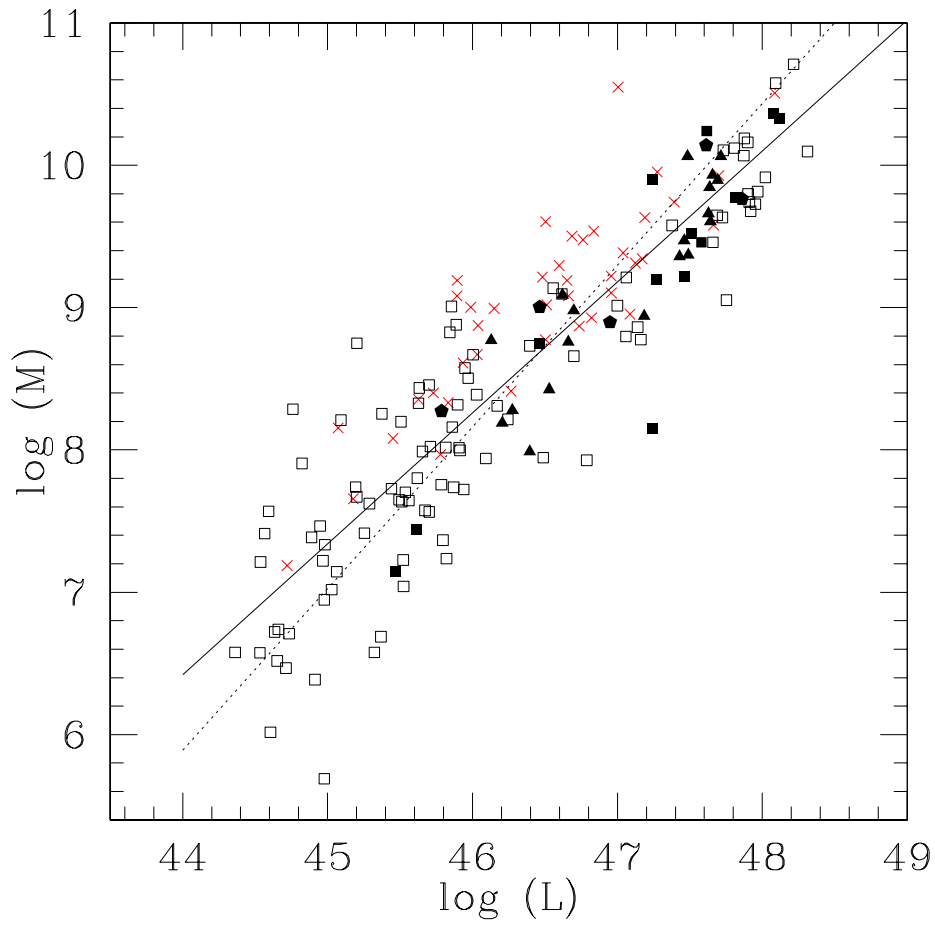Figure 4.8 The L versus $M_{\rm BH}$ correlation for all QSOs. The solid line is the regression result for $M_{\rm BH}$ on L and the dashed line is the regression result for L on $M_{\rm BH}$. The red symbols are steep spectrum radio loud QSOs.).

EW([O III]) on L regression line. That suggests the radio properties of QSOs are associated with the black hole mass and there is no obvious threshold mass to turn on the radio emission (Lacy et al. 2001).

The powerlaw slope β for M_{BH} over L is expected to be 1 if all QSOs, on average, have the same Eddington accretion ratio. A slope below 1 indicates that the M_{BH} increases slower than L, suggesting higher Eddington ratio for more luminous objects. Since the radio loud QSOs have the smallest slope, they ought to have the strongest L/L_{Edd}— L dependency (see section 4.1.5).

Although luminosity is a contributing factor in the reverberation formula I used to calculate M_{BH}, I do not expect the M_{BH} calculation method itself would give rise to the M_{BH}— L relationship. M_{BH} is more sensitive to FWHM(Hβ) ($M_{BH} \propto v_{FWHM}^2$) than to L ($M_{BH} \propto L^{0.66}$). In this sample, the FWHM(Hβ) spans 1.5 orders of magnitudes and L spans close to 5 orders magnitudes. That results in similar ranges of v_{FWHM}^2 and $L^{0.66}$. If there were no intrinsic correlation between L and M_{BH}, the FWHM(Hβ) factor could introduce scatter, which reduces any artificial correlation introduced by the M_{BH} calculating formula. However, instead of canceling out the M_{BH}— L correlation, FWHM(Hβ) is positively correlated with L and hence enhances the M_{BH}— L correlation.

Note that the M_{BH}— L correlation might not hold true for low luminosity AGNs. The low luminosity radio galaxies and BL Lac objects, which are not selected in this QSO sample, could have low Eddington ratios and high black hole mass, and hence reduce the strength of the correlation (Netzer 2003; Woo and Urry 2002).

4.1.5 Luminosity versus Eddington Accretion Ratio

Figure 4.9 shows the Eddington ratio calculated from L and FWHM(Hβ). The arrows at the lower right corner of Figure 4.9 show the possible correction for flat spectrum radio loud QSOs (section 3.5). Most QSOs have Eddington ratios from 0.1 to 1 (see more in section 5.1.1). There is a positive correlation between L and L/L_{Edd} in my QSO sample although the slope is shallow. For all objects and the radio loud QSO sub-sample, the probability for this correlation to arise from random variables is less than 0.1%. For the radio quiet QSO sub-sample, the correlation is only at a 5% significance level. I divide the sample into two groups: a high luminosity group with $L > 10^{47} erg/s$ and a low luminosity group with $L < 10^{47} erg/s$. The high luminosity sample has a mean $log(L/L_{\mathrm{Edd}})$ of -0.17 ± 0.04 and the low luminosity sample has a mean value of -0.42 ± 0.04.

4.2 The BGEV1 Relationship

In this section, I study properties in the BGEV1 relationship. Although luminosity is not a dominant component in BGEV1, some BGEV1 correlations and their interpretations are dependent on luminosity. To account for luminosity effects in the analysis, I used different color symbols to represent QSOs with different luminosity.

- Blue symbols are for QSOs with $\log L < 46$.

- Black symbols are for QSOs with $46 < \log L < 47$.
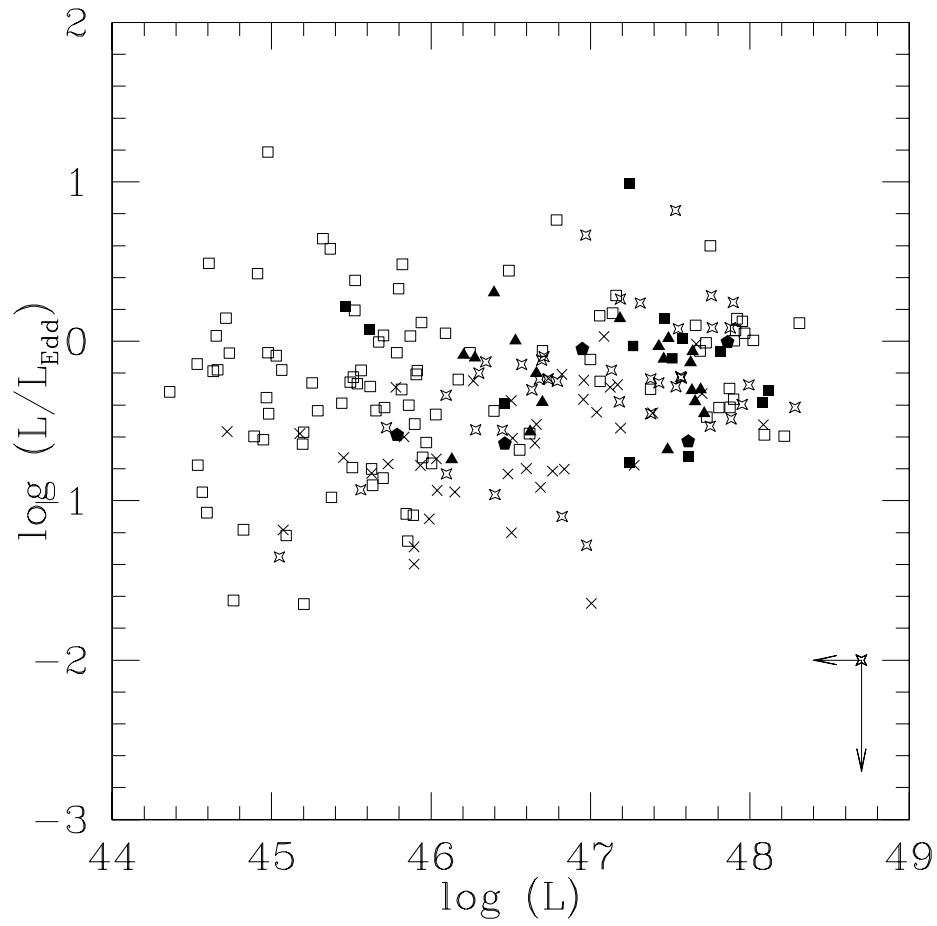
- Red symbols are for QSOs with $\log L > 47$.

Figure 4.9 The L versus L/L_{Edd} correlation for all QSOs.

4.2.1   Anti-correlation between [O III] and Fe II Emission Lines

The newly observed high luminosity objects in my sample (red symbols) show a strong anti-correlation between optical [O III] and Fe II emission line strength. The correlation trends defined by high luminosity objects (red symbols), middle luminosity objects (black symbols) and low luminosity objects (blue symbols) are the same (Figure 4.10). That result extends the BGEV1 relationship from low luminosity QSOs (Boroson and Green 1992) to a wide range of luminosities. To avoid the built-in correlation caused by the common continuum divider, I did not directly correlate the equivalent widths of the two lines. Instead, I correlate the equivalent width [O III] against the Fe II/Hβ flux ratio. As I had mentioned before, the measured Fe II flux is integrated between wavelength 4434Å and 4684Å using the original unbroadened template.

The same strong anti-correlation is shown within each of the sub-samples: radio quiet QSOs, radio loud QSOs and BAL QSOs. The probability for the anti-correlation to rise from random underlying distributions is less than 0.1% for each of the sub-sample as well as for the entire sample. However, different classes of QSOs do not occupy the same range of emission line properties. BAL QSOs tend to have very weak (in most cases, undetected) [O III] lines and strong optical Fe II lines. On the other end of the relationship, radio loud QSOs tend to have the strongest [O III] lines and the weakest optical Fe II lines. The differences between BAL QSOs and radio loud QSOs along the Fe II/Hβ versus [O III] correlation direction are true for high and low luminosity samples separately as well as for the overall sample. The median value and standard deviation of the [O III] equivalent width and Fe II/Hβ are listed in Table 4.7.
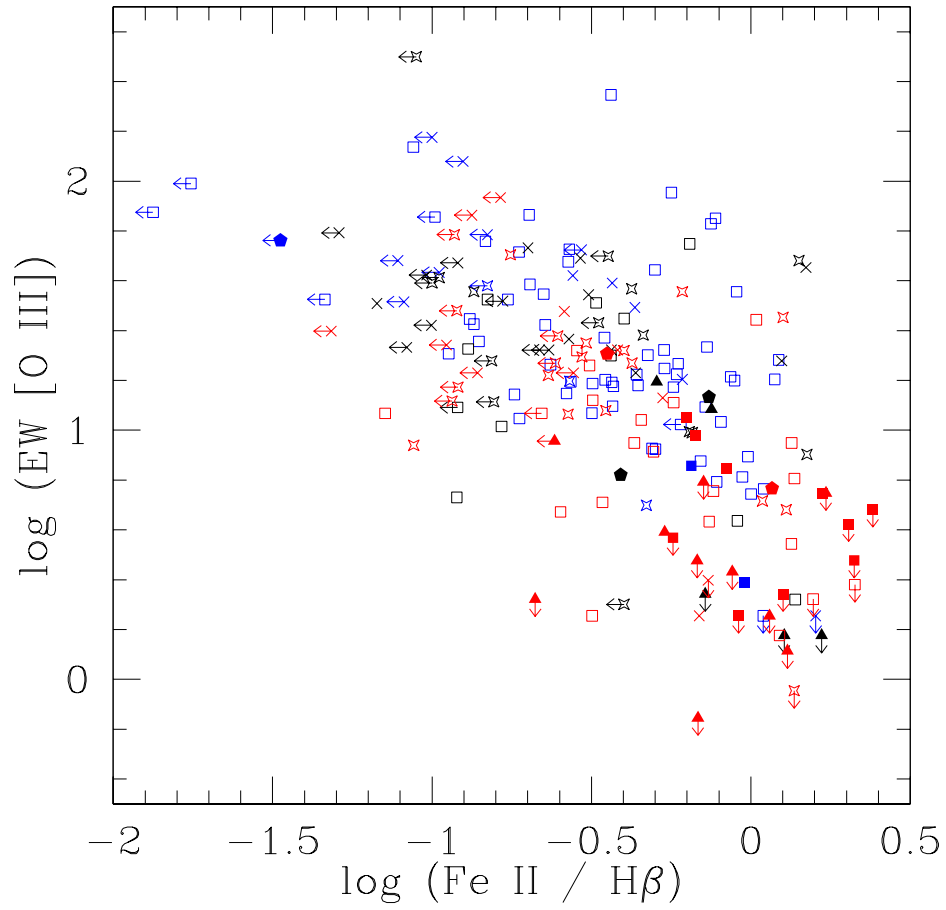
Figure 4.10 There is a strong anti-correlation between [O III] and Fe II/Hβ for all QSOs across a wide range of luminosities. BAL QSOs and radio loud QSOs seem to occupy the two ends of the anti-correlation.

Table 4.7.   Median values and standard deviations of the [O III] and optical
Fe II/Hβ distributions

	Radio Quiet	Radio Loud	BAL	All
$<$EW([O III])$>$	1.20	1.36	0.62	1.22
σ(EW([O III]))	0.44	0.43	0.40	0.49
$<$Fe II/Hβ$>$	−0.43	−0.56	−0.13	−0.43
σ(Fe II/Hβ)	0.40	0.39	0.36	0.41

[a]All values in this table are in the logarithmic scale

4.2.2   Fe II, Eddington Ratio and Black Hole Mass

The anti-correlation between [O III] and Fe II strengths is a strong rela-
tionship in BGEV1 (Boroson and Green 1992), which is thought to be driven
by the Eddington accretion ratio (Boroson 2002). In this section, I will dis-
cuss how this argument is supported by my sample with expanded luminosity
coverage.

FWHM(Hβ) is thought to be the key BGEV1 factor (Boroson and
Green 1992) that links BGEV1 with black hole and accretion properties,
since FWHM(Hβ) is used to calculate both $M_{\rm BH}$ and $L/L_{\rm Edd}$. So, I correlate
Fe II/Hβ with FWHM(Hβ) for my sample. There is a strong anti-correlation
between Fe II/Hβ and FWHM(Hβ) (see Figure 4.11). However, the correlation
is primarily caused by the fact that radio loud and radio quiet QSOs occupy dif-
ferent regions. Within the radio quiet QSO sub-sample, such correlation does
not exist. A major source of scatter in this anti-correlation is the differences
in QSO luminosities. As seen from the color-coded Figure 4.11 QSOs with dif-
ferent luminosity range (i.e., different symbol colors) are displaced along the

direction perpendicular to the overall direction of the anti-correlation. This scatter is expected from the BGEV2 correlation between FWHM(Hβ) and L, which is orthogonal to BGEV1.

Figure 4.12 plots Fe II/Hβ against M_{BH}. Overall, there is no correlation between those two quantities. However, closer inspection of the color-coded diagram reveals that within each luminosity bin, there is an anti-correlation. QSOs with different luminosities are displaced perpendicular to the anti-correlation direction. Hence, the overall anti-correlation is destroyed by the scatter introduced by the large luminosity range. The displacement direction of QSOs with different luminosities is consistent with the tight correlation between L and M_{BH} (Figure 4.8). This result suggests that M_{BH} is linked to both L and the physical mechanism that drives Fe II/Hβ. Due to the relationship $L = M_{\mathrm{BH}} \times L/L_{\mathrm{Edd}}$, Fe II/H$\beta$ is probably closely linked to L/L_{Edd}. To test this hypothesis, I plot Fe II/Hβ against L/L_{Edd}.

Figure 4.13 shows a strong correlation between Fe II/Hβ and L/L_{Edd}, which is calculated from L and FWHM(Hβ). This correlation is significant within the radio loud QSO sub-sample and in the entire combined sample. Radio loud QSOs mainly occupy the low L/L_{Edd} end while BAL QSOs and radio quiet QSOs share the other end of the relationship. Most importantly, the luminosity is no longer a source of scatter in this correlation. Instead, QSOs with different luminosities all display a consistent Fe II/Hβ versus L/L_{Edd} correlation.

The analysis in this section shows that the Fe II/Hβ, a key BGEV1 component, is linked to L/L_{Edd} not M_{BH} or L.
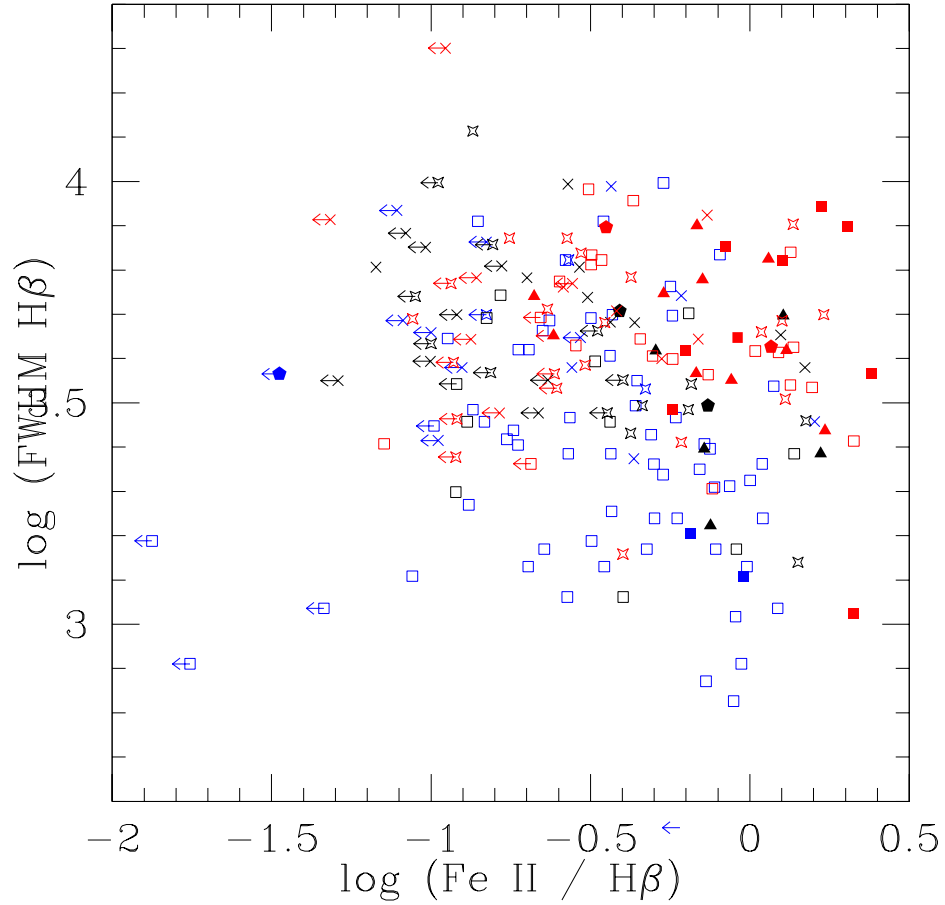
Figure 4.11 The anti-correlation between Fe II/Hβ and FWHM(Hβ). It is likely to be caused by selection effect since radio loud QSOs selected at high luminosity tend to have both high FWHM(Hβ) and weak Fe II/Hβ. QSOs with different luminosities are displaced perpendicular to the direction of the anti-correlation, causing scatter.
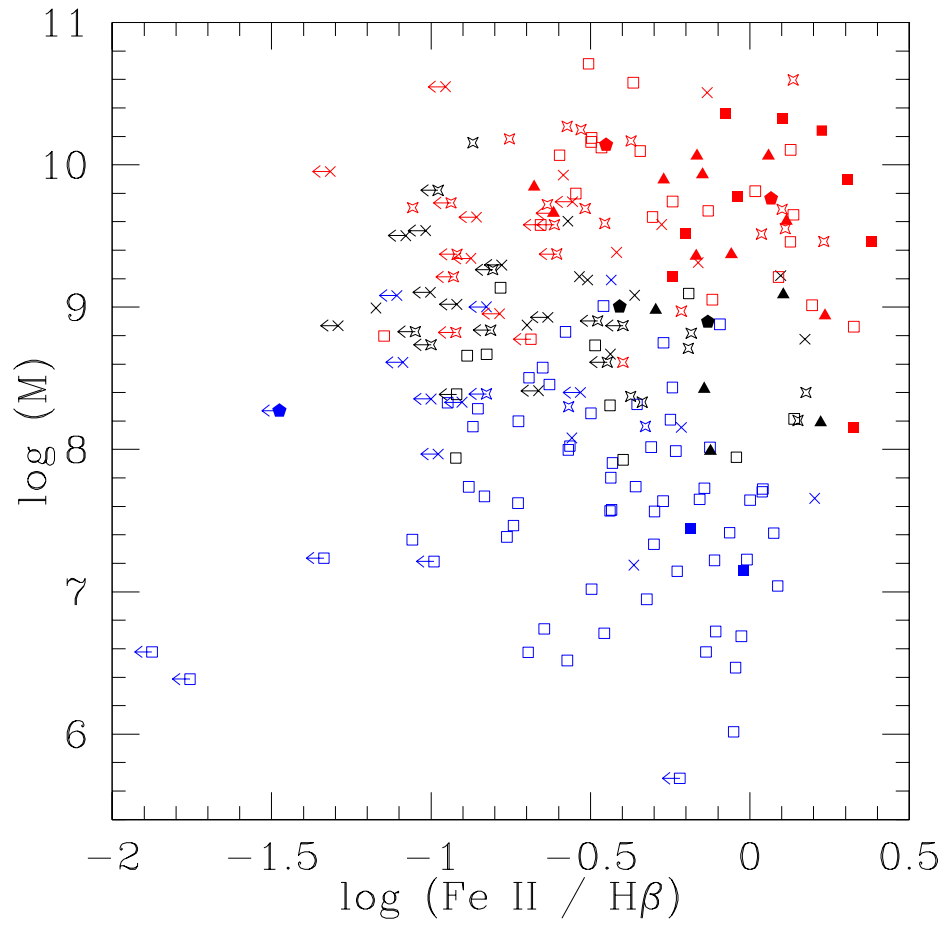
Figure 4.12 There is no correlation between Fe II/Hβ and M_{BH}.
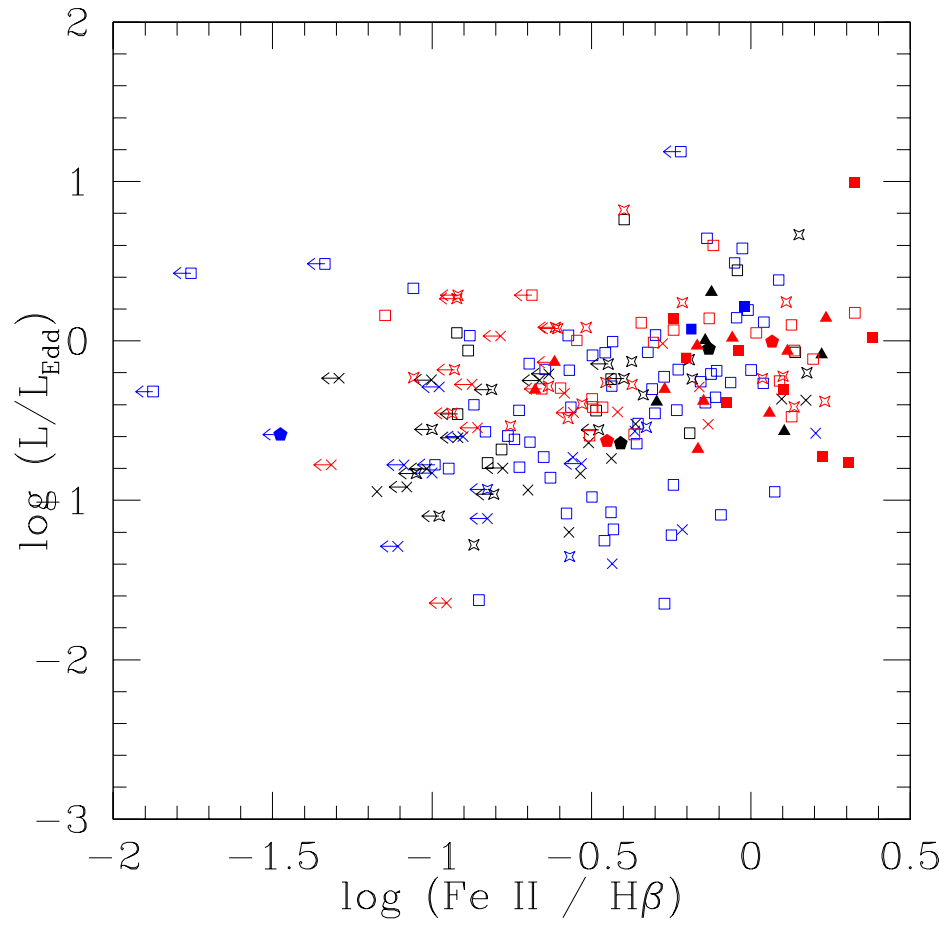
Figure 4.13 The correlation between Fe II/Hβ and L/L_{Edd}. All types of QSOs lie on the same relationship trend.

4.2.3 [O III], Eddington Ratio and Black Hole Mass

There is no overall correlation between EW([O III]) and FWHM(Hβ) (Figures 4.14). However, within each luminosity range, there is a correlation. The overall correlation is destroyed by the scatter introduced by the displacements of low and high luminosity QSOs along the direction perpendicular to the correlation (i.e., scatter caused by BGEV2).

However, despite the lack correlation between EW([O III]) and FWHM(Hβ), EW([O III]) is still anti-correlated with both M_{BH} and L/L_{Edd}. Figure 4.15 shows the anti-correlation between EW([O III]) and M_{BH}. Low luminosity QSOs occupy the high [O III] and low M_{BH} part of the plot. High luminosity QSOs occupy the low [O III] and high M_{BH} part of the plot. That strongly indicates that the EW([O III]) versus M_{BH} anti-correlation is primarily caused by the known EW([O III]) versus L anti-correlation (the [O III] Baldwin Effect).

Figure 4.16 shows the luminosity independent EW([O III]) versus L/L_{Edd} anti-correlation. It is significant in radio quiet, radio loud sub-samples and the entire combined QSO sample. This result is consistent with the link between BGEV1 and L/L_{Edd}.

I notice that although BAL QSOs have extreme [O III] and Fe II properties, their Eddington ratios are less distinguished from the rest of the QSOs. In fact, when BAL QSOs are compared with QSOs of similar luminosities, they do not show higher Eddington ratios at all. This suggests that the link between [O III] and Fe II emission properties and Eddington ratios is indirect. Later in this thesis, I will discuss the possible indirect link (see Sections 5.2.1 and 5.3).
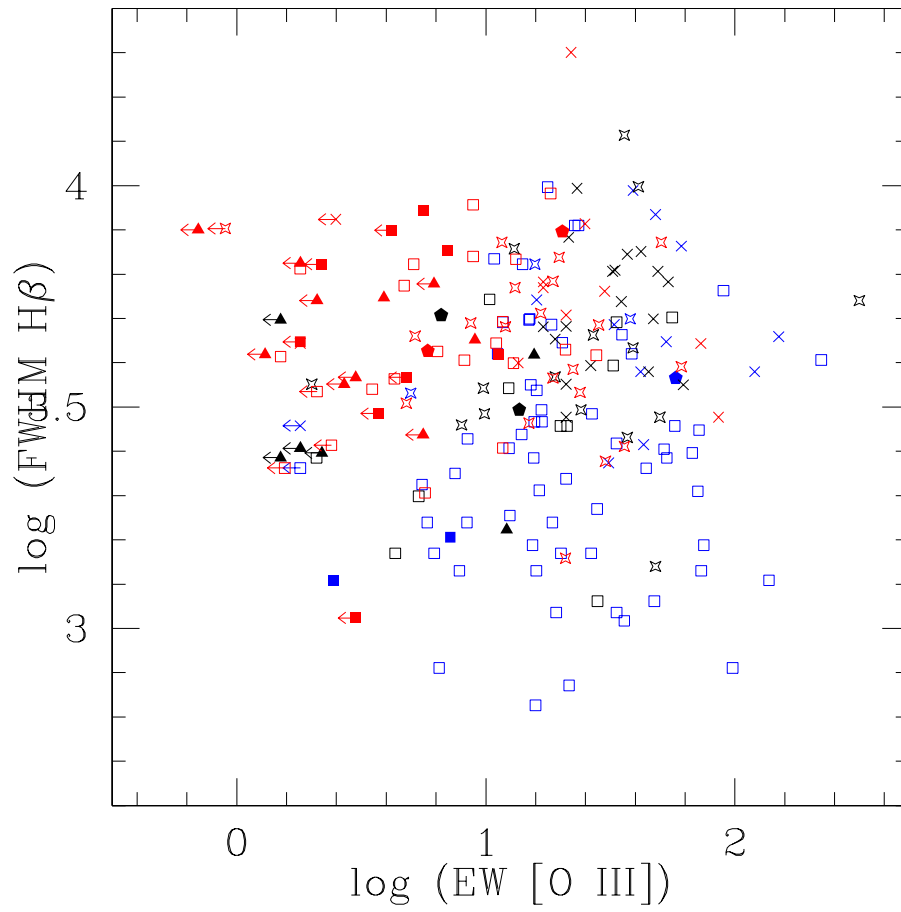
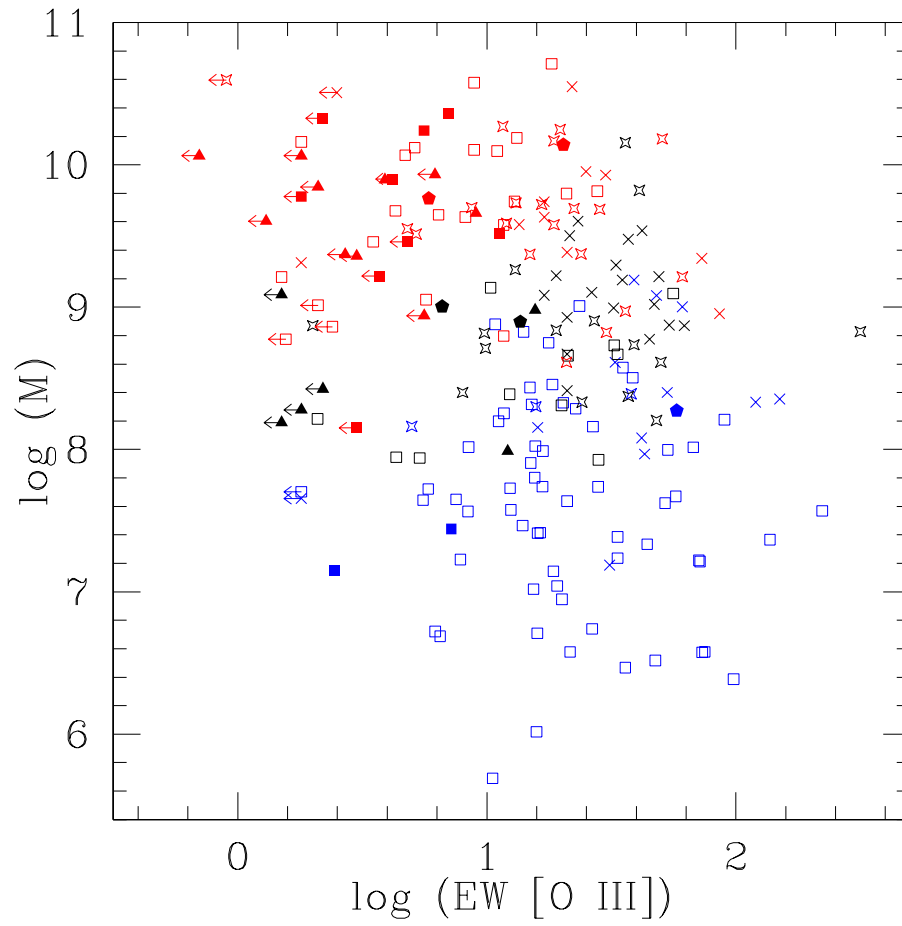Figure 4.14 There is no correlation between EW([O III]) and FWHM(Hβ).

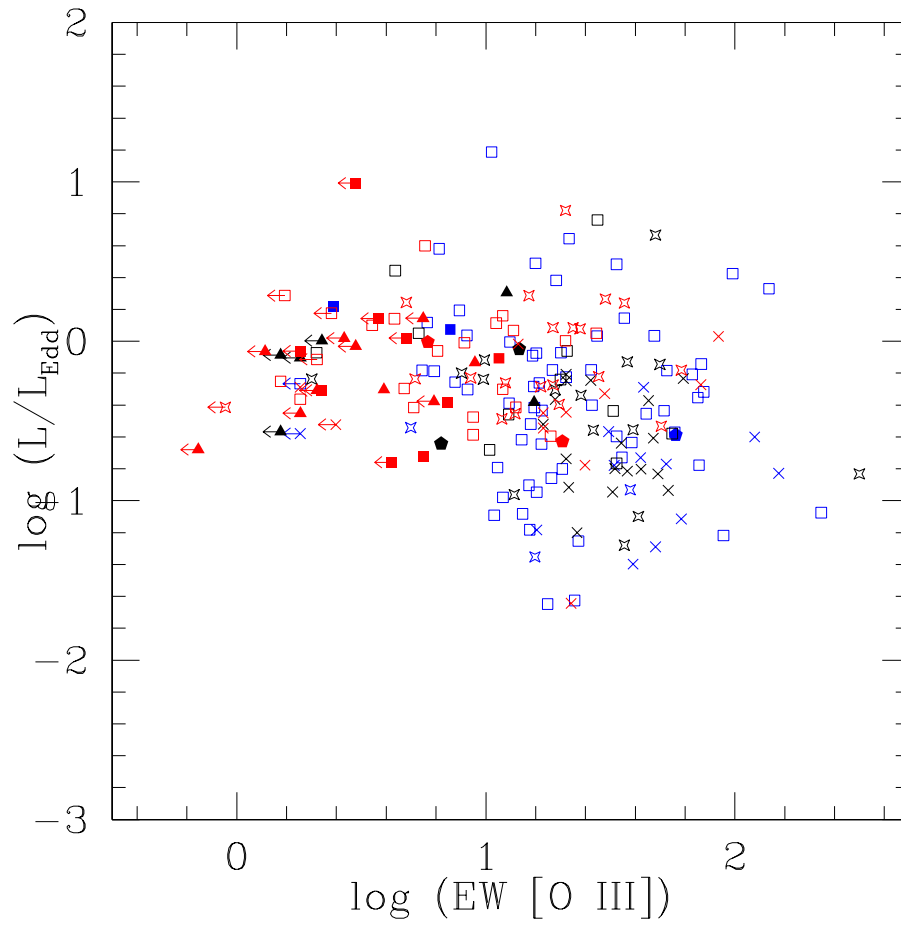Figure 4.15 The [O III] versus M_{BH} anti-correlation.

Figure 4.16 The [O III] versus L/L_{Edd} anti-correlation.

4.2.4 EW(Hβ) and BGEV1

As discussed in Section 4.1.1, BAL QSOs have weak EW(Hβ). That suggests a link between EW(Hβ) and BGEV1. EW(Hβ) is positively correlated with FWHM(Hβ) (see Figure 4.17). The null probability of the EW(Hβ) versus FWHM(Hβ) correlation is less than 1% for the overall sample and the radio quiet non-BAL QSO sub-sample, and less than 0.1% for the radio loud QSO sub-sample. Like the FWHM(Hβ) correlations with EW([O III]) and Fe II/Hβ, the scatter in the EW(Hβ) versus FWHM(Hβ) correlation is partly introduced by the displacement of high and low luminosity QSOs perpendicular to the correlation direction due to the strong positive correlation between FWHM(Hβ) and L (BGEV2).

In Figure 4.18, QSOs in each luminosity bin show a correlation between EW(Hβ) and M_{BH}. However, the overall correlation is destroyed by the scatter introduced by luminosity. Similar to the Fe II/Hβ versus M_{BH} plot, this plot suggests that M_{BH} is linked to both L and an underlying mechanism driving EW(Hβ) changes, possibly L/L_{Edd}.

Indeed, Figure 4.19 shows the luminosity independent anti-correlation between EW(Hβ) and L/L_{Edd}. The anti-correlation is significant in the radio quiet non-BAL QSO sub-sample as well as in the overall sample with less than 0.1% null probability for both samples. This anti-correlation suggests that, contrary to Boroson and Green (1992)'s results, EW(Hβ) is a strong BGEV1 component.

As a BGEV1 component, EW(Hβ) is strongly correlated with EW([O III]), and is anti-correlated with Fe II/Hβ (Figures 4.20 and 4.21). The EW(Hβ) versus EW([O III]) correlation is probably caused by multiple factors:
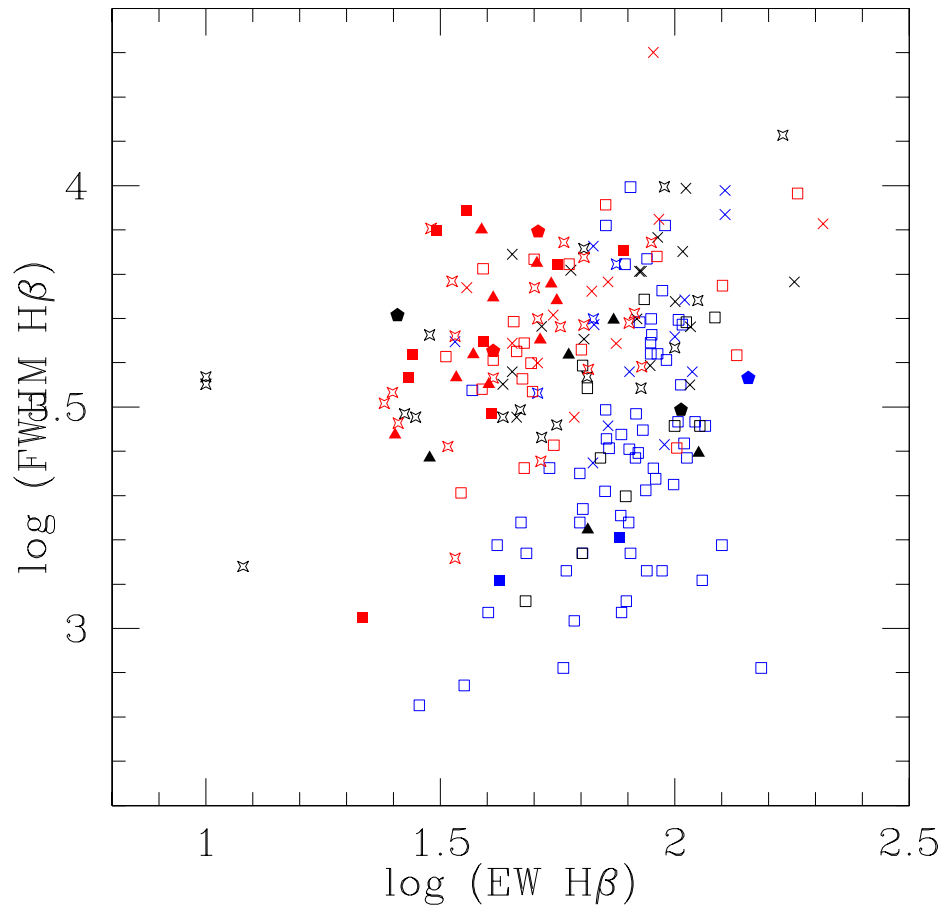
Figure 4.17 The correlation between EW(Hβ) and FWHM(Hβ).

110
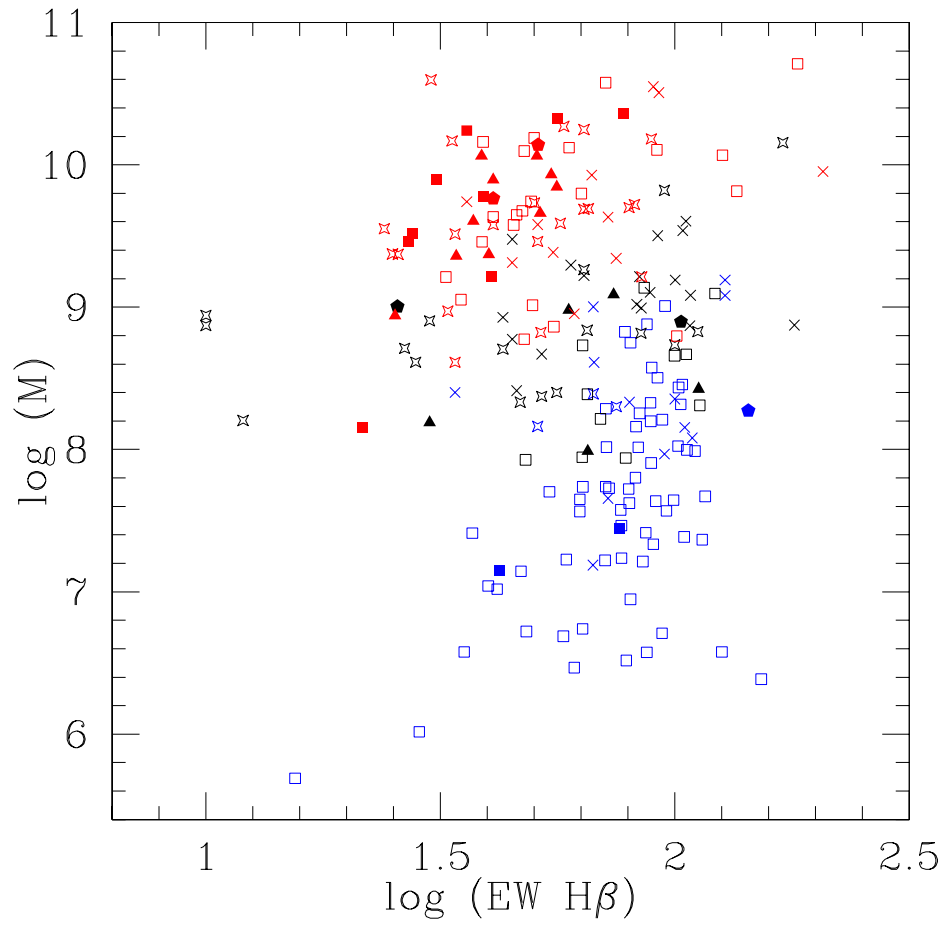
Figure 4.18 The lack of correlation between EW(Hβ) and M_{BH}.
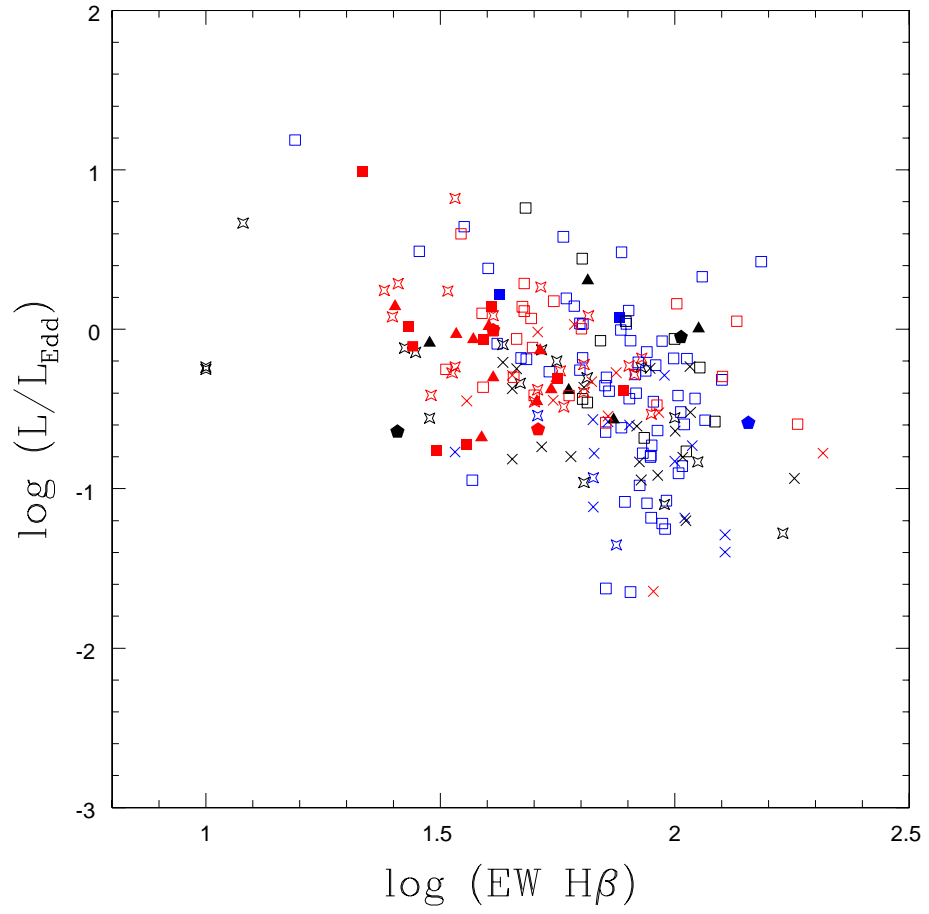
Figure 4.19 The anti-correlation between EW(Hβ) and L/L_{Edd}.

112

- They are both anti-correlated with L/L_{Edd}.

- They are both anti-correlated with L. In Figure 4.20, we can see that QSOs with different luminosity are generally separated along the correlation trend in.

- Furthermore, the common continuum divider in EW([O III]) and EW(Hβ) might artificially enhance the correlation.

The anti-correlations between EW(Hβ) and Fe II/Hβ is significant in all sub-samples. However, since Fe II/Hβ is EW(Fe II) divided by EW(Hβ), a built-in anti-correlation between the Fe II/Hβ and EW(Hβ) is expected. EW(Hβ) is not correlated with EW(Fe II).

4.3   Radio Properties

The QSO sample in this thesis contains both radio loud and radio quiet QSOs. That allows us to study the relationship between QSO radio properties, black hole accretion properties and optical/IR emission properties. The results are reported in this section.

4.3.1   Radio Loudness versus Black Hole Mass

Radio loud and radio quiet QSOs have different black hole mass and Eddington ratio characteristics. Consistent with (Laor 2000; McLure and Dunlop 2001), my radio loud QSOs have higher black hole masses. The mean logarithmic value of M_{BH} for radio loud objects is 9.117 ± 0.0782 and that of radio quiet objects is 8.191 ± 0.114. A possible selection bias is that since radio loud QSOs have low space density, they are more likely to be selected at

Figure 4.20 The correlation between EW([O III]) and EW(Hβ).
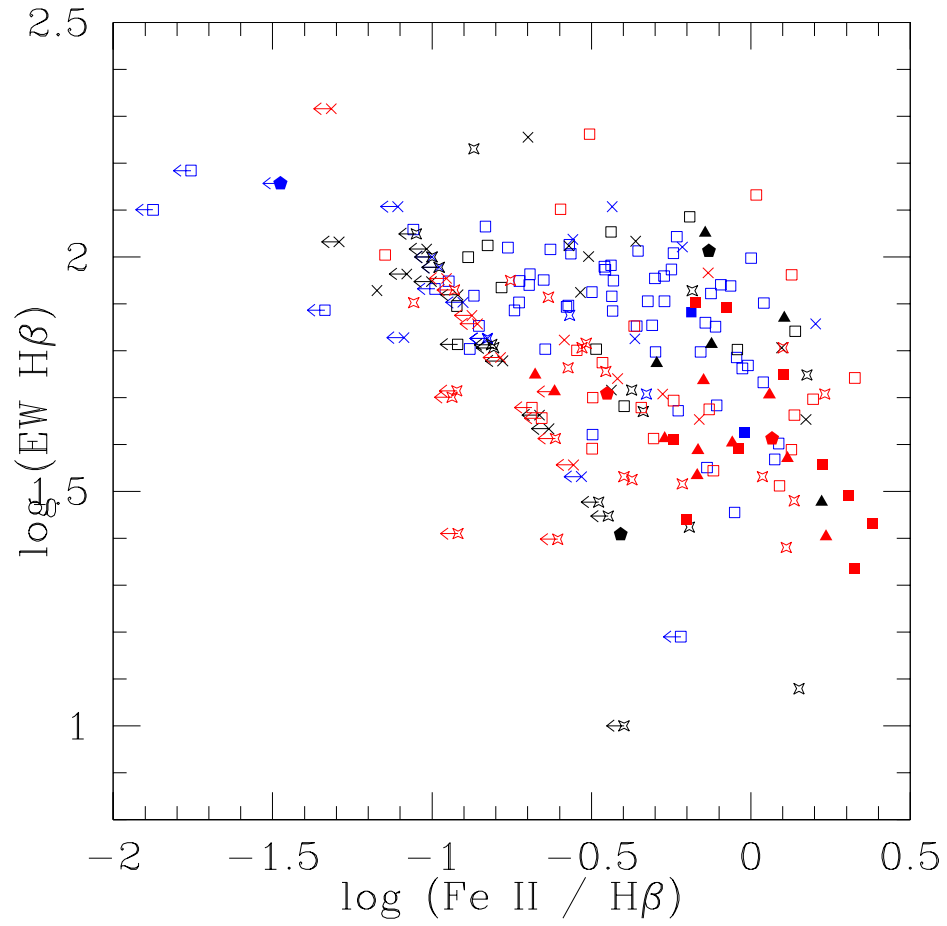
Figure 4.21 The anti-correlation between Fe II/Hβ and EW(Hβ).

115

high redshift, which corresponds to larger volume of space. However, from the results in section 4.1.4 (Figure 4.8), radio loud QSOs are displaced to higher M_{BH} for a given L, compared with radio quiet and BAL QSOs. So, the above mentioned selection effect does not change my conclusions.

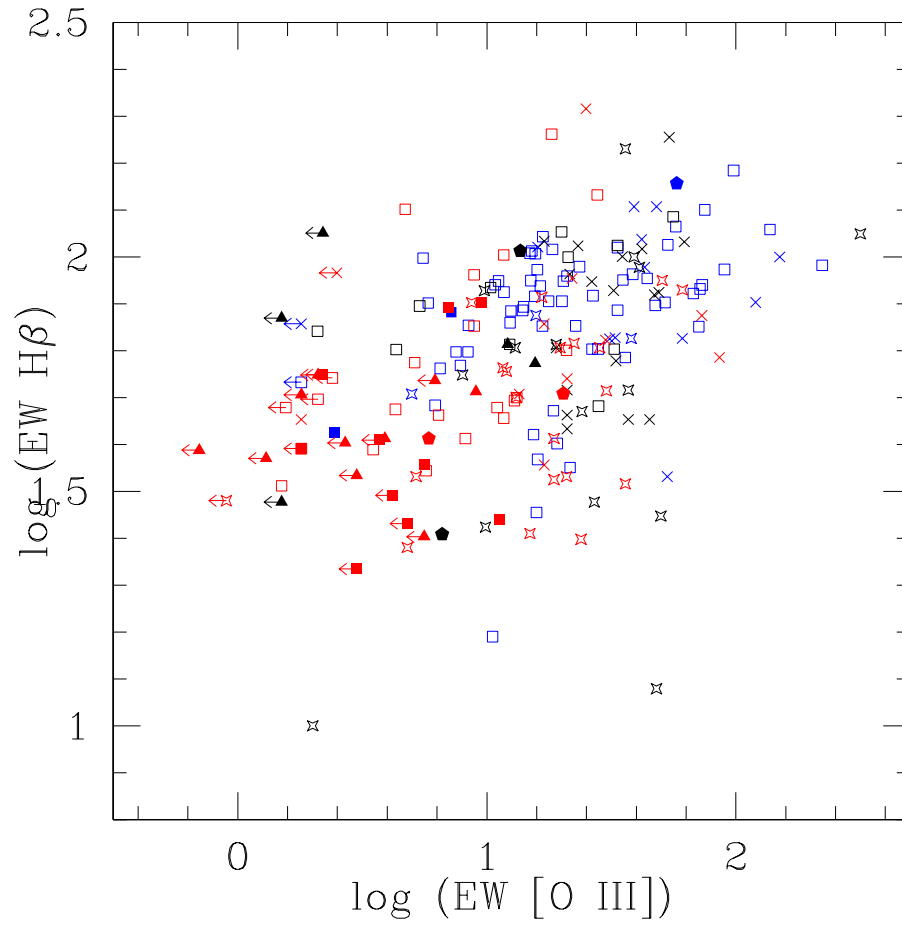Radio loud objects have smaller Eddington ratio. The mean logarithmic value of L/L_{Edd} for radio loud objects is -0.475 ± 0.050 and that for radio quiet objects is -0.237 ± 0.043. This actually goes against the selection effect since my sample shows a slight increase in L/L_{Edd} with increasing L. Given a limited range of L, a smaller L/L_{Edd} corresponds to a larger M_{BH}. Hence, it is still consistent with the hypothesis that radio loud QSOs have larger M_{BH}.

Within the radio loud sub-sample, the radio loudness R^* is correlated with both luminosity and Eddington ratio (Figures 4.22 and 4.23), but is anti-correlated with EW(Hβ) (Figure 4.24). The null probability for each of those three correlations is around 2% respectively. For the steep spectrum radio loud QSO sub-sample, R^* is correlated with luminosity (null probability of 2%) and anti-correlated with EW(Hβ) (null probability of 3%). For the flat spectrum radio loud QSOs, R^* is correlated with L/L_{Edd} (null probability of 6%).

The correlation between R^* and L for the entire radio loud QSO sample is primarily a result of flat spectrum objects occupying the high L and high R^* region of Figure 4.22. That correlation is explained by relativistic beaming since beamed synchrotron radiation raises both radio and bolometric flux levels but it affects radio flux more (see next section). The R^* versus L correlation for steep spectrum radio loud QSO sub-sample suggests that R^* could be a measure of beaming and orientation angle for those objects.

Although radio loud QSOs tend to have large EW([O III]) and small Fe II/Hβvalues, the radio loudness is not correlated with those two BGEV1

116
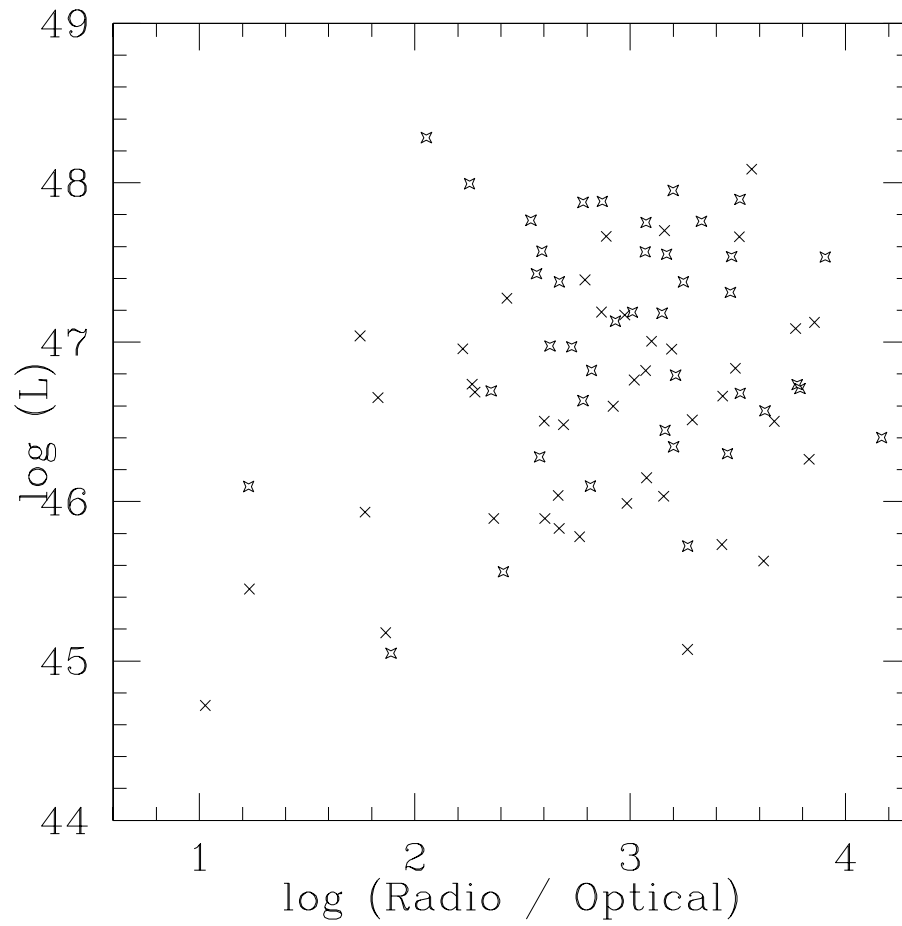
Figure 4.22 The radio loudness versus L correlation.
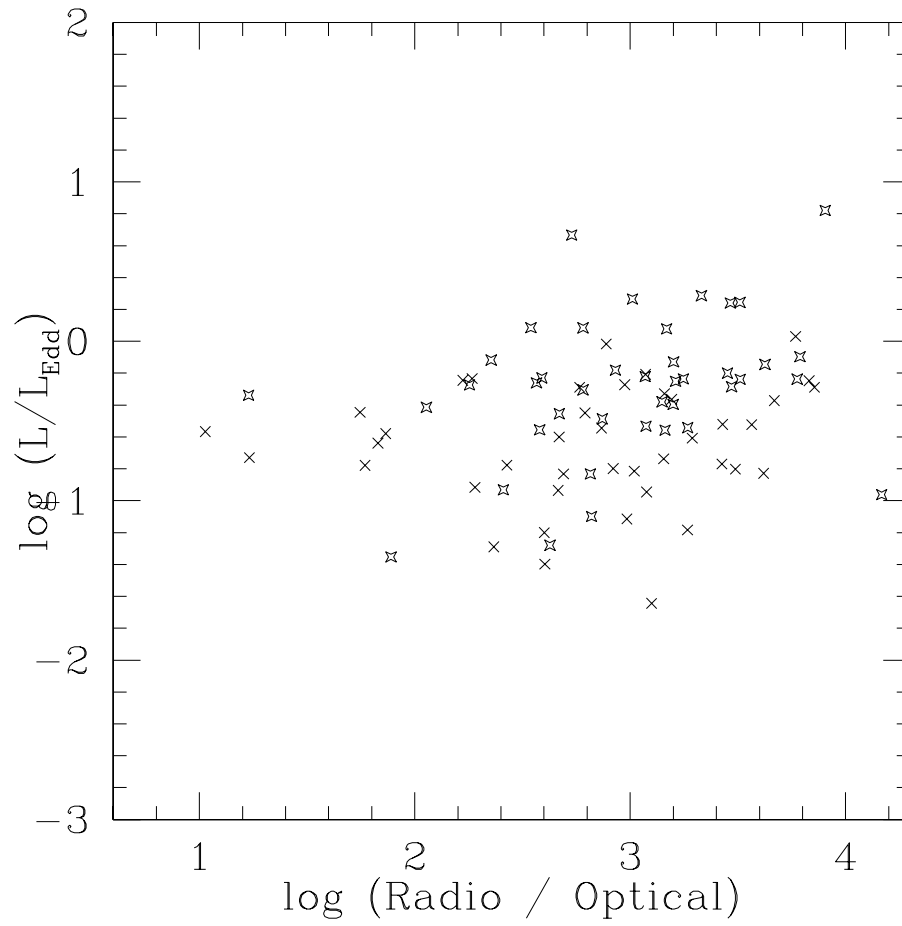
Figure 4.23 The radio loudness versus L/L_{Edd} correlation.
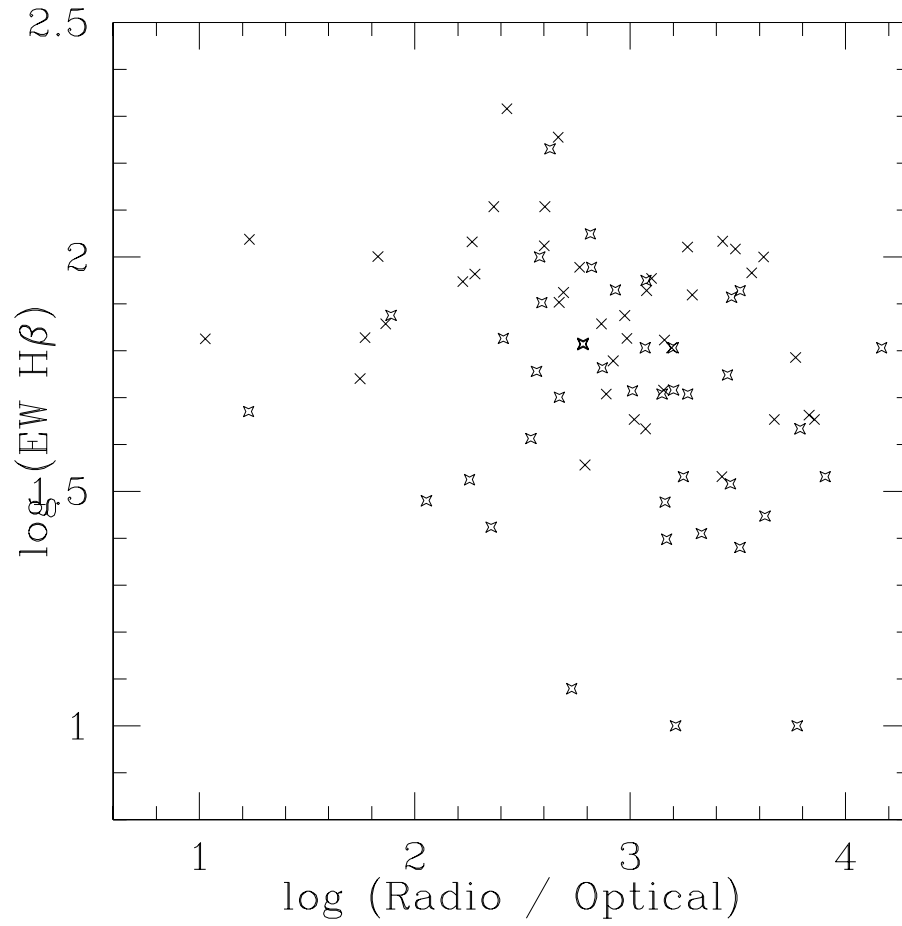
Figure 4.24 The radio loudness versus EW(Hβ) anti-correlation.

indicators among radio loud objects. Within the radio loud QSO sub-sample, the radio loudness is not correlated with black hole mass either.

4.3.2 Radio Spectral Index and Orientation

As I had discussed in section 3.5, the radio spectral index could indicate the orientation of the jet of the QSO black hole. The face-on jet produces beamed radiation and has flat radio spectrum.

My data shows that the radio spectral index correlates with the observed bolometric luminosity (Figure 4.25). The probability for this correlation to rise from random underlying distribution is 0.1%. That indicates that the beamed synchrotron radiation not only affects the radio spectrum but also is apparent in optical and IR parts of the spectrum. The mean value of $\log L$ is 46.5 ± 0.1 for steep spectrum objects and 47.0 ± 0.1 for flat spectrum objects. The difference is slightly larger than the ~ 0.3 correction I got from section 3.5. However, this sample is skewed toward the brighter flat spectrum objects at high redshift. Hence it could exaggerate the luminosity differences between flat and steep spectrum objects.

The beamed luminosity also causes flat spectrum objects to have smaller emission equivalent widths. The radio spectral index is anti-correlated with EW([O III]) and EW(Hβ), with a null probability of 0.5% and 0.1% respectively.

The face-on orientation could cause us to under-estimate the virial velocity in the BLR region. That is supported by the anti-correlation (null probability 0.5%) between the radio spectral index and the FWHM(Hβ) (Figure 4.26). The mean value of $\log(FWHM)$ is 3.71 ± 0.03 for steep spectrum objects and 3.63 ± 0.03 for flat spectrum objects. This is substantially smaller
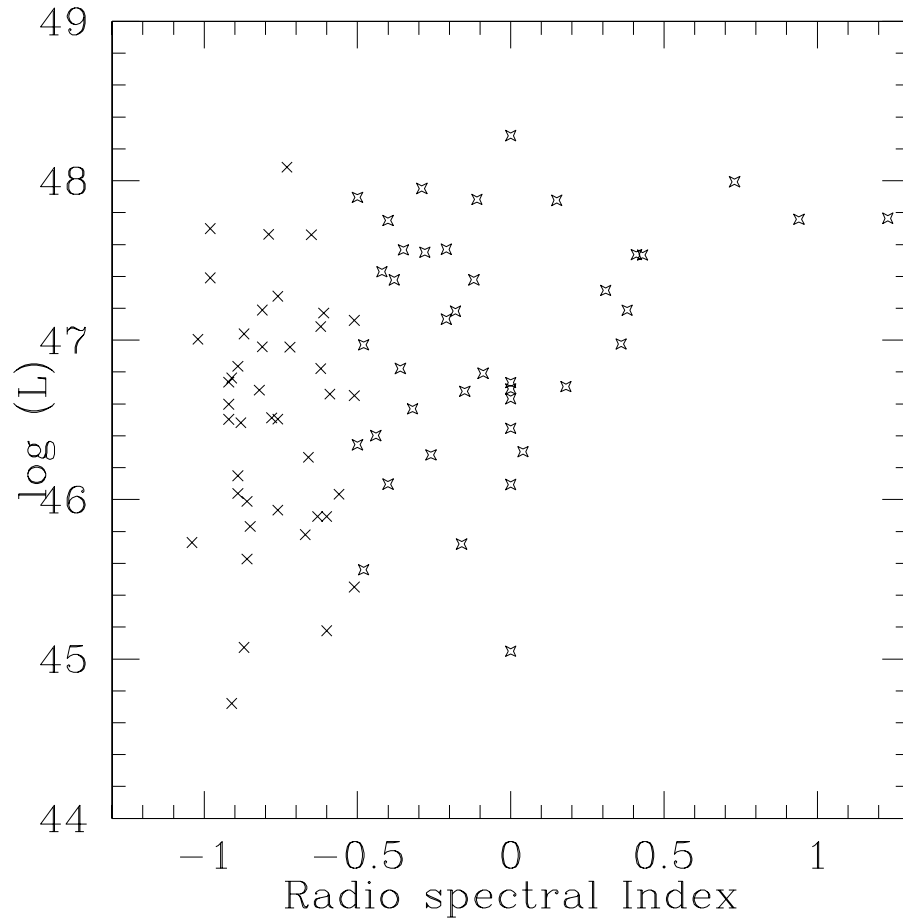
Figure 4.25 The radio spectral index versus L correlation.

than the ~ 0.3 correction in section 3.5, which is derived from objects with extreme beaming such as superluminal objects and optically violent variables.

For objects with flat radio spectra, the combined effect of over-estimated luminosity and under-estimated FWHM(Hβ), causes us to over-estimate the Eddington ratio. Indeed, I observed a correlation between the radio spectral index and the Eddington ratio (null probability less than 0.1%, Figure 4.27). The average value for $\log(L/L_{\mathrm{Edd}})$ is -0.62 ± 0.06 for steep spectrum objects and -0.30 ± 0.07 for flat spectrum objects.

The Fe II/Hβ is a BGEV1 property that is not biased by beaming. I do not find correlation between radio spectral index and Fe II/Hβ. That indicates orientation is not linked to BGEV1 and the intrinsic L/L_{Edd} corrected for beaming.

4.4 Absorption Line Properties

There are 34 BAL QSOs in my sample. All of them have high ionization broad absorption lines such as C IV. Among them, 17 have confirmed broad low ionization absorption lines such as Mg II $\lambda 2798$ or Al III $\lambda\lambda 1855,1863$. Part of my research goal is to compare their emission line properties with non-BAL QSOs. As we have seen, BAL QSOs tend to have extremely weak [O III] emission and strong Fe II emission. However, their black hole mass and Eddington ratios are not significantly different from non-BAL QSOs in the same luminosity range.

I tried to correlate BAL absorption line equivalent widths and maximum velocity v_{max} with [O III], Fe II line strengths, black hole masses and Eddington ratios. I do not find any significant correlations. However, I have

122
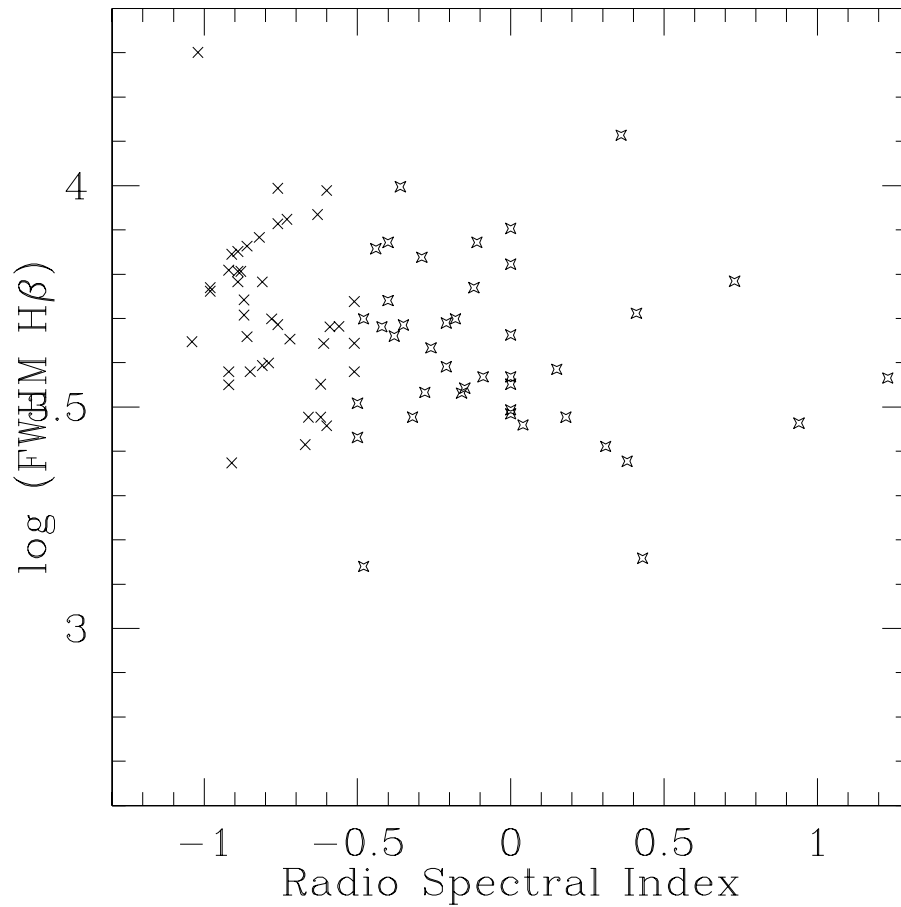
Figure 4.26 The radio spectral index versus FWHM(Hβ) anti-correlation.
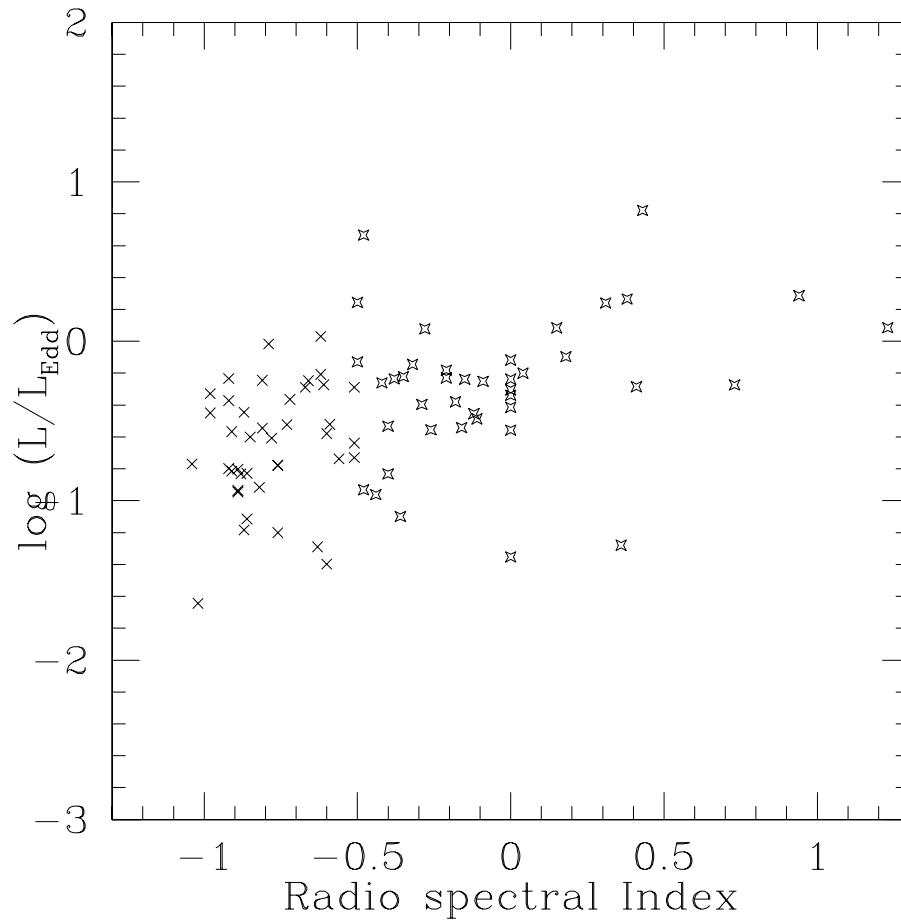
Figure 4.27 The radio spectral index versus L/L_{Edd} correlation.

to note that my sample only have a limited range of BAL absorption equivalent widths and v_{max}. The range of emission line strengths and black hole masses among BAL QSOs is also small compared with the general QSO sample. That might just indicate that all BAL QSOs have similar central engine properties.

Chapter 5

Discussion and Interpretation

5.1 Accretion Properties

5.1.1 QSO Accretion Rate

One of the most prominent results that emerge from my analysis is the strong correlation between FWHM(Hβ) and bolometric luminosity. This correlation has been noticed before in the work of Joly, Collin-Souffrin, Masnou and Nottale (1985) for lower luminosity AGNs, including QSOs, Seyfert 1 galaxies and broad line radio galaxies. I extended the results to high luminosity QSOs. Joly, Collin-Souffrin, Masnou and Nottale (1985) used the Hβ width for low luminosity objects and the C IV width for high luminosity objects. HST observations made in the 1990's had indicated that the Hβ and C IV broad lines do not have the same width (Vestergaard 2002). Hence, the results derived from the mixture of Hβ and uncorrected C IV lines need to be updated.

Since the black hole mass and Eddington ratio can both be calculated from FWHM(Hβ) and L, I can overlay contours of constant black hole masses and Eddington ratio on the FWHM(Hβ) versus L plot. As we can immediately see from Figure 5.1, the correlation is primarily a result of the fact that most QSOs in my sample are within a small range of Eddington ratios from 0.1 to 10. These values do not agree with the AGN Eddington ratio calculated by Joly, Collin-Souffrin, Masnou and Nottale (1985) using photo-ionization models. Assuming AGN broad emission line region gas clouds have typical dimension-

less ionization parameter $U \sim 10^{-2}$ and electron density $n_e \sim 10^{10} cm^{-3}$, Joly, Collin-Souffrin, Masnou and Nottale (1985) concluded that most AGNs in their sample have Eddington ratios on the order of 10^{-3}.

However, new reverberation mapping results for low luminosity AGNs (e.g. Peterson et al. 1985; Peterson and Horne 2004) since the late 1980's have indicated that the BLR size might be much smaller than that used by Joly, Collin-Souffrin, Masnou and Nottale (1985). Rees, Netzer and Ferland (1989) calculated that the BLR cloud electron density might be as high as $10^{13} cm^{-3}$. Popovic (2003) applies the Boltzmann plot method to 14 AGNs and found that optically thin Balmer emission line gas in the BLR could reach $n_e \sim 10^{14} cm^{-3}$. Wandel, Peterson and Malkan (1999) used a photo-ionization model with $U n_e \sim 10^{10}$, and calculated the Eddington ratio for low luminosity QSOs to be in the order of 0.1. This value is in agreement with reverberation mapping results.

5.1.2 Super-Eddington Accretion

As indicated in Section 3.5, if the QSO is viewed face-on, the L/L_{Edd} calculation method could over-estimate the L/L_{Edd} by a factor of 3. For the few $L/L_{\text{Edd}} \sim 10$ objects, there are indications that their Hβ profile might contain an unusually large narrow component that is not completely subtracted by 10% of the [O III] flux. The residue narrow Hβ component could cause a 50% under-estimate of the FWHM(Hβ) and hence a factor of 2 over-estimate of the L/L_{Edd}. Considering the above factors, most QSOs in the sample have accretion rates consistent with or below the Eddington limit.

On the other hand, it is possible for QSOs to have accretion rates beyond the Eddington limit. In this section, I will discuss several mechanisms
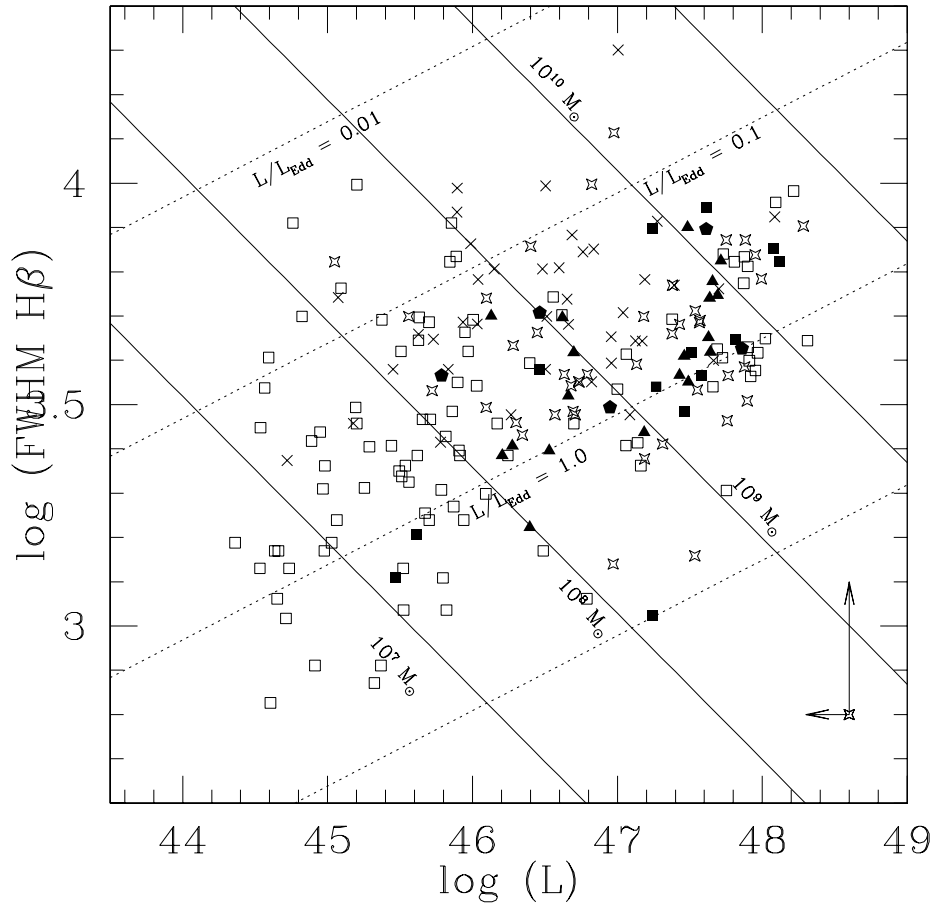
Figure 5.1 The L versus FWHM(Hβ) correlation with constant M_{BH} and L/L_{Edd} contours. The solid lines are constant black hole mass lines. The dashed lines are constant Eddington ratio lines. The arrows at the lower right corner of the plot represent possible corrections for flat spectrum radio loud objects due to the beaming and orientation effects. For the meaning of the symbols, please refer to Figure 4.1.

128

for super-Eddington accretion in QSOs. Past research has suggested that QSOs can be super Eddington accretors (Collin, Boisson, Mouchet, Dumont et al. 2002; Wang 2003). For steady state spherical accretion flows, the Eddington ratio should always be less than 1. In real world QSOs, the accretion flow is probably neither steady state nor spherically symmetric. However, the fact that most QSOs have Eddington ratios close to 1 suggests that the interaction between the radiation force and gravitational force is strong.

If the QSO has a very luminous accretion disk that is geometrically thin and optically thick, the outward radiation peaks in the direction perpendicular to the disk plane while the accretion material comes in close to the disk plane. The radiation force and gravitational force are never balanced. That provides a mechanism for the apparent super-Eddington accretion in some QSO systems. If the accretion flow has a large covering factor, it would see the bright disk surface and the radiation pressure supported thick inner disk around the central black hole, and hence experience the outward radiation pressure. Under this model, larger accretion flow covering factor corresponds to smaller upper limit for the accretion rate.

If the accretion flow is not steady state, QSOs can have super Eddington luminosity over a period of time. Studies of accretion disks around stellar black holes have shown that they undergo quiescent and outburst cycles (low and high states) in both optical and X-ray bands (McGowan, Priedhorsky and Trudolyubov 2004; Nowak 1995). The standard accretion disk model indicates that disks are subject to thermal-viscous instability due to partial hydrogen ionization (Shakura and Sunyaev 1973; Meyer and Meyer-Hofmerster 1981). In the quiescent state, accreting material builds up in the system and the thermal accretion disk is not prominent. The accretion flow of the inner

region close to the black hole is probably advection dominated (Narayan, Mc-Clintock and Yi 1996). In the high state, the viscosity drastically increases and results in a bright thermal accretion disk with large accretion rate. The high state accretion disks typically have Eddington ratio greater than 0.08 (Narayan, McClintock and Yi 1996) and no inner advection zones. In the high state phase, the accretion fuel is already built-up in the disk and the accretion rate is regulated by the pressure inside the optically thick disk rather than the radiation pressure from the black hole. The maximum accretion rate for a high state accretion disk is limited by the dynamics in the inner region of the disk.

Done, Pounds, Nandra and Fabian (1995) have shown that QSO X-ray spectra are very similar to stellar black hole accretors in the high state. Past research also showed that theoretically AGN accretion disks could display ionization instability too (Lin and Shields 1986; Siemiginowska, Czerny and Kostyunin 1996). Most UV-optical selected QSOs are selected to show signatures of strong thermal accretion disks. Disk theories have suggested that such optically thick disks can exist only at relatively high accretion rates. If the accretion rate drops below 8% of the Eddington limit, the disk will become advection dominated, which is primarily suggested for low luminosity AGNs such as LINERs (e.g. Yuan, Markoff, Falcke and Biermann 2002). My results support the hypothesis that QSOs have outburst accretion disks by showing that QSOs black holes accrete at or near the Eddington limit.

Fully developed QSO accretion disks are thought to have a geometrically thick inner region caused by self-radiation and magnetic fields. Theoretical analysis has shown that the maximum accretion rate for a stable thick disk is h/r times the Eddington rate of the central object, where h is the height

the inner disk and r is the inner radius. My results suggest that the h/r value can not be very large due to the fact that the upper limit of QSO accretion rates does not far exceed the Eddington ratio.

5.2 Emission Line Correlations

5.2.1 Eigenvector 1 and Unification

The BGEV1 properties discussed in this study are: The smaller Fe II/Hβ corresponds to larger EW([O III]), larger FWHM(Hβ) and larger EW(Hβ). I successfully extend the EW([O III]) and Fe II/Hβ anti-correlation from low luminosity QSOs (Boroson and Green 1992) to the high luminosity QSOs. Since the QSOs in my sample reach the highest QSO luminosities, this anti-correlation is universal among QSOs and probably reflect physical processes common to all QSOs. I confirmed that radio loud QSOs and BAL QSOs are at the low and high Fe II ends of the anti-correlation.

The large luminosity coverage of my sample weakens the BGEV1 correlation between FWHM(Hβ) and Fe II/Hβ. Since the FWHM(Hβ) is correlated with L, which is a key BGEV2 property, the FWHM(Hβ) versus Fe II/Hβ plot now shows the competing effects of the orthogonal BGEV1 and BGEV2. The luminosity-introduced scatter destroys correlation between Fe II/Hβ and M_{BH} seen in low luminosity samples. On the other hand, Fe II/Hβ is tightly correlated with L/L_{Edd} regardless of the luminosity range. These results strongly support the hypothesis that Eddington ratio, not black hole mass, is the latent variable behind the BGEV1 set of relationships (Boroson 2002).

Similarly, EW([O III]) and EW(Hβ) are also anti-correlated with L/L_{Edd} regardless of the luminosity range. However, since EW([O III]) is strongly anti-correlated with L ([O III] Baldwin Effect), it is also anti-correlated with M_{BH}.

131

Like the FWHM(Hβ), EW([O III]) is connected to both BGEV1 and BGEV2.

The emission strength of [O III] and Fe II depends on the amount of gas containing O^{++} and Fe^+ ions and how they are illuminated by ionizing photons from the central object. The weak [O III] narrow lines, weak Hβ broad lines and strong Fe II broad emission lines suggest large amounts of cool and dense gas clouds in the BLR near the QSO accretion disk. The Fe II line is primarily emitted from high density and low temperature zones in the BLR (~ 6000K) (Wills, Netzer and Wills 1985). The radiation temperature in the region behind the optically thick and low temperature BLR clouds could drop low enough for dust grains to survive. Hence many Fe II strong QSOs (e.g., BAL QSOs in this sample) often show dust reddened continua. The large amount of dusty gas outside of the BLR prevents ionizing photons from the reaching the outer NLR causing the weak [O III] lines in those objects. I hypothesize that those relatively cool and dusty gas clouds are part of the accretion material build-up that leads to the outburst of QSO accretion disks. Once the outburst starts, the cool gas clouds are illuminated and the iron dust particles are sublimed into the BLR gas to emit strong Fe II lines. But the ionizing photons are blocked from the NLR by the thick gas and remaining dusty materials. Below, I will discuss two ways to associate the Eddington ratio with the dusty gas and unify QSOs based on their BGEV1 properties.

- The Eddington ratio can be linked to the availability of accretion fuel. Although we do not know the exact physics of the transition from quiescent disk (low state) to outburst disk (high state), we can speculate that if there is more accretion material build-up, the outburst would have higher accretion rate and produces higher luminosity from the disk. However, the availability of accretion fuels does not linearly correlate with

Eddington ratio. For low L/L_{Edd} objects, which are found mostly in the low redshift sample, increasing the fuel supply increases the accretion rate. At higher luminosities (high redshift), most QSOs would have reached the Eddington ratio limit set forth by the maximum accretion rate allowed by the inner disk structure.

- The Eddington ratio could also be linked to the evolutionary stages of the QSO black hole growth (e.g. Fabian 1999). At the beginning of the high state, the Eddington ratio is high but the QSO appear shrouded with absorption lines, reddened continuum and little radio emission. The Eddington ratio is limited by the availability of the cool, dusty fueling gas as well as the disk dynamics. As the high state progresses, the cold gas clouds are either accreted into the disk or blown away by the outflow. The object becomes a normal optically selected QSO. Then, when the accretion material runs out, the QSO's Eddington ratio decreases to sub-Eddington level.

5.2.2 The Baldwin Effects
5.2.2.1 The Hβ Baldwin Effect

Compared with samples used in previous Hβ Baldwin Effect studies, my sample has the largest luminosity coverage spanning five orders of magnitudes, making it ideal for detecting the weak anti-correlation between EW(Hβ) and L. In addition, I am able to apply the same method to measure all Hβ equivalent widths to avoid systematic differences between different sub-samples. However, I am still unable to detect a significant EW(Hβ) versus L anti-correlation in my combined sample.

The slope of the Hβ Baldwin Effect in my combined sample is $-0.020\pm$

0.015. With the greater luminosity coverage, I were able to reduce the error bar on the Hβ Baldwin Effect slope compared with the results from Espey and Andreadis (1999); Sergeev, Pronik, Sergeeva and Malkov (1999). However, even with such improvements, the Hβ Baldwin Effect slope is still nearly consistent with zero. The large scatter in the EW(Hβ) versus L diagram is probably caused by the fact that EW(Hβ) is a strong BGEV1 component which is orthogonal to the luminosity dominant BGEV2. The slope, if any, is much smaller than the Baldwin Effect slopes from C IV and He II lines (e.g. Kinney, Rivolo and Koratkar 1990). I do not confirm the reverse Baldwin Effect for Hβ observed in Croom et al. (2002). The very shallow slope of the correlation and the large scatter makes the Baldwin Effect very hard to detect in QSO samples with limited luminosity coverage. The EW(Hβ) is not a reliable estimator for QSO bolometric luminosity and cannot be used as a distance standard candle (Baldwin 1977).

The slopes of Baldwin Effects have been suggested to be associated with the emission line's ionization potential (e.g. Korista, Baldwin and Ferland 1998; Espey and Andreadis 1999). Figure 5.2 plots the Baldwin Effect slope of the Hβ line (red symbol) with slopes of other broad lines gathered in Espey and Andreadis (1999). Within uncertainties, the Hβ slope is consistent with the Lyα and Hα slopes, which have the same ionization potential. The dashed line is the fit for the "slope of the slopes" from Espey and Andreadis (1999). The new Hβ slope data point is consistent with the fit as well. The result supports the hypothesis that Baldwin Effects are caused by softer ionizing continuum at higher accretion disk luminosity (Netzer, Laor and Gondhalekar 1992; Korista, Baldwin and Ferland 1998).

Consistent with the results from Baldwin, Wampler and Gaskell (1989),

the Baldwin Effect does not seem to depend on the QSO types. The radio loud, radio quiet and BAL QSOs in my sample display a similar lack of anti-correlation between EW(Hβ) and L.

5.2.2.2 The [O III] Baldwin Effect

In this study, I confirmed the [O III] Baldwin Effect for all classes of QSOs over a wide luminosity range, extending earlier results from Brotherton (1996). The same mechanism for the broad line Baldwin Effects, luminosity-dependent ionizing continuum and ionizing parameters, may contribute to the [O III] Baldwin Effect as well. However, unlike the broad lines, which are dominated by emission clouds selected to have a narrow range of density and distance from the central engine based on the incoming ionizing continuum (Baldwin, Ferland, Korista and Verner 1995; Korista, Baldwin and Ferland 1998), the narrow lines are emitted by gas over a large volume as seen from the [O III] imaging (Pogge 1989). Therefore, the [O III] emission line is affected by the overall amount of O^{++} ions available in the NLR.

If all QSOs have the same amount of NLR O^{++} gas, the Baldwin Effect slope should be close to -1, which is much steeper than the -0.15 to -0.2 slopes derived from my samples. A possible explanation is that more luminous QSOs may also have more NLR gas. That would result in more [O III] flux in high L QSOs and hence slow down EW([O III])'s decrease with increasing luminosity. Higher luminosity corresponds to higher black hole mass, which in turn, corresponds to a more massive bulge (Laor 1998; Gebhardt, Kormendy, Ho, Bender et al. 2000). Since [O III] NLR is linked with the bulge mass, it is reasonable to assume that there is more [O III] NLR gas in systems with higher luminosity (Nelson and Whittle 1996).
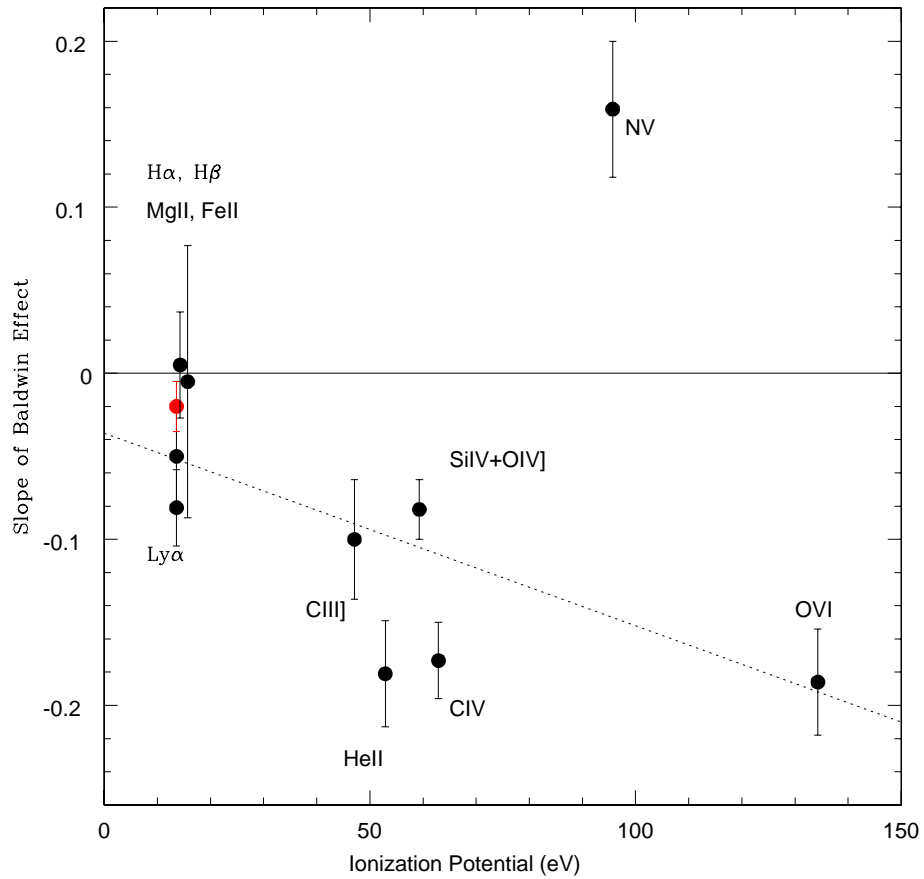
Figure 5.2 Baldwin effect slopes of broad emission lines. The red symbol is the new Hβ data point. The rest data points are adopted from Espey and Andreadis (1999).

5.2.3 Links between BGEV1 and BGEV2

From the correlation results, I have found that some spectral properties make significant contributions to both BGEV1 and BGEV2. As seen in Chapter refresults:, many correlation diagrams are affected by BGEV1 and BGEV2 contributions, with one correlation being dominant and the other contributing to scatter. The most important observational properties that belong to both BGEV1 and BGEV2 are as follows.

- The key BGEV1 component EW([O III]) is shown to be anti-correlated with luminosity, which is a primary BGEV2 component.

- FWHM(Hβ) is a key factor in calculating L/L_{Edd} and hence linked with BGEV1. It is also strong a BGEV2 component due to its tight correlation with L due to the limited range of L/L_{Edd} among QSOs.

- My results show that EW(Hβ), which is possibly a Baldwin Effect and BGEV2 component, is also a strong BGEV1 component. EW(Hβ) is correlated or anti-correlated with EW([O III]), Fe II/Hβ, FWHM(Hβ) as well as with L/L_{Edd}. Similarly, Baskin and Laor (2004) has found that EW(C IV) is connected with BGEV1 and L/L_{Edd}.

Although BGEV1 and BGEV2 are thought to be independently driven by the underlying L/L_{Edd} and L (Boroson 2002), there are intrinsic and observational properties that depend on both L/L_{Edd} and L. For example, M_{BH} could be calculated by both L/L_{Edd} and L. So, if an observation property is primarily determined by M_{BH}, it will show up in both BGEV1 and BGEV2.

5.3 The Nature of BAL QSOs

BAL QSOs have extremely weak [O III] lines, strong Fe II lines and also weak Hβ lines (see Figure 4.10 and Section 4.1.1). This indicates BAL QSOs are not just normal QSOs with special viewing angles. They have physical differences from normal QSOs. However, although BAL QSOs in general have the high Eddington ratios among all QSOs, high luminosity BAL QSOs do not have particularly large Eddington ratios compared with other high luminosity QSOs (see Figures 4.13 and 4.16). In fact, at the highest luminosity, all types of QSOs are essentially saturated at accretion rates close to the Eddington limit (Figure 4.9).

The central engines for BAL and non-BAL QSOs might be the same, but the surrounding gas may be different. For instance, if BAL QSOs have a lot more thick gas clouds around the BLR region compared the non-BAL QSOs, the gas clouds could cause the following observational properties.

- It could provide material for the absorbing outflow and result in BALs.

- it might shield the ionizing radiation and create the low temperature zone for the strong Fe II broad lines.

- Dust could survive in the back of the optically thick cloud that contains the low temperature zone and cause the reddened continuum.

- It might shield the ionizing flux from the outer [O III] NLR and reduce the [O III] line strength.

All the above properties are only indirectly linked with the Eddington ratio. BAL QSOs might be objects with the most abundant accretion fuel

and at the early stages of the disk high state. They do not stand out as high Eddington ratio objects when compared with other high luminosity QSOs because all of them have reached the maximum Eddington ratio. In this scenario, BAL QSOs could evolve into normal QSOs by blowing away the dusty gas.

I did not find significant differences in emission line properties for high ionization and low ionization BAL QSOs. I also did not find any correlation between BAL equivalent width and BGEV1 properties. That suggests the same physical conditions are behind all BAL QSOs. If hiBAL and loBAL QSOs are fundamentally the same type of objects, we could explain their differences in terms of orientation. The loBAL QSOs have low ionization absorption troughs and reddened continuum indicating more cold and dusty clouds along the line of sight.

If the QSO central engine is completely obscured by the BAL gas, we might not see the blue color QSO signature and miss them in UV-optical surveys. Since loBAL QSOs are found more frequently in infrared selection samples (Low, Cutri, Huchra and Kleinmann 1988; Boroson and Meyers 1992), we might be missing many of those deeply buried objects in UV-optical QSO surveys.

The lack of correlation between v_{max} and luminosity among my BAL QSOs does not support Laor and Brandt (2002)'s suggestion of X-ray weak QSO absorbers. However, that is probably because my BAL QSO sample only picks up objects with the largest v_{max} and L. My v_{max} values are within a factor 1.5 from each other. This offers little dynamic range for the correlation. By comparison, the Laor and Brandt (2002) study covers QSO absorbers with 1 order of magnitude difference in v_{max} and 4 orders of magnitude different

139

in luminosity. Given the small range of v_{max}, the $v_{max}/FWHM(H\beta)$ in my sample is highly dependent on FWHM(Hβ). Hence, it is highly correlated with the Eddington ratio. It does not have the same implication as the v_{max}/v_{BLR} versus L/L_{Edd} relationship discovered by Laor and Brandt (2002).

5.4 QSO Black Hole Mass Limits

In section 4.1.5, I observed a small increase of L/L_{Edd} at high L. The correlation between L/L_{Edd} and L does not support past suggestions that L/L_{Edd} and L each drives an independent set of eigenvector relationships (Boroson 2002).

One possible explanation is that high luminosity QSOs might have a different accretion process with intrinsically higher Eddington ratio compared with low luminosity QSOs. If that is the case, the different accretion process does not produce any observable difference in the [O III] and Fe II emission line strengths. In addition, researchers have also noted the apparent similarity in other spectral properties between high and low luminosity QSOs.

The second explanation is that QSOs with extremely high black hole masses, which are needed to produce high luminosity at low Eddington ratio, might be rare and are therefore left out in my sample. Since QSO luminosity is the product of M_{BH} and L/L_{Edd}, the correlation between L and L/L_{Edd} suggests that M_{BH} is not a free ranging parameter. High luminosity QSOs are produced by high black masses and high Eddington ratios. If QSOs with high M_{BH} are very rare, a large proportion of high luminosity QSOs would have to come from medium black hole masses, which are readily available, and hence have high Eddington ratios. This explanation suggests a cut-off in QSO mass function above a certain mass.

The results from Netzer (2003) have indicated that there is a upper limit for QSO black hole masses. Corbett et al. (2003) studied QSO luminosity function and concluded that QSO number density decreases with increasing luminosity according to a steep powerlaw above a turn-off luminosity. Since there is a strong M_{BH}— L, relationship, they further conclude that above a turn-off black hole mass, QSO density decreases according to a powerlaw with increasing black hole mass. The turn-off luminosity and mass evolves with luminosity. At $z \sim 2$, the turn-off black hole mass is around 5×10^8 solar mass. Based on the luminosity function, I can calculate exactly how the lack of high black hole mass QSOs could bias the selection toward more high Eddington ratio objects at high luminosity. The detailed calculation can be found in Appendix C of this work.

5.5 Conclusion

In this research project, I obtained new infrared spectra for a sample of BAL QSOs and re-measured QSO spectra from the literature to study the relationship between QSO emission line properties, luminosity and black hole properties. Based on those relationships, I discussed the implications of black hole properties on QSO unification schemes. My main findings include the following.

- A strong correlation exists between QSO luminosity and broad line FWHM. This correlation indicates that most QSOs, regardless of types or luminosities, have similar Eddington accretion ratios (L/L_{Edd} between 0.1 and 1). This conclusion also supported by the strong M_{BH}—L correlation with powerlaw index close to 1. Super-Eddington accretion is

observed in some objects. There is a slight increase of Eddington ratios at high luminosity. This is probably caused by the sharp decline of the QSO black hole mass function at high mass.

- The [O III] versus optical Fe II anti-correlation (BGEV1) is confirmed to apply to a large sample of diverse QSOs over a wide luminosity range. BAL QSOs are at the weak [O III] and strong Fe II end of the relationship. Radio loud QSOs are at the strong [O III] and weak Fe II end. I confirmed that BGEV1 properties are generally correlated to Eddington ratios with the weaker [O III] and stronger Fe II corresponding to higher L/L_{Edd}. The [O III] and Fe II strengths are probably indirectly linked to L/L_{Edd} through the abundance of accretion fuel.

- Overall, BAL QSOs have higher Eddington ratios when compared with other QSOs. However, when compared with QSOs in the same redshift and luminosity range, BAL QSOs do not show particularly high L/L_{Edd} despite their weaker [O III] and stronger Fe II. I interpret this as BAL QSOs have more abundant accretion fuel but were unable to accrete at a higher L/L_{Edd} due to the limits posed the inner accretion disk structure. BAL QSOs could be young QSOs enshrouded in dusty clouds. The orientation parent population of BAL QSOs can be selected from objects with extreme BGEV1 properties.

- Radio loud QSOs tend to have high black hole mass and low Eddington ratio. Among radio loud QSOs, the radio loudness is not correlated with black hole mass. The radio spectral index is correlated with the calculated luminosity, indicating beaming. That requires us to correct

for luminosity and line FWHM for flat spectrum radio loud objects when calculating M_{BH} and L/L_{Edd}.

- Despite the large luminosity coverage, I did not detect a significant anti-correlation between EW(Hβ) and L to confirm the Hβ Baldwin Effect after excluding the flat spectrum radio loud and BAL QSOs, which could cause biases. Part of the reason for the lack of anti-correlation could be that the EW(Hβ) versus L is too shallow compared with the large scatter in EW(Hβ). The shallow slope is consistent with the ionization potential theory for Baldwin effect. I observed Baldwin Effect for the [O III] line, which is probably caused by the limited amount of [O III] emitting gas in the system.

To further continue the research in this project, I need to analyze emission line properties based on complete QSO samples that reaches to low luminosity at high redshift and includes a large number of BAL QSOs. Such sample might be obtained by argumenting new spectral survey data (e.g., the SDSS) with new infrared observations.

Appendices

Appendix A

The Data and Measurement Tables

In this appendix, I list the measured and calculated properties of QSOs in the sample used in this thesis. The columns in those tables are as follows.

- Columns RA and DEC are the epoch 2000 coordinates of the target QSO.

- Column z is the redshift.

- Column L is the logarithmic value of the QSO bolometric luminosity in the unit of solar luminosity.

- Column M_{BH} is the logarithmic value of the QSO black hole mass in the unit of solar mass.

- Column L/L_{Edd} is the logarithmic value of the Eddington accretion ratio.

- Column R* is the logarithmic value of the radio loudness calculated from the flux density (per Hz) ratio between the rest frame 5GHz and 4400Å.

- Column radio spec index is the radio spectral index measured at rest frame 5GHz.

- Column BAL class is the low ionization and high ionization classification of BAL QSOs.

- Column Hβ or Hα FWHM is the logarithmic value of the Hβ broad line FWHM in the unit of km s^{-1}. If Hβ region spectrum is not available, I used the Hα FWHM instead.

- Column Hβ EW is the logarithmic value of the Hβ broad line equivalent width in the unit of Å.

- Column [O III] EW is the logarithmic value of the [O III] narrow line equivalent width in the unit of Å.

- Column Fe II/Hβ is the logarithmic value of the ratio of the Fe II and Hβ broad line equivalent widths.

- Column Fe II EW is the logarithmic value of the Fe II broad line equivalent width in the unit of Å. It is measured between rest frame 4434Å and 4484Å.

Table A.1.   Properties of BAL QSOs

RA 2000	DEC 2000	z	L	M_{BH}	L/L_{Edd}	R*	Radio spec index	BAL class
00h45m47.3s	+04d10m24s	0.39	46.62	9.09	−0.57	<−0.01	. . .	Lo
00h46m13.5s	+ 01d04m26s	2.14	47.51	9.52	−0.11	0.92	−0.64	Hi
02h28m39.2s	− 10d11m10s	2.26	48.08	10.36	−0.38	<0.31	. . .	Hi
07h24m18.5s	+ 41d59m14s	1.56	47.18	8.94	0.14	1.39	. . .	Lo
08h04m33.1s	+ 64d59m49s	0.15	46.28	8.28	−0.10	<−0.58	. . .	Lo
08h09m01.3s	+ 27d53m42s	1.23	46.46	8.75	−0.39	<0.72	. . .	Hi
08h45m38.7s	+ 34d20m43s	2.13	47.62	10.24	−0.72	<0.72	. . .	Hi
09h13m28.3s	+ 39d44m44s	1.57	47.24	8.15	0.99	0.56	. . .	Hi
09h34m04.0s	+ 31d53m31s	2.42	47.82	9.78	−0.06	0.89	. . .	Hi
09h49m41.1s	+ 29d55m19s	1.22	47.69	9.89	−0.30	<0.09	. . .	Lo
10h04m20.1s	+05d13m01s	0.16	45.62	7.44	0.07	<0.15	. . .	Hi
10h07m26.1s	+ 12d48m56s	0.24	46.46	9.00	−0.64	2.19	−0.85	. . .
10h13m41.9s	+ 08d51m26s	2.26	47.71	10.06	−0.45	<0.68	. . .	Lo
10h44m59.5s	+ 36d56m05s	0.70	46.66	8.76	−0.20	1.18	. . .	Lo
10h54m27.2s	+ 25d36m00s	2.39	47.49	9.37	0.02	<0.96	. . .	Lo
12h33m56s	+ 13d04m09s	2.38	47.66	9.93	−0.38	<0.79	. . .	Lo
12h34m58.2s	+ 13d08m55s	2.36	47.43	9.36	−0.03	<1.01	. . .	Lo
12h49m13.8s	− 05d59m18s	2.24	48.12	10.33	−0.31	<0.26	. . .	Hi
13h11m36.5s	− 05d52m39s	2.22	47.64	9.60	−0.06	<0.74	. . .	Hi
13h12m13.6s	+ 23d19m59s	1.52	47.27	9.20	−0.03	1.87	. . .	Hi
13h24m22.5s	+ 24d52m22s	2.36	47.46	9.48	−0.11	<0.98	. . .	Lo
14h04m38.8s	+ 43d27m07s	0.32	46.20	8.19	−0.09	<0.23	. . .	Hi
14h08m06.2s	+ 30d54m48s	0.84	46.13	8.77	−0.74	1.25	. . .	Lo
14h19m03.8s	−13d10m44s	0.13	45.79	8.27	−0.59	−0.45	0.15	. . .
14h20m13.1s	+ 25d34m04s	2.20	47.58	9.46	0.02	<0.79	. . .	Hi

Table A.1—Continued

RA 2000	DEC 2000	z	L	M_{BH}	L/L_{Edd}	R*	Radio spec index	BAL class
14h45m15s	− 00d23m59s	2.22	47.24	9.90	−0.76	<1.13	. . .	Hi
14h45m45s	+ 01d29m12s	2.44	47.46	9.22	0.14	<1.01	. . .	Hi
15h16m36.8s	+ 00d29m41s	2.25	47.64	9.84	−0.31	<0.75	. . .	Lo
15h54m44.6s	+08d22m22s	0.12	45.46	7.15	0.22	<0.02	. . .	Hi
17h01m24.8s	+ 51d49m20s	0.29	46.53	8.43	0.00	0.45	−1.04	Lo
17h09m19.9s	+ 28d18m35s	2.38	47.86	9.76	0.00	0.20	. . .	. . .
17h11m24.2s	+ 59d31m21s	1.49	46.70	8.98	−0.38	<1.28	. . .	Lo
17h23m41.1s	+ 55d53m41s	2.11	47.63	9.66	−0.13	<0.70	. . .	Lo
17h35m23.0s	+ 55d46m11s	1.59	47.10	. . .	. . .	<0.94	. . .	Hi
21h14m52.6s	+06d07m43s	0.47	46.95	8.90	−0.05	−0.32	−0.86	. . .
22h15m11.9s	− 00d45m50s	1.48	47.48	10.06	−0.68	<0.48	. . .	Lo
22h15m31.6s	− 17d44m08s	2.22	47.61	10.14	−0.63	<0.76	. . .	. . .
22h36m07.6s	+13d43m55s	0.33	46.40	7.99	0.31	<0.05	. . .	Lo
22h57m17.5s	+02d43m18s	2.09	. . .	. . .	. . .	. . .	0	Lo

Table A.2.   Line measurements of BAL QSOs

RA 2000	DEC 2000	Hβ or Hα FWHM	Hβ EW	[O III] EW	Fe II/Hβ	Fe II EW
00h45m47.3s	+04d10m24s	3.70	1.87	<0.18	0.10	1.97
00h46m13.5s	+ 01d04m26s	3.62	1.44	1.05	−0.20	1.24
02h28m39.2s	− 10d11m10s	3.85	1.89	0.85	−0.08	1.81
07h24m18.5s	+ 41d59m14s	3.44	1.40	<0.75	0.24	1.64
08h04m33.1s	+ 64d59m49s	3.41	. . .	<0.26	. . .	2.13
08h09m01.3s	+ 27d53m42s	3.58	. . .	. . .	. . .	. . .
08h45m38.7s	+ 34d20m43s	3.94	1.56	0.75	0.23	1.78
09h13m28.3s	+ 39d44m44s	3.02	1.33	<0.48	0.32	1.66
09h34m04.0s	+ 31d53m31s	3.65	1.59	<0.26	−0.04	1.55
09h49m41.1s	+ 29d55m19s	3.75	1.61	0.59	−0.27	1.34
10h04m20.1s	+05d13m01s	3.21	1.88	0.86	−0.19	1.70
10h07m26.1s	+ 12d48m56s	3.71	1.41	0.82	−0.41	1.00
10h13m41.9s	+ 08d51m26s	3.82	1.71	<0.26	0.06	1.76
10h44m59.5s	+ 36d56m05s	3.52	. . .	. . .	. . .	. . .
10h54m27.2s	+ 25d36m00s	3.55	1.60	<0.43	−0.06	1.55
12h33m56s	+ 13d04m09s	3.78	1.74	<0.79	−0.15	1.59
12h34m58.2s	+ 13d08m55s	3.57	1.53	<0.48	−0.17	1.37
12h49m13.8s	− 05d59m18s	3.82	1.75	<0.34	0.10	1.85
13h11m36.5s	− 05d52m39s	3.62	1.57	<0.11	0.12	1.69
13h12m13.6s	+ 23d19m59s	3.54	. . .	. . .	. . .	. . .
13h24m22.5s	+ 24d52m22s	3.61	. . .	. . .	. . .	. . .
14h04m38.8s	+ 43d27m07s	3.39	1.48	<0.18	0.22	1.70
14h08m06.2s	+ 30d54m48s	3.70	. . .	. . .	. . .	. . .
14h19m03.8s	−13d10m44s	3.57	2.16	1.76	<−1.48	<0.68
14h20m13.1s	+ 25d34m04s	3.57	1.43	<0.68	0.38	1.81
14h45m15s	− 00d23m59s	3.90	1.49	<0.62	0.31	1.80
14h45m45s	+ 01d29m12s	3.49	1.61	<0.57	−0.24	1.37
15h16m36.8s	+ 00d29m41s	3.74	1.75	<0.32	−0.68	1.07
15h54m44.6s	+08d22m22s	3.11	1.63	0.39	−0.02	1.61
17h01m24.8s	+ 51d49m20s	3.40	2.05	<0.34	−0.14	1.91
17h09m19.9s	+ 28d18m35s	3.63	1.61	0.77	0.07	1.68
17h11m24.2s	+ 59d31m21s	3.62	1.77	1.19	−0.30	1.48
17h23m41.1s	+ 55d53m41s	3.65	1.71	0.96	<−0.62	<1.10
17h35m23.0s	+ 55d46m11s	. . .	1.90	0.98	−0.17	1.73
21h14m52.6s	+06d07m43s	3.49	2.01	1.13	−0.13	1.88
22h15m11.9s	− 00d45m50s	3.90	1.59	<−0.15	−0.17	1.42

Table A.2—Continued

RA 2000	DEC 2000	Hβ or Hα FWHM	Hβ EW	[O III] EW	Fe II/Hβ	Fe II EW
22h15m31.6s	− 17d44m08s	3.90	1.71	1.31	−0.45	1.26
22h36m07.6s	+13d43m55s	3.22	1.81	1.08	−0.12	1.69
22h57m17.5s	+02d43m18s	3.42	1.75	0.85	−0.37	1.38

Table A.3.   Properties of Radio Loud QSOs

RA 2000	DEC 2000	z	L	M_{BH}	L/L_{Edd}	R*	Radio spec index
00h05m59.2s	+ 16d09m48s	0.45	46.96	9.10	−0.25	2.22	−0.81
00h10m31.0s	+ 10d58m30s	0.09	45.45	8.08	−0.73	1.23	−0.51
00h27m15.4s	+ 22d41m58s	1.12	47.38	9.73	−0.45	2.67	−0.12
00h47m05.9s	+ 03d19m55s	0.62	47.04	9.38	−0.45	1.75	−0.87
00h59m05.5s	+ 00d06m52s	0.72	46.57	8.61	−0.14	3.63	−0.32
01h18m18.5s	+ 02d58m06s	0.67	46.51	9.02	−0.61	3.29	−0.78
01h26m42.8s	+ 25d59m01s	2.36	47.53	8.61	0.82	3.91	0.43
01h37m41.3s	+ 33d09m35s	0.37	46.50	8.77	−0.37	3.67	−0.92
01h52m27.3s	− 20d01m06s	2.15	47.76	9.58	0.09	2.54	1.23
01h57m34.9s	+ 74d42m43s	2.34	47.95	10.25	−0.40	3.20	−0.29
02h01m57.1s	− 11d32m34s	0.67	46.96	9.22	−0.36	3.19	−0.72
02h28m53.2s	− 03d37m37s	2.06	47.55	9.37	0.08	3.17	−0.28
02h35m07.4s	− 04d02m06s	1.44	47.66	9.58	−0.02	2.89	−0.79
02h40m08.2s	− 23d09m16s	2.24	48.09	10.51	−0.52	3.56	−0.73
03h36m30.1s	+ 32d18m29s	1.27	47.12	9.31	−0.29	3.86	−0.51
03h47m40.2s	+ 01d05m14s	0.03	43.67	5.98	−0.41	1.58	. . .
04h07m48.4s	− 12d11m37s	0.57	47.43	9.59	−0.26	2.57	−0.42
04h17m16.7s	− 05d53m45s	0.78	47.28	9.95	−0.78	2.43	−0.76
04h23m15.8s	− 01d20m33s	0.92	46.71	8.71	−0.10	3.79	0.18
04h24m08.5s	+ 02d04m25s	2.04	47.75	10.18	−0.53	3.07	−0.4
04h27m07.3s	− 13d02m53s	2.17	47.70	9.93	−0.33	3.16	−0.98
04h56m47.2s	+ 04d00m53s	1.35	47.57	9.70	−0.23	2.59	−0.21
05h55m30.8s	+ 39d48m49s	2.37	47.76	9.37	0.29	3.33	0.94
07h13m02.4s	+ 11d46m15s	0.77	47.01	10.55	−1.64	3.10	−1.02
07h39m18.0s	+ 01d37m05s	0.19	45.72	8.16	−0.54	3.27	−0.16

Table A.3—Continued

RA 2000	DEC 2000	z	L	M_{BH}	L/L_{Edd}	R*	Radio spec index
07h41m10.7s	+ 31d12m00s	0.64	46.66	9.08	−0.52	3.43	−0.59
07h45m41.7s	+ 31d42m57s	0.46	46.82	9.82	−1.10	2.82	−0.36
08h39m50.6s	− 12d14m34s	0.20	46.04	8.87	−0.94	2.67	−0.89
08h40m47.5s	+ 13d12m23s	0.68	46.27	8.41	−0.25	3.83	−0.66
08h41m24.3s	+ 70d53m42s	2.17	47.90	9.55	0.24	3.51	−0.5
09h02m16.8s	− 14d15m31s	1.33	47.54	9.72	−0.28	3.47	0.41
09h06m31.9s	+ 16d46m11s	0.41	45.73	8.40	−0.77	3.43	−1.04
09h27m03.0s	+ 39d02m21s	0.70	46.40	9.26	−0.96	4.17	−0.44
09h54m56.8s	+ 09d29m55s	0.30	45.83	8.33	−0.60	2.67	−0.85
09h54m56.8s	+ 17d43m31s	1.48	47.38	9.51	−0.24	3.25	−0.38
09h58m20.9s	+ 32d24m02s	0.53	46.97	8.20	0.67	2.73	−0.48
10h10m27.5s	+ 41d32m39s	0.61	46.82	8.93	−0.21	3.07	−0.62
10h14m47.1s	+ 23d01m18s	0.57	46.34	8.37	−0.13	3.20	−0.5
10h14m55.1s	+00d33m38s	0.19	44.72	7.19	−0.57	1.03	−0.91
10h22m32.8s	− 10d37m44s	0.20	45.89	9.19	−1.40	2.60	−0.6
10h30m59.1s	+ 31d02m56s	0.18	45.56	8.39	−0.93	2.41	−0.48
10h51m29.9s	− 09d18m10s	0.34	46.15	8.99	−0.95	3.08	−0.89
11h04m13.7s	+ 76d58m58s	0.31	46.48	9.21	−0.83	2.69	−0.88
11h39m57.0s	+ 65d47m49s	0.65	47.19	9.63	−0.54	2.87	−0.81
11h48m55.9s	− 04d04m10s	0.34	46.10	8.83	−0.83	2.82	−0.4
11h53m24.4s	+ 49d31m09s	0.33	46.03	8.67	−0.74	3.16	−0.56
11h59m31.8s	+ 29d14m44s	0.73	46.79	8.94	−0.25	3.21	−0.09
12h20m11.9s	+ 02d03m42s	0.24	46.28	8.74	−0.56	2.58	−0.26
12h28m24.9s	+ 31d28m38s	2.22	48.28	10.60	−0.41	2.05	0
12h29m06.7s	+ 02d03m09s	0.16	46.68	8.82	−0.24	3.51	−0.15

Table A.3—Continued

RA 2000	DEC 2000	z	L	M_{BH}	L/L_{Edd}	R*	Radio spec index
12h31m20.6s	+ 07d25m53s	2.39	47.54	9.47	−0.03	1.85	. . .
12h52m26.3s	+ 56d34m20s	0.32	45.63	8.35	−0.83	3.62	−0.86
12h56m14.2s	+ 56d52m25s	0.04	45.18	7.66	−0.58	1.86	−0.6
13h05m33.0s	− 10d33m19s	0.28	46.69	8.71	−0.12	2.35	0
13h07m54.0s	+ 06d42m14s	0.60	46.60	9.30	−0.80	2.92	−0.92
13h12m17.8s	+35d15m21s	0.18	46.09	8.33	−0.34	1.23	0
13h33m35.8s	+ 16d49m04s	2.08	47.99	10.17	−0.27	2.25	0.73
13h43m00.2s	+ 28d44m07s	0.91	46.98	10.16	−1.28	2.63	0.36
13h53m35.9s	+ 26d31m48s	0.31	45.89	9.08	−1.29	2.37	−0.63
13h57m04.4s	+ 19d19m07s	0.72	47.17	9.34	−0.27	2.97	−0.61
13h58m17.6s	+ 57d52m05s	1.37	47.39	9.74	−0.45	2.79	−0.98
14h07m00.4s	+ 28d27m15s	0.08	45.07	8.15	−1.18	3.27	−0.87
14h27m35.5s	+ 26d32m14s	0.37	46.65	9.19	−0.64	1.83	−0.51
14h36m45.8s	+ 63d36m38s	2.07	47.88	10.27	−0.49	2.87	−0.11
14h51m02.6s	− 23d29m32s	2.22	47.88	9.69	0.08	2.78	0.15
14h59m07.6s	+ 71d40m20s	0.90	47.09	8.95	0.03	3.77	−0.62
15h12m50.5s	− 09d06m00s	0.36	46.30	8.40	−0.20	3.45	0.04
15h14m43.0s	+ 36d50m50s	0.37	46.74	8.87	−0.23	2.27	−0.92
15h24m41.6s	+ 15d21m21s	0.63	46.45	8.90	−0.56	3.16	0
15h47m43.5s	+ 20d52m17s	0.26	45.93	8.61	−0.78	1.77	−0.76
16h20m21.9s	+ 17d36m24s	0.56	46.76	9.48	−0.81	3.02	−0.91
16h24m39.1s	+ 23d45m13s	0.93	46.84	9.54	−0.80	3.49	−0.89
16h42m58.8s	+ 39d48m37s	0.59	46.73	8.87	−0.24	3.77	0
16h58m33.4s	+ 05d15m16s	0.88	47.18	9.46	−0.38	3.15	−0.18
17h19m38.2s	+ 48d04m12s	1.08	47.84	9.83	−0.09	1.78	. . .

Table A.3—Continued

RA 2000	DEC 2000	z	L	M_{BH}	L/L_{Edd}	R*	Radio spec index
17h23m20.8s	+ 34d17m58s	0.21	45.78	7.97	−0.29	2.76	−0.67
17h52m46.0s	+ 17d34m20s	0.50	46.63	8.84	−0.30	2.78	0
21h37m45.2s	− 14d32m55s	0.20	45.99	9.00	−1.11	2.99	−0.86
21h48m05.5s	+ 06d57m39s	1.00	47.31	8.97	0.24	3.47	0.31
22h11m53.6s	+18d41m51s	0.07	45.05	8.30	−1.35	1.89	0
22h18m52.0s	− 03d35m37s	0.90	47.19	8.82	0.27	3.01	0.38
22h54m10.4s	+ 11d36m38s	0.33	46.50	9.60	−1.20	2.60	−0.76
23h11m17.7s	+ 10d08m15s	0.43	46.69	9.50	−0.92	2.28	−0.82
23h12m58.8s	+ 38d47m43s	2.17	47.57	9.69	−0.22	3.07	−0.35
23h46m36.8s	+ 09d30m46s	0.68	47.13	9.21	−0.18	2.93	−0.21

Table A.4.   Line measurements of Radio Loud QSOs

RA 2000	DEC 2000	Hβ or Hα FWHM	Hβ EW	[O III] EW	Fe II/Hβ	Fe II EW
00h05m59.2s	+ 16d09m48s	3.59	1.95	1.42	<-1.00	<0.95
00h10m31.0s	+ 10d58m30s	3.58	2.04	1.62	-0.56	1.48
00h27m15.4s	+ 22d41m58s	3.77	1.70	1.12	<-0.94	<0.76
00h47m05.9s	+ 03d19m55s	3.71	1.74	1.32	-0.42	1.32
00h59m05.5s	+ 00d06m52s	3.48	1.45	1.70	<-0.45	<1.00
01h18m18.5s	+ 02d58m06s	3.70	1.92	1.67	<-0.92	<1.00
01h26m42.8s	+ 25d59m01s	3.16	1.53	1.32	-0.40	1.13
01h37m41.3s	+ 33d09m35s	3.58	1.65	1.65	0.17	1.83
01h52m27.3s	$-$ 20d01m06s	3.57	1.61	1.27	<-0.61	<1.00
01h57m34.9s	+ 74d42m43s	3.84	1.81	1.29	-0.53	1.28
02h01m57.1s	$-$ 11d32m34s	3.65	1.81	1.28	0.10	1.90
02h28m53.2s	$-$ 03d37m37s	3.53	1.40	1.38	<-0.61	<0.79
02h35m07.4s	$-$ 04d02m06s	3.60	1.71	1.13	-0.28	1.43
02h40m08.2s	$-$ 23d09m16s	3.92	1.97	<0.40	-0.13	1.83
03h36m30.1s	+ 32d18m29s	3.64	1.65	0.26	-0.16	1.49
03h47m40.2s	+ 01d05m14s	3.12	1.96	1.32	-0.02	1.94
04h07m48.4s	$-$ 12d11m37s	3.68	1.76	1.08	-0.45	1.30
04h17m16.7s	$-$ 05d53m45s	3.91	2.32	1.40	<-1.32	<1.00
04h23m15.8s	$-$ 01d20m33s	3.48	1.63	. . .	. . .	. . .
04h24m08.5s	+ 02d04m25s	3.87	1.95	1.70	-0.75	1.20
04h27m07.3s	$-$ 13d02m53s	3.76	1.82	1.48	-0.58	1.24
04h56m47.2s	+ 04d00m53s	3.69	1.90	0.94	-1.06	0.85
05h55m30.8s	+ 39d48m49s	3.46	1.41	1.17	<-0.92	<0.49
07h13m02.4s	+ 11d46m15s	4.30	1.95	1.34	<-0.95	<1.00
07h39m18.0s	+ 01d37m05s	3.53	1.71	0.70	-0.33	1.38
07h41m10.7s	+ 31d12m00s	3.68	2.03	1.23	-0.36	1.67
07h45m41.7s	+ 31d42m57s	4.00	1.98	1.61	<-0.98	<1.00
08h39m50.6s	$-$ 12d14m34s	3.78	2.26	1.73	-0.70	1.56
08h40m47.5s	+ 13d12m23s	3.48	1.66	1.32	<-0.66	<1.00
08h41m24.3s	+ 70d53m42s	3.51	1.38	0.68	0.11	1.49
09h02m16.8s	$-$ 14d15m31s	3.71	1.91	1.22	-0.64	1.28
09h06m31.9s	+ 16d46m11s	3.65	1.53	1.72	<-0.53	<1.00
09h27m03.0s	+ 39d02m21s	3.86	1.81	1.11	<-0.81	<1.00
09h54m56.8s	+ 09d29m55s	3.58	1.90	2.08	<-0.90	<1.00
09h54m56.8s	+ 17d43m31s	3.66	1.53	0.72	0.04	1.57
09h58m20.9s	+ 32d24m02s	3.14	1.08	1.68	0.15	1.23

155

Table A.4—Continued

RA 2000	DEC 2000	Hβ or Hα FWHM	Hβ EW	[O III] EW	Fe II/Hβ	Fe II EW
10h10m27.5s	+ 41d32m39s	3.55	1.63	1.32	<−0.63	<1.00
10h14m47.1s	+ 23d01m18s	3.43	1.72	1.57	−0.37	1.34
10h14m55.1s	+00d33m38s	3.37	1.83	1.49	−0.36	1.46
10h22m32.8s	− 10d37m44s	3.99	2.11	1.59	−0.44	1.67
10h30m59.1s	+ 31d02m56s	3.70	1.83	1.58	<−0.83	<1.00
10h51m29.9s	− 09d18m10s	3.81	1.93	1.51	−1.17	0.76
11h04m13.7s	+ 76d58m58s	3.81	1.92	1.69	−0.53	1.39
11h39m57.0s	+ 65d47m49s	3.78	1.86	1.23	<−0.86	<1.00
11h48m55.9s	− 04d04m10s	3.74	2.05	2.50	<−1.05	<1.00
11h53m24.4s	+ 49d31m09s	3.68	1.72	1.32	−0.44	1.28
11h59m31.8s	+ 29d14m44s	3.57	1.00	. . .	. . .	. . .
12h20m11.9s	+ 02d03m42s	3.63	2.00	1.59	<−1.00	<1.00
12h28m24.9s	+ 31d28m38s	3.90	1.48	<−0.05	0.14	1.62
12h29m06.7s	+ 02d03m09s	3.54	1.93	0.99	−0.18	1.74
12h31m20.6s	+ 07d25m53s	3.59	1.59	0.92	<−0.50	<1.10
12h52m26.3s	+ 56d34m20s	3.66	2.00	2.18	<−1.00	<1.00
12h56m14.2s	+ 56d52m25s	3.46	1.86	<0.26	0.20	2.06
13h05m33.0s	− 10d33m19s	3.48	1.42	0.99	−0.19	1.23
13h07m54.0s	+ 06d42m14s	3.81	1.78	1.52	<−0.78	<1.00
13h12m17.8s	+35d15m21s	3.49	1.67	1.38	−0.34	1.33
13h33m35.8s	+ 16d49m04s	3.78	1.53	1.27	−0.37	1.15
13h43m00.2s	+ 28d44m07s	4.11	2.23	1.56	−0.87	1.36
13h53m35.9s	+ 26d31m48s	3.93	2.11	1.68	<−1.11	<1.00
13h57m04.4s	+ 19d19m07s	3.64	1.88	1.86	<−0.88	<1.00
13h58m17.6s	+ 57d52m05s	3.77	1.56	1.23	<−0.56	<1.00
14h07m00.4s	+ 28d27m15s	3.74	2.02	1.20	−0.22	1.81
14h27m35.5s	+ 26d32m14s	3.74	2.00	1.54	−0.51	1.49
14h36m45.8s	+ 63d36m38s	3.87	1.76	1.06	−0.57	1.19
14h51m02.6s	− 23d29m32s	3.59	1.82	1.35	−0.52	1.30
14h59m07.6s	+ 71d40m20s	3.48	1.79	1.93	<−0.79	<1.00
15h12m50.5s	− 09d06m00s	3.46	1.75	0.90	0.18	1.92
15h14m43.0s	+ 36d50m50s	3.55	2.03	1.79	<−1.29	<0.74
15h24m41.6s	+ 15d21m21s	3.66	1.48	1.43	<−0.48	<1.00
15h47m43.5s	+ 20d52m17s	3.69	1.83	1.52	<−1.09	<0.74
16h20m21.9s	+ 17d36m24s	3.85	1.65	1.57	. . .	. . .
16h24m39.1s	+ 23d45m13s	3.85	2.02	1.62	<−1.02	<1.00

156

Table A.4—Continued

RA 2000	DEC 2000	Hβ or Hα FWHM	Hβ EW	[O III] EW	Fe II/Hβ	Fe II EW
16h42m58.8s	+ 39d48m37s	3.55	1.00	0.30	<−0.40	<0.60
16h58m33.4s	+ 05d15m16s	3.70	1.71	. . .	0.23	1.94
17h19m38.2s	+ 48d04m12s	3.66	1.75	0.46	−0.41	1.34
17h23m20.8s	+ 34d17m58s	3.41	1.98	1.63	<−0.98	<1.00
17h52m46.0s	+ 17d34m20s	3.57	1.81	1.28	<−0.81	<1.00
21h37m45.2s	− 14d32m55s	3.86	1.83	1.79	<−0.83	<1.00
21h48m05.5s	+ 06d57m39s	3.41	1.52	1.56	−0.21	1.30
22h11m53.6s	+18d41m51s	3.82	1.88	1.20	−0.57	1.31
22h18m52.0s	− 03d35m37s	3.38	1.71	1.48	<−0.92	<0.79
22h54m10.4s	+ 11d36m38s	3.99	2.02	1.37	−0.57	1.45
23h11m17.7s	+ 10d08m15s	3.88	1.96	1.33	<−1.08	<0.88
23h12m58.8s	+ 38d47m43s	3.69	1.81	1.45	0.10	1.91
23h46m36.8s	+ 09d30m46s	3.59	1.93	1.79	<−0.93	<1.00

Table A.5.   Properties of Radio Quiet QSOs

RA 2000	DEC 2000	z	L	M_{BH}	L/L_{Edd}	R*	Radio spec index
00h06m19.5s	+ 20d12m10s	0.03	44.98	6.95	−0.07	−0.51	. . .
00h29m13.6s	+13d16m03s	0.14	45.87	7.74	0.03	0.12	. . .
00h51m35.2s	− 01d07m09s	1.57	47.06	9.21	−0.25	<0.97	. . .
00h51m54.8s	+17d25m58s	0.06	44.91	6.39	0.43	<0.01	. . .
00h52m02.4s	+ 01d01m29s	2.27	47.69	9.65	−0.06	<0.71	. . .
00h52m33.7s	+ 01d40m41s	2.29	47.75	9.05	0.60	<0.65	. . .
00h53m34.9s	+ 12d41m36s	0.06	45.52	7.04	0.38	−0.43	−0.75
00h54m52.1s	+25d25m38s	0.16	45.95	8.58	−0.73	<−0.22	. . .
01h20m17.2s	+ 21d33m46s	1.49	47.90	10.16	−0.36	<0.08	. . .
01h59m50.2s	+00d23m41s	0.16	45.91	8.01	−0.21	0.64	−1.03
02h34m37.8s	− 08d47m15s	0.04	45.09	8.21	−1.22	−0.35	−1.16
02h57m40.8s	− 16d30m46s	0.07	44.97	7.22	−0.35	<0.01	. . .
02h59m05.6s	+ 00d11m22s	3.38	48.02	9.92	0.01	<0.76	. . .
03h04m49.9s	− 00d08m13s	3.29	47.95	9.73	0.13	<0.80	. . .
04h14m52.6s	− 07d55m39s	0.04	44.59	7.57	−1.07	<−0.13	. . .
04h36m22.2s	− 10d22m34s	0.04	44.98	7.33	−0.45	0.11	. . .
07h47m29.1s	+ 60d56m01s	0.03	45.29	7.62	−0.44	−0.83	. . .
07h52m22.5s	+ 60d57m52s	2.49	47.90	9.80	0.00	<0.59	. . .
08h10m58.6s	+76d02m42s	0.10	45.65	7.99	−0.43	−0.47	−0.57
08h44m45.2s	+76d53m09s	0.13	45.44	7.73	−0.39	<0.13	. . .
08h47m42.4s	+34d45m04s	0.06	45.49	7.65	−0.26	<−0.57	. . .
08h59m24.3s	+ 46d37m17s	0.92	47.06	8.80	0.16	<0.43	. . .
09h23m32.3s	+ 57d45m57s	1.38	47.38	9.58	−0.30	<0.52	. . .
09h25m12.9s	+52d17m11s	0.04	44.36	6.58	−0.32	<0.01	. . .
09h25m54.7s	+19d54m05s	0.19	45.89	8.88	−1.09	<0.04	. . .

Table A.5—Continued

RA 2000	DEC 2000	z	L	M_{BH}	L/L_{Edd}	R*	Radio spec index
09h26m03.3s	+12d44m04s	0.03	44.66	6.74	−0.18	0.54	. . .
09h37m01.0s	+01d05m43s	0.05	44.65	6.52	0.03	<0.05	. . .
09h37m48.8s	+ 73d01m58s	2.53	47.97	9.82	0.05	<0.54	. . .
09h48m42.6s	+ 50d29m31s	0.06	44.71	6.47	0.14	0.37	. . .
09h50m48.4s	+39d26m51s	0.21	45.70	8.46	−0.86	<0.30	. . .
09h56m52.4s	+41d15m22s	0.23	46.70	8.66	−0.06	<−0.58	. . .
10h14m20.7s	−04d18m40s	0.06	45.03	7.02	−0.09	<−0.20	. . .
10h25m31.3s	+51d40m35s	0.05	44.63	6.72	−0.19	<−0.03	. . .
10h51m43.8s	+33d59m26s	0.17	45.86	8.16	−0.40	<−0.06	. . .
10h51m51.4s	−00d51m18s	0.36	46.62	9.10	−0.58	<−0.08	. . .
11h06m31.8s	+ 00d52m52s	0.42	45.20	8.75	−1.65	<1.50	. . .
11h06m33.4s	− 18d21m23s	2.31	47.91	9.74	0.07	<0.50	. . .
11h06m47.5s	+ 72d34m07s	0.01	44.57	7.41	−0.95	<−1.40	. . .
11h17m06.4s	+44d13m33s	0.14	45.63	8.33	−0.80	<0.04	. . .
11h18m30.2s	+40d25m53s	0.15	45.70	7.56	0.04	−0.49	. . .
11h19m08.6s	+21d19m18s	0.18	46.17	8.31	−0.24	−0.14	−0.81
11h21m47.1s	+11d44m18s	0.05	45.06	7.14	−0.18	<−0.37	. . .
11h23m20.7s	+ 01d37m48s	1.47	47.88	10.19	−0.41	<0.09	. . .
11h24m39.2s	+42d01m44s	0.23	46.09	7.94	0.05	<0.03	. . .
11h29m16.6s	−04d24m08s	0.06	45.25	7.42	−0.26	<−0.39	. . .
11h52m03.5s	−11d22m24s	0.05	44.89	7.39	−0.60	<−0.21	. . .
11h53m49.2s	+11d28m29s	0.18	46.03	8.39	−0.46	<−0.18	. . .
12h04m42.1s	+27d54m11s	0.17	45.97	8.50	−0.63	<−0.18	. . .
12h08m58.0s	+ 45d40m36s	1.17	47.73	10.10	−0.47	<0.00	. . .
12h14m17.7s	+14d03m13s	0.08	45.67	7.58	0.00	<−0.54	. . .

Table A.5—Continued

RA 2000	DEC 2000	z	L	M_{BH}	L/L_{Edd}	R*	Radio spec index
12h19m20.9s	+06d38m38s	0.33	46.56	9.14	−0.68	0.74	0.14
12h25m27.4s	+ 22d35m13s	2.05	48.09	10.58	−0.59	0.54	−0.31
12h32m03.6s	+20d09m29s	0.06	45.19	7.74	−0.64	<−0.29	. . .
12h46m35.3s	+02d22m09s	0.05	44.61	6.02	0.49	<0.06	. . .
12h50m05.7s	+ 26d31m08s	2.04	48.31	10.10	0.11	−0.29	0.19
13h01m12.9s	+59d02m06s	0.48	47.00	9.01	−0.11	<−0.17	. . .
13h09m47.0s	+08d19m49s	0.16	46.00	8.67	−0.77	<−0.27	. . .
13h13m05.8s	−11d07m42s	0.03	44.53	6.58	−0.14	<−0.18	. . .
13h23m20.6s	+ 29d10m07s	0.97	47.14	8.86	0.18	<0.41	. . .
13h23m49.5s	+65d41m48s	0.17	45.82	8.02	−0.30	<−0.01	. . .
13h37m18.7s	+ 24d23m03s	0.11	45.79	7.76	−0.07	0.37	. . .
13h41m00.7s	+ 41d23m14s	1.22	47.66	9.46	0.10	<0.12	. . .
13h43m56.7s	+25d38m48s	0.09	44.95	7.47	−0.62	<0.25	. . .
13h48m44.1s	− 03d53m25s	2.34	47.92	9.68	0.14	<0.51	. . .
13h53m03.4s	+ 69d18m30s	0.03	44.82	7.90	−1.18	<−0.57	. . .
13h53m15.8s	+ 63d45m45s	0.09	45.82	7.24	0.48	0.11	−1.04
13h54m06.4s	+23d25m49s	0.06	44.98	5.69	1.19	<−0.19	. . .
13h54m35.6s	+18d05m17s	0.15	45.90	8.32	−0.52	<−0.18	. . .
13h56m32.7s	+21d03m52s	0.30	46.39	8.73	−0.44	<−0.03	. . .
14h05m16.2s	+25d55m35s	0.16	45.94	7.72	0.12	<−0.15	. . .
14h06m21.8s	+22d23m46s	0.10	45.37	6.69	0.58	−0.28	−0.98
14h13m48.3s	+44d00m14s	0.09	45.62	7.80	−0.28	<−0.39	. . .
14h17m00.8s	+44d56m06s	0.11	45.54	7.70	−0.27	<−0.09	. . .
14h18m51.1s	+ 08d52m27s	2.00	47.72	9.63	−0.01	<0.55	. . .
14h29m06.6s	+01d17m06s	0.09	45.84	8.83	−1.08	−0.86	0.08

Table A.5—Continued

RA 2000	DEC 2000	z	L	M_{BH}	L/L_{Edd}	R*	Radio spec index
14h29m43.0s	+47d47m26s	0.22	45.91	8.00	−0.18	<0.15	. . .
14h38m16.1s	−06d58m21s	0.13	45.71	8.02	−0.42	<−0.17	. . .
14h42m07.4s	+35d26m23s	0.08	45.52	7.23	0.19	−0.62	−1.07
14h46m45.9s	+40d35m05s	0.27	46.24	8.21	−0.07	<0.01	. . .
14h51m08.8s	+27d09m27s	0.07	45.32	6.58	0.64	−0.39	−0.82
15h04m01.2s	+10d26m16s	0.04	45.20	7.67	−0.57	<−0.80	. . .
15h21m14.2s	+22d27m43s	0.14	45.56	7.64	−0.18	<0.05	. . .
15h24m24.6s	+ 09d58m30s	1.33	47.87	10.07	−0.30	<−0.01	. . .
15h35m52.3s	+57d54m09s	0.03	44.54	7.21	−0.78	<−0.30	. . .
15h36m38.3s	+54d33m33s	0.04	44.74	6.71	−0.07	<−0.26	. . .
15h45m30.2s	+48d46m09s	0.40	46.49	7.95	0.44	0.05	−0.78
16h13m57.2s	+65d43m10s	0.13	45.85	9.01	−1.25	−0.08	−0.45
16h14m13.2s	+26d04m16s	0.13	45.80	7.37	0.33	0.42	−1.14
16h20m11.3s	+17d24m28s	0.11	45.63	8.44	−0.90	<−0.20	. . .
16h27m56.0s	+55d22m31s	0.13	45.51	8.20	−0.79	<0.08	. . .
16h34m28.9s	+ 70d31m33s	1.34	48.22	10.71	−0.60	−0.64	0
17h04m41.4s	+ 60d44m31s	0.37	46.79	7.93	0.76	0.64	−0.75
21h32m27.8s	+10d08m19s	0.06	45.51	7.64	−0.23	−0.41	−0.53
21h36m23.8s	+ 15d45m08s	2.13	47.81	10.12	−0.41	<0.53	. . .
22h17m12.2s	+14d14m21s	0.07	45.38	8.25	−0.98	<−0.43	. . .
23h07m02.9s	+04d32m57s	0.04	44.76	8.29	−1.63	<−0.22	. . .
23h22m24.8s	− 00d07m19s	1.54	47.16	8.77	0.29	<0.85	. . .

Table A.6.   Line measurements of Radio Quiet QSOs

RA 2000	DEC 2000	Hβ or Hα FWHM	Hβ EW	[O III] EW	Fe II/Hβ	Fe II EW
00h06m19.5s	+ 20d12m10s	3.17	1.91	1.30	−0.32	1.58
00h29m13.6s	+13d16m03s	3.27	1.80	1.45	−0.88	0.92
00h51m35.2s	− 01d07m09s	3.61	1.51	0.18	0.09	1.60
00h51m54.8s	+17d25m58s	2.91	2.18	1.99	<−1.76	<0.43
00h52m02.4s	+ 01d01m29s	3.63	1.66	0.81	0.14	1.80
00h52m33.7s	+ 01d40m41s	3.31	1.54	0.76	−0.12	1.43
00h53m34.9s	+ 12d41m36s	3.04	1.60	1.28	0.09	1.69
00h54m52.1s	+25d25m38s	3.66	1.95	1.55	−0.65	1.30
01h20m17.2s	+ 21d33m46s	3.81	1.59	0.26	−0.50	1.09
01h59m50.2s	+00d23m41s	3.40	1.92	1.83	−0.13	1.80
02h34m37.8s	− 08d47m15s	3.76	1.97	1.95	−0.25	1.72
02h57m40.8s	− 16d30m46s	3.31	1.85	1.85	−0.11	1.74
02h59m05.6s	+ 00d11m22s	3.65	. . .	. . .	. . .	. . .
03h04m49.9s	− 00d08m13s	3.58	. . .	. . .	. . .	. . .
04h14m52.6s	− 07d55m39s	3.61	1.98	2.35	−0.44	1.54
04h36m22.2s	− 10d22m34s	3.36	1.95	1.64	−0.30	1.65
07h47m29.1s	+ 60d56m01s	3.40	1.90	1.72	−0.73	1.18
07h52m22.5s	+ 60d57m52s	3.63	1.80	1.32	−0.55	1.26
08h10m58.6s	+76d02m42s	3.47	2.04	1.23	−0.23	1.81
08h44m45.2s	+76d53m09s	3.41	1.86	1.09	−0.14	1.72
08h47m42.4s	+34d45m04s	3.35	1.80	0.88	−0.16	1.64
08h59m24.3s	+ 46d37m17s	3.41	2.00	1.07	−1.15	0.86
09h23m32.3s	+ 57d45m57s	3.69	1.66	1.07	<−0.66	<1.00
09h25m12.9s	+52d17m11s	3.19	2.10	1.88	<−1.88	<0.23
09h25m54.7s	+19d54m05s	3.83	1.94	1.03	−0.09	1.85
09h26m03.3s	+12d44m04s	3.17	1.80	1.42	−0.64	1.16
09h37m01.0s	+01d05m43s	3.06	1.90	1.68	−0.57	1.32
09h37m48.8s	+ 73d01m58s	3.62	2.13	1.44	0.02	2.15
09h48m42.6s	+ 50d29m31s	3.02	1.79	1.56	−0.04	1.74
09h50m48.4s	+39d26m51s	3.69	2.02	1.26	−0.63	1.39
09h56m52.4s	+41d15m22s	3.46	2.00	1.33	−0.89	1.11
10h14m20.7s	−04d18m40s	3.19	1.62	1.19	−0.50	1.12
10h25m31.3s	+51d40m35s	3.17	1.68	0.79	−0.11	1.58
10h51m43.8s	+33d59m26s	3.48	1.92	1.43	−0.87	1.05
10h51m51.4s	−00d51m18s	3.70	2.09	1.75	−0.19	1.89
11h06m31.8s	+ 00d52m52s	4.00	1.91	1.25	−0.27	1.63

162

RA 2000	DEC 2000	Hβ or Hα FWHM	Hβ EW	[O III] EW	Fe II/Hβ	Fe II EW
11h06m33.4s	− 18d21m23s	3.60	1.69	1.11	−0.24	1.45
11h06m47.5s	+ 72d34m07s	3.54	1.57	1.20	0.08	1.64
11h17m06.4s	+44d13m33s	3.65	1.95	1.31	−0.95	1.00
11h18m30.2s	+40d25m53s	3.24	1.80	0.92	−0.30	1.50
11h19m08.6s	+21d19m18s	3.46	2.05	1.30	−0.44	1.61
11h21m47.1s	+11d44m18s	3.24	1.67	1.27	−0.23	1.44
11h23m20.7s	+ 01d37m48s	3.83	1.70	1.12	−0.50	1.20
11h24m39.2s	+42d01m44s	3.30	1.90	0.73	−0.92	0.97
11h29m16.6s	−04d24m08s	3.31	1.94	1.21	−0.06	1.87
11h52m03.5s	−11d22m24s	3.42	2.02	1.53	−0.76	1.26
11h53m49.2s	+11d28m29s	3.54	1.81	1.09	<−0.92	<0.89
12h04m42.1s	+27d54m11s	3.62	1.96	1.59	−0.69	1.27
12h08m58.0s	+ 45d40m36s	3.84	1.96	0.95	0.13	2.09
12h14m17.7s	+14d03m13s	3.25	1.88	1.10	−0.43	1.45
12h19m20.9s	+06d38m38s	3.74	1.93	1.01	−0.78	1.15
12h25m27.4s	+ 22d35m13s	3.96	1.85	0.95	−0.37	1.49
12h32m03.6s	+20d09m29s	3.49	1.85	1.22	−0.36	1.49
12h46m35.3s	+02d22m09s	2.83	1.45	1.20	−0.05	1.40
12h50m05.7s	+ 26d31m08s	3.64	1.68	1.04	−0.34	1.33
13h01m12.9s	+59d02m06s	3.53	1.70	<0.32	0.20	1.89
13h09m47.0s	+08d19m49s	3.69	2.02	1.53	−0.83	1.20
13h13m05.8s	−11d07m42s	3.13	1.94	1.86	−0.70	1.24
13h23m20.6s	+ 29d10m07s	3.41	1.74	<0.38	0.33	2.07
13h23m49.5s	+65d41m48s	3.43	1.85	0.93	−0.31	1.54
13h37m18.7s	+ 24d23m03s	3.31	...	...	...	2.03
13h41m00.7s	+ 41d23m14s	3.54	1.59	0.54	0.13	1.72
13h43m56.7s	+25d38m48s	3.44	1.89	1.14	−0.74	1.14
13h48m44.1s	− 03d53m25s	3.56	1.67	0.63	−0.13	1.54
13h53m03.4s	+ 69d18m30s	3.70	1.95	1.18	−0.43	1.52
13h53m15.8s	+ 63d45m45s	3.04	1.89	1.53	<−.134	<0.55
13h54m06.4s	+23d25m49s	2.54	1.19	1.02	<−0.22	<0.97
13h54m35.6s	+18d05m17s	3.55	2.01	1.18	−0.35	1.66
13h56m32.7s	+21d03m52s	3.59	1.80	1.51	−0.49	1.32
14h05m16.2s	+25d55m35s	3.24	1.90	0.76	0.04	1.94
14h06m21.8s	+22d23m46s	2.91	1.76	0.81	−0.03	1.74
14h13m48.3s	+44d00m14s	3.39	1.92	1.19	−0.44	1.48

Table A.6—Continued

RA 2000	DEC 2000	Hβ or Hα FWHM	Hβ EW	[O III] EW	Fe II/Hβ	Fe II EW
14h17m00.8s	+44d56m06s	3.36	1.73	<0.26	0.04	1.77
14h18m51.1s	+ 08d52m27s	3.61	1.61	0.91	−0.31	1.31
14h29m06.6s	+01d17m06s	3.82	1.89	1.15	−0.58	1.32
14h29m43.0s	+47d47m26s	3.39	2.03	1.73	−0.57	1.46
14h38m16.1s	−06d58m21s	3.47	2.01	1.19	−0.56	1.44
14h42m07.4s	+35d26m23s	3.13	1.77	0.89	−0.01	1.76
14h46m45.9s	+40d35m05s	3.39	1.84	0.32	0.14	1.98
14h51m08.8s	+27d09m27s	2.87	1.55	1.33	−0.14	1.41
15h04m01.2s	+10d26m16s	3.46	2.06	1.76	−0.83	1.23
15h21m14.2s	+22d27m43s	3.33	2.00	0.74	0.00	2.00
15h24m24.6s	+ 09d58m30s	3.77	2.10	0.67	−0.60	1.51
15h35m52.3s	+57d54m09s	3.45	1.93	1.86	<−0.99	<0.94
15h36m38.3s	+54d33m33s	3.13	1.97	1.20	−0.46	1.52
15h45m30.2s	+48d46m09s	3.17	1.80	0.64	−0.04	1.76
16h13m57.2s	+65d43m10s	3.91	1.98	1.37	−0.46	1.52
16h14m13.2s	+26d04m16s	3.11	2.06	2.14	−1.06	1.00
16h20m11.3s	+17d24m28s	3.70	2.01	1.17	−0.24	1.77
16h27m56.0s	+55d22m31s	3.62	1.95	1.05	−0.73	1.22
16h34m28.9s	+ 70d31m33s	3.98	2.26	1.26	−0.51	1.76
17h04m41.4s	+ 60d44m31s	3.06	1.68	1.45	−0.40	1.28
21h32m27.8s	+10d08m19s	3.34	1.96	1.32	−0.27	1.69
21h36m23.8s	+ 15d45m08s	3.82	1.77	0.71	−0.47	1.31
22h17m12.2s	+14d14m21s	3.69	1.92	1.07	−0.50	1.43
23h07m02.9s	+04d32m57s	3.91	1.85	1.36	−0.85	1.00
23h22m24.8s	− 00d07m19s	3.36	1.68	<0.19	<−0.69	<0.99

Appendix B

Observed Spectra and Model Fits

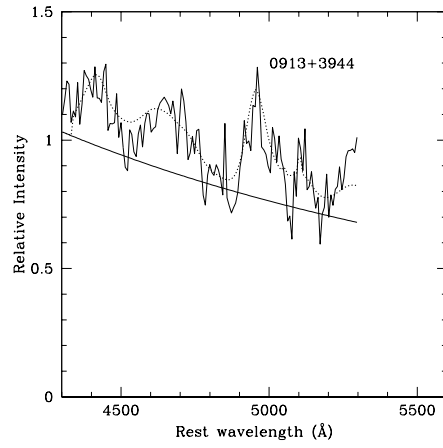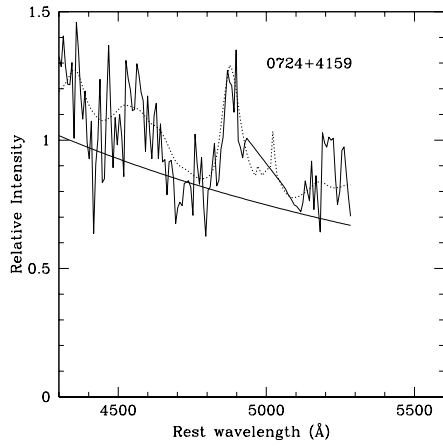In this appendix, I plot the newly observed Hβ region spectra for QSOs used in this thesis. The model fit is overlaid on the calibrate spectrum.
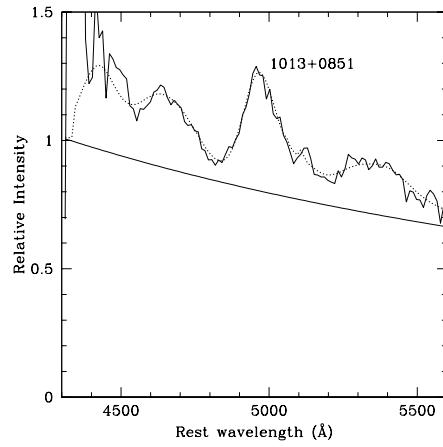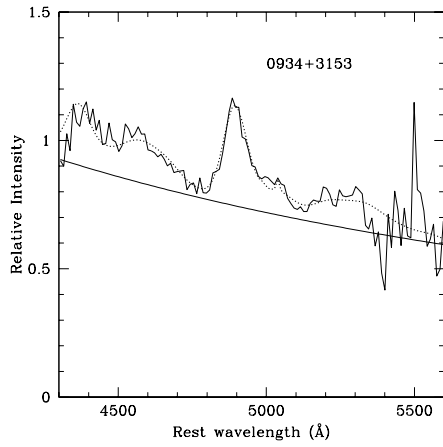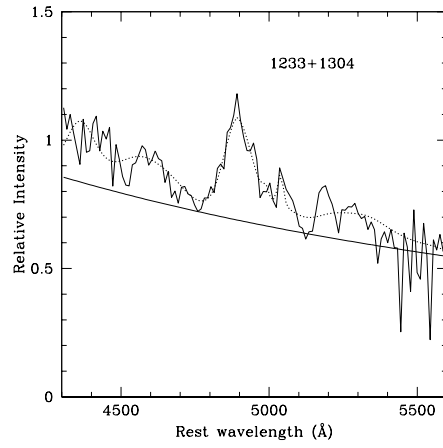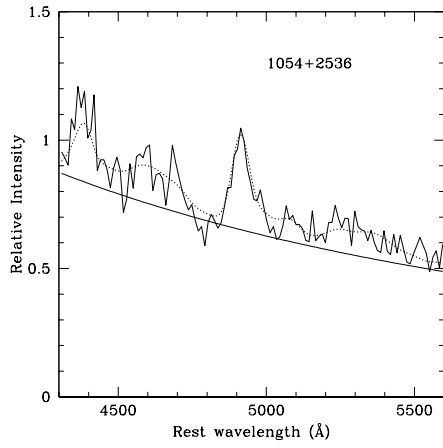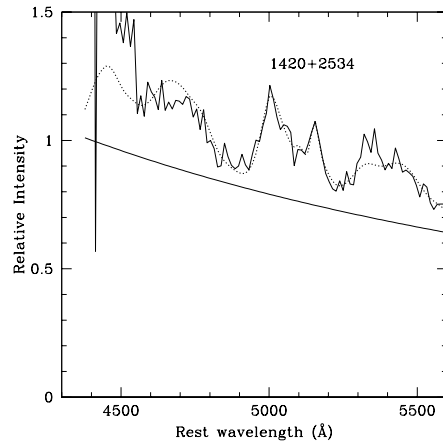
Figure B.1 UKIRT BAL QSOs

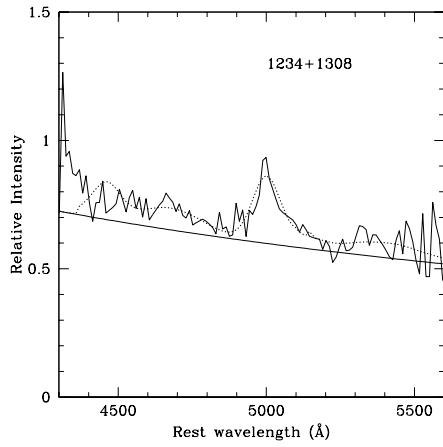Figure B.2 UKIRT BAL QSOs
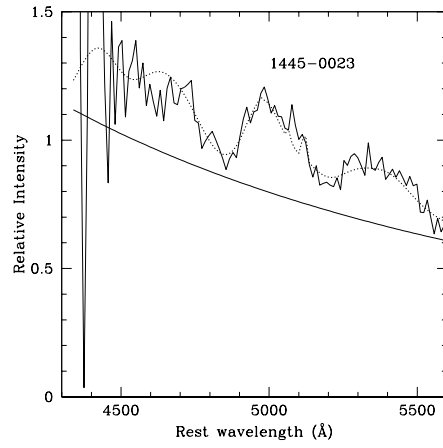
166

Figure B.3 UKIRT BAL QSOs
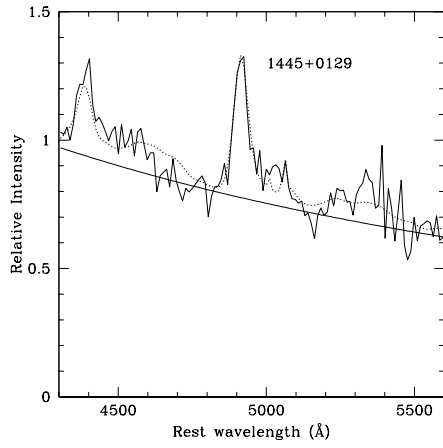

Figure B.4 UKIRT BAL QSOs
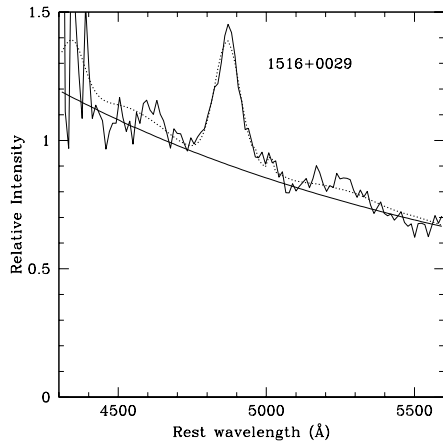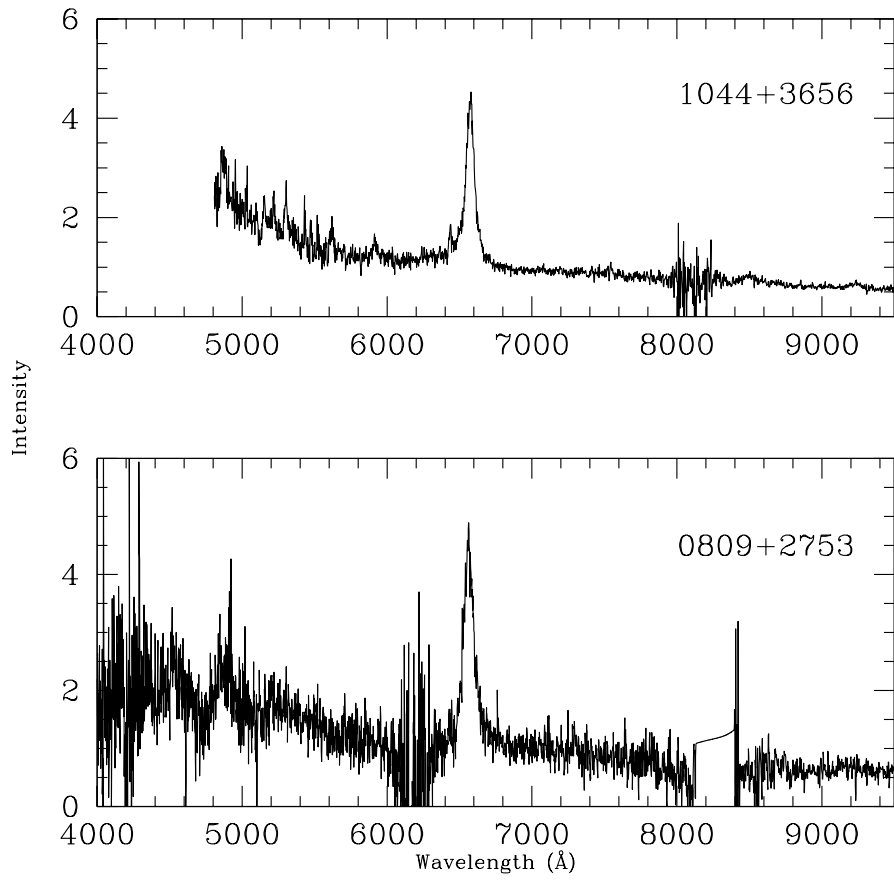
167

Figure B.5 UKIRT BAL QSOs

Figure B.6 UKIRT BAL QSOs

168

Figure B.7 IRTF SpeX reduced BAL QSO spectra
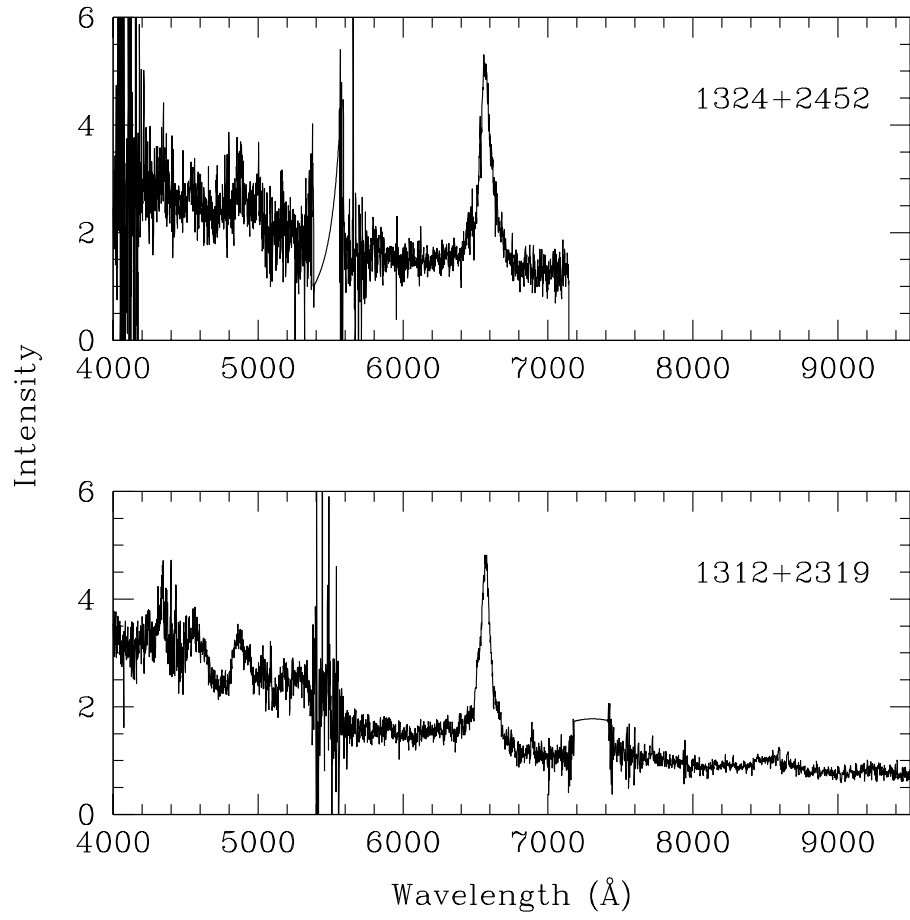
Figure B.8 IRTF SpeX reduced BAL QSO spectra

1408+3054

Intensity

Wavelength (Å)
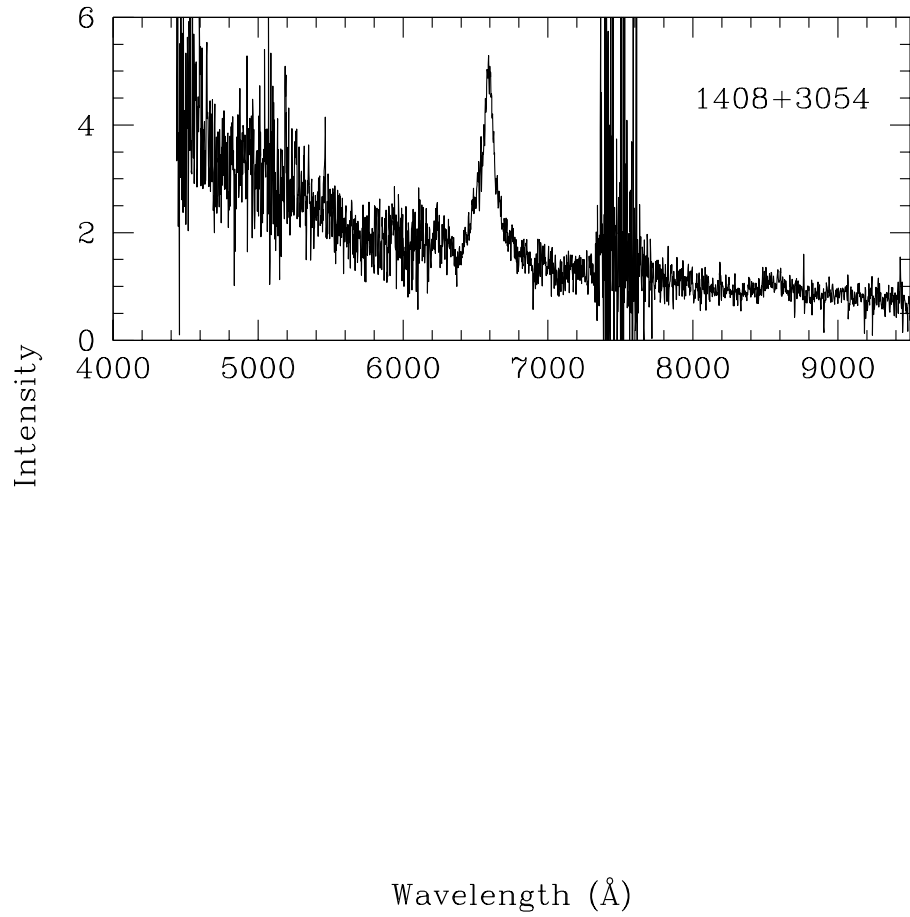
Figure B.9 IRTF SpeX reduced BAL QSO spectra

Appendix C

Eddington Ratio Selection Effects

The results in this thesis show that high luminosity QSOs tend to have high Eddington ratios. I have noted before the in chapter 4. that it is likely to caused by the limited range of black hole masses. High luminosity QSOs are produced by high black masses and high Eddington ratios. If the QSO number density decreases with increasing black hole mass, a large proportion of high luminosity QSOs would be created by medium black hole masses, which are readily available, and high Eddington ratios. In this section, I will analyze this problem in detail.

To model the observed distribution, I assume the following space density distribution of QSOs.

- At any given black hole mass M, the number of QSOs per unit volume (e.g., per Mpc^3) per unit mass is expressed by $\Theta(M)$.

- At any given Eddington ratio R, the number of QSOs per unit volume per unit Eddington ratio is expressed by $\Psi(R)$.

- The black hole mass and Eddington ratio is independent from each other.

Therefore, the QSO number density at M and R is expressed by

$$\Phi(M, R) = \Theta(M) \times \Psi(R).$$

Now, we need to find out the exact expressions for $\Theta(M)$ and $\Psi(R)$ respectfully.

From the Boroson and Green (1992) sample, I found that there are approximately the same number of QSOs in each logarithmic bin of Eddington ratio from R^{min} to R^{max}. I use the symbol Ψ' to denote the QSO density per $log(R)$ and hence have

$$\Psi'(R) = const$$

Between any R and $R + dR$, the number of QSOs is a fixed number:

$$\Psi(R) \times dR = \Psi'(R) * (log(R + dR) - log(R))$$

hence

$$\Psi(R) = \Psi'(R) \times \frac{d(log(R))}{dR},$$

$$\Psi(R) = const \times \frac{1}{ln(10)} \times \frac{1}{R}.$$

We can rewrite the above equation as

$$\Psi(R) = \frac{\Psi_0}{R}$$

C.0.1   QSO Number Density as a Function of Black Hole Mass

Corbett et al. (2003) gives the QSO space density per $log(M)$ (i.e., Θ') as a function of black hole mass and redshift. It seems that for all redshifts, the $log(\Theta')$ versus $log(M)$ distributions have a similar two-powerlaw shape:

173

- Below a certain "cut-off" mass M_0, the $log(\Theta')$ is approximately constant with regard to $log(M)$: $\Theta'(M) = const.$

- Above M_0, the $log(\Theta')$ versus $log(M)$ relationship follows a straight line with a slope of -1.823: $\Theta'(M) = const \times M^{-1.823}$.

Using the formulae I developed in the last section and considering that the two parts of Θ must join at $M = M_0$, we have

$$\Theta(M) = \frac{\Theta_0}{M} \, for \, M < M_0$$

and

$$\Theta(M) = \Theta_0 \times M_0^{1.823} \times \frac{1}{M^{2.823}} \, for \, M >= M_0$$

.

The value of the cut-off mass M_0 depends on the redshift.

Combining the formulae in the previous two sections and re-normalize them, we have the combined QSO number density function for any give Eddington ratio and black hole mass:

$$\Phi(M, R) = \frac{\Phi_0}{R \times M} \, for \, M < M_0, \tag{C.1}$$

and

$$\Phi(M, R) = \frac{\Phi_0 \times M_0^{1.823}}{R \times M^{2.823}} \, for \, M >= M_0. \tag{C.2}$$

174

At any given luminosity L, we select QSOs with a certain combination of black hole mass M and Eddington ratio R_{Edd} that satisfies the relationship

$$M_9 = \frac{L_{46}}{12.6 \cdot R_{Edd}}.$$

The $L = 10^{47} erg/s$ line is shown on Figure C.1 (the solid line) with the limits on R_{Edd} and the corresponding limits on M:

$$M_9^{min} = \frac{L_{46}}{12.6 \cdot R_{Edd}^{max}}$$

$$M_9^{max} = \frac{L_{46}}{12.6 \cdot R_{Edd}^{min}}.$$

As I had discussed before, we took values $R_{Edd}^{max} = 1.0$ and $R_{Edd}^{min} = 0.1$.

Between any given L and $L + dL$, we first calculate the total QSO number density:

$$U(L, dL) = \int_{R^{min}}^{R^{max}} \int_{\frac{L}{12.6R}}^{\frac{L+dL}{12.6R}} \Phi(M, R) dM dR. \tag{C.3}$$

Then, we can calculate a median value of R for that luminosity under the condition that $dL \to 0$:

$$\int_{R^{min}}^{R^{med}} \int_{\frac{L}{12.6R}}^{\frac{L+dL}{12.6R}} \Phi(M, R) dM dR = 0.5 \cdot U(L, dL). \tag{C.4}$$

Since the Eddington rate is a strictly decreasing function with regard to black hole mass when the luminosity is fixed, the median black hole mass corresponds to the median Eddington ratio.
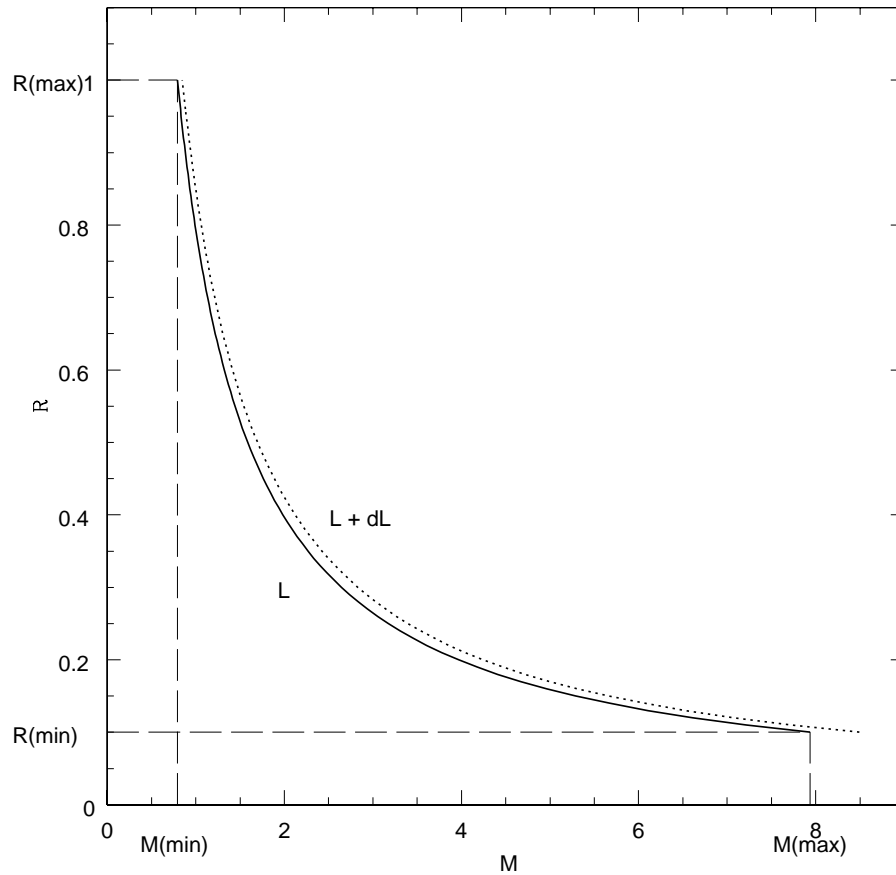
Figure C.1 The constant luminosity curve in the black hole mass versus Eddington ratio diagram. The integrated QSO number density in the area between the L line (the solid line) and the $L + dL$ line (the dashed line) is calculated.

$$M_9^{med} = \frac{L_{46}}{12.6 \times R_{Edd}^{med}}$$

If the selection luminosity of the sample is low enough that $M^{max} \leq M_0$, the QSO density distribution follows a single powerlaw described by equation C.1. We can solve for R_{med} analytically:

$$\int_{R_{min}}^{R} \int_{\frac{L}{12.6R}}^{\frac{L+dL}{12.6R}} \frac{\Phi_0}{MR} dM dR$$

$$= \Phi_0 \int_{R_{min}}^{R} \frac{1}{R} \cdot \ln\left(\frac{L+dL}{L}\right) dR$$

$$= \Phi_0 \ln\left(\frac{L+dL}{L}\right) \cdot \ln\left(\frac{R}{R^{min}}\right).$$

Combining the above with equations C.3 and C.4, we have

$$\ln\left(\frac{R^{med}}{R^{min}}\right) = 0.5 \times \ln\left(\frac{R^{max}}{R^{min}}\right).$$

That gives $R^{med} = 0.31$ for low luminosity samples. Note that this median Eddington ratio is not dependent on the actual value of the luminosity or the size of the luminosity bin used in the integration.

If the sample QSOs have a high enough luminosity that the entire black hole mass range is above the cut-off mass (i.e. $M_{min} \geq M_0$), the QSO number density function again falls into a complete single powerlaw domain described by equation C.2. Integrate Φ between L and $L + dL$, we have

$$\int_{R_{min}}^{R} \int_{\frac{L}{12.6R}}^{\frac{L+dL}{12.6R}} \frac{\Phi_0 \times M_0^{1.823}}{R \times M^{2.823}} dM dR$$

$$= \Phi_0 \times M_0^{1.823} \times \int_{R_{min}}^{R} \frac{1}{R} \cdot \left[\left(\frac{L}{12.6R} \right)^{-1.823} - \left(\frac{L+dL}{12.6R} \right)^{-1.823} \right] \cdot dR$$

$$= const \times [L^{-1.823} - (L+dL)^{-1.823}] \cdot \int_{R_{min}}^{R} R^{0.823} dR$$

$$= const \times [L^{-1.823} - (L+dL)^{-1.823}] \cdot (R^{1.823} - R_{min}^{1.823})$$

Combine the above with equations C.3 and C.4, and eliminate the constant and L related terms on both sides of the equation, we have

$$R_{med}^{1.823} - R_{min}^{1.823} = 0.5 \times (R_{max}^{1.823} - R_{min}^{1.823}).$$

That gives $R_{med} = 0.68$ regardless of the actual value of L and dL in this region.

So far, I have demonstrated that at high or low luminosities, where the underlying QSO number density distributions follow single powerlaws, the median Eddington ratio are constants. The value of the constant is determined by the underlying powerlaw index. However, if the sample luminosity is intermediate, we will select objects from both sides of M_0 and hence get an underlying distribution of two powerlaws. That made it impossible to simply eliminate L related terms in equation C.4. Therefore, R_{med} depends on the selection luminosity of the sample.

Although it is possible to solve for R_{med} against L analytically in this region, we need to divide the luminosity into many small ranges to accommodate the different relative positions of M_{min}, M_{max} and M_{med} against M_0. I

178

found that numerical integration is much more straightforward. For each set of L, R^{min} and R^{max} values, the right hand side of equation C.4 is a fixed value and the left hand side of the equation is a strictly increasing function with R^{med}. So, it is easy to solve for R^{med} using numerical methods.

I wrote a computer program to calculate the R_{med} against L for different QSO distribution models with different M_0 ($10^8 M_\odot$, $5 \times 10^8 M_\odot$, $10^9 M_\odot$ and $5 \times 10^9 M_\odot$). The results are presented in figure C.2. The two dots are the mean Eddington ratios from the $\log(L) < 10^{47}$ erg/s QSOs and the $\log(L) > 10^{47}$ erg/s QSOs in our sample (section 4.1.5). The corresponding median black hole mass against luminosity for those models are presented in figure C.3.

As expected, higher black hole mass are selected at higher luminosity. Also in this model, higher Eddington ratio objects are also selected at higher luminosity to make up for the shortage of high mass objects. As a result of the luminosity selection effect, both black hole mass and Eddington ratio now increase with luminosity when the luminosity is high.
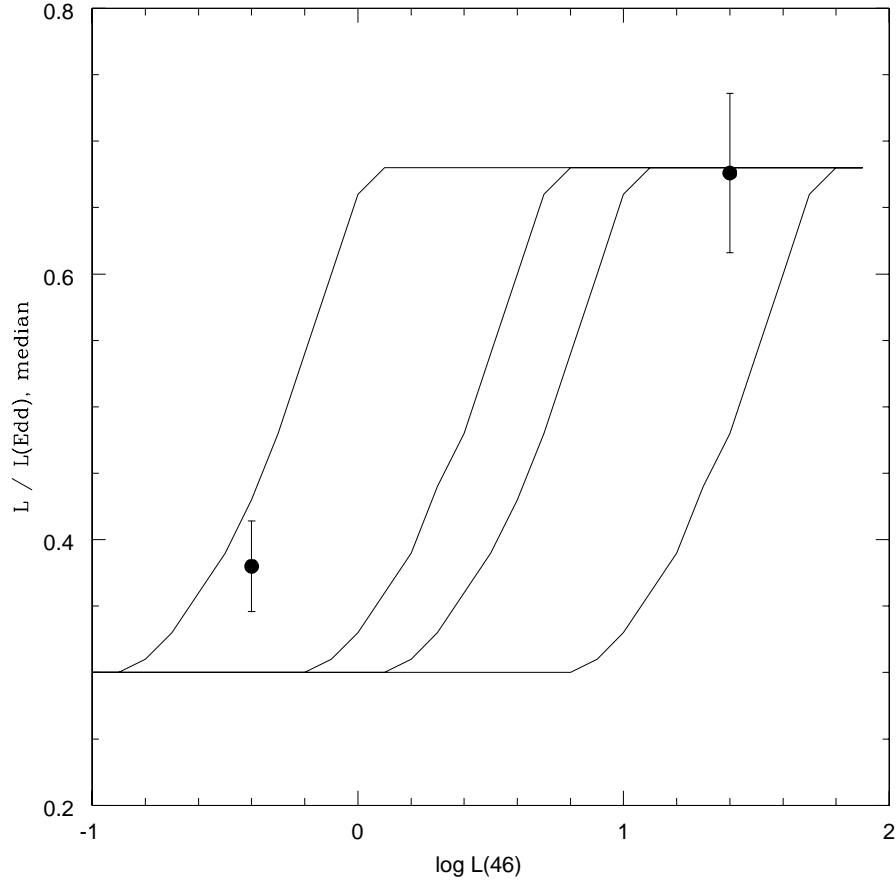
Figure C.2 The median Eddington ratio for QSO samples selected at different luminosity. The lines are calculated from models with different cut-off masses. From left to right, the cut off masses in the model are $10^8 M_\odot$, $5 \times 10^8 M_\odot$, $10^9 M_\odot$ and $5 \times 10^9 M_\odot$. The two dots are the mean Eddington ratios from the low and high luminosity QSOs in the QSO sample used in this thesis.
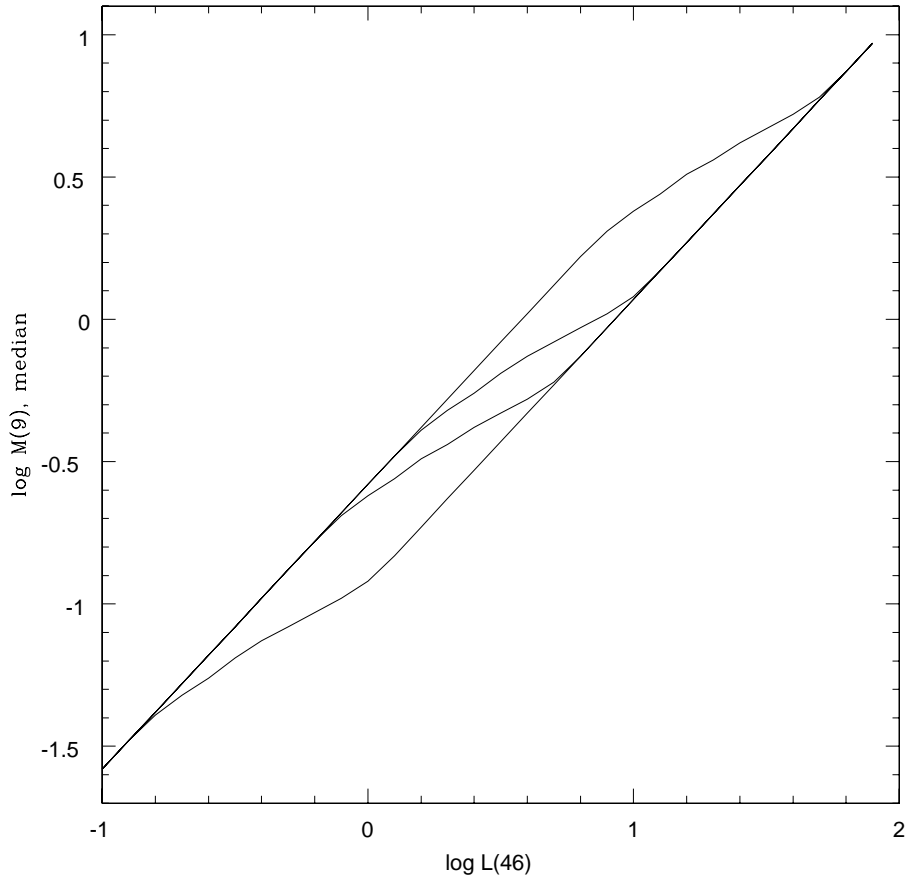
Figure C.3 The mean black hole mass for QSO samples selected at different luminosity. The lines are calculated from models with different cut-off masses. From left to right, the cut off masses in the model are $10^8 M_\odot$, $5 \times 10^8 M_\odot$, $10^9 M_\odot$ and $5 \times 10^9 M_\odot$

Bibliography

Alexander, T. & Netzer, H. 1994, MNRAS270, 803

Arav, N., Li, Z. Y., & Begelman, M. C. 1994, ApJ, 432, 62

Arav, N. 1997, in ASP Conf. Ser. 128, Mass Ejection from Active Galactic Nuclei, ed. N. Arav, I. Shlosman & R. J. Weymann (San Francisco: ASP), 264

Arav N., Barlow T.A., Laor A., Sargent W.L.W. & Blandford R.D. 1998, MNRAS, 297, 990

Avni, Y. 1976, ApJ, 210, 642

Baldwin, J. A. 1977, ApJ, 214, 679

Baldwin, J., Ferland, G., Korista, K. & Verner, D. 1995, ApJ, 455, L119

Baldwin, J. A., Wampler, E. J., & Gaskell, C. M. 1989, ApJ, 338, 630

Baldwin,J.A., Ferland,G.J., Korista,K.T., Carswell,R.F. et al. 1996, ApJ, 461, 664

Baskin, A. & Laor, A. 2004, MNRAS, 350, L31

Becker, R. H., White R. L., Gregg, M. D., Brotherton, M. S. et al. 2000, ApJ, 538, 72

Benn, C. R., Grueff, G., Vigotti, M. & Wall, J. V. 1988, MNRAS, 230, 1

Boroson, T. A. 2002, ApJ, 565, 78

Boroson, T. A., & Green, R. F. 1992, ApJS, 80, 109 (BG92)

Boroson, T. A., & Meyers, K. A. 1992, ApJ, 397, 442

Boisse, P., Boulade, O., Kunth, D., Tytler, D. & Vigroux, L. 1992, A&A, 262, 401

Brotherton, M. S., Wills, B. J., Francis, P. J. & Steidel, C. C. 1994, ApJ, 430, 495

Brotherton, M. S. 1996, ApJS, 102, 1

Brotherton, M. S. 2004, in preparation

Collin, S., Boisson, C., Mouchet, M., Dumont, A. M. et al. 2002, A&A, 388, 771

Corbett, E. A., Croom, S. M., Boyle, B. J., Netzer, H. et al. 2003, MNRAS, 343, 705

Croom, S. M., Rhook, K., Corbett, E. A., Boyle, B. J. et al. 2002, MNRAS, 337, 275

Dietrich,M., Wagner,S.J., Courvoisier,T.J.-L., Bock,H. & North,P. 1999, A&A, 351, 31

Dietrich, M., Appenzeller, I., Vestergaard, M., & Wagner, S. J. 2002, ApJ, 564, 581

Done, C., Pounds, K. A., Nandra, K., & Fabian, A. C. 1995, MNRAS, 275, 417

Eckart, A. & Genzel, R. 1997, MNRAS, 284, 576

Genzel, R., Eckart, A., Ott, T. & Eisenhauer, F. 1997, MNRAS, 291, 219

Elvis, M. 2000, ApJ, 545, 63

Elvis, M., Wilkes, B. J., McDowell, J. C., Green, R. F. et al. 1994, ApJS, 95, 1

Espey, B. R., & Andreadis, S. 1999, in ASP Conf. Ser. 162, Quasars and Cosmology, ed. G. J. Ferland & J. A. Baldwin (San Francisco: ASP), 351

Fabian, A. C. 1999, MNRAS, 308, L39

Ferland, G. J., Peterson, B. M., Horne, K., Welsh, W. F. & Nahar, S. N. 1992, ApJ, 387, 95

Ferland, G. J. & Baldwin, J. A., eds. 1999, ASP Conf. Series 162, Quasars and Cosmology (San Francisco: ASP)

Francis, P. J., Hooper, E. J. & Impey, C. D. 1993, AJ, 106, 417

Freedman, W. 2002, Int. J. Mod. Phys., A17S1, 58

Foltz, C. B., Weymann, R. J., Morris, S. L. & Turnshek, D. A. 1987, ApJ, 317, 450

Foltz, C. B., Chaffee, F. H., Hewett, P. C., Weymann, R. J. & Morris, S. L. 1990, BAAS, 22, 806

Gallagher,S.C., Brandt,W.N., Chartas,G. & Garmire,G.P. 2002, ApJ, 567, 37

Gebhardt, K., Kormendy, J., Ho, L. C., Bender, R. et al. 2000, ApJ, 543, 5L

Goad, M. R., Korista, K. T. & Knigge, C. 2004, MNRAS, to be published

Goodrich, R. W. 1990, ApJ, 355, 88

Green P.J., Forster K., Kuraszkiewicz J., 2001, ApJ, 556, 727

Green, P. J., Aldcroft, T. L., Mathur, S., Wilkes, B. J. & Elvis, M. 2001, ApJ, 558, 109

Grupe, D., Beuermann, K., Mannheim, K., & Thomas, H.-C. 1999, A&A, 350, 805

Haehnelt, M. G., Natarajan, P. & Rees, M. J. 1998, MNRAS, 300, 817

Hall, P. B., Anderson, S. F., Strauss, M. A., York, D. G. et al. 2002, ApJS, 141, 267

Hamann,F., Korista,K.T. & Morris,S.L. 1993, ApJ, 415, 541

Hamann,F., Sabra,B., Junkkarinen,V., Cohen,R. & Shields,G. 2002, Workshop on X-ray Spectroscopy of AGN with Chandra and XMM-Newton, MPE Report 279, 121

Hewett, P. C. & Foltz, C. B. 2003, AJ, 125, 1784

Hines,D.C. & Wills,B.J. 1995, ApJ, 448, L69

Joly, M., Collin-Souffrin, S., Masnou, J. L. & Nottale, L. 1985, A&A, 152, 282

Kaspi, S., Smith, P. S., Netzer, H., Maoz, D. et al. 2000, ApJ, 533, 631

Kellermann, K. I., Sramek, R., Schmidt, M., Shaffer, D. B. & Green, R. 1989, AJ, 98, 1195

Kinney, A. L., Rivolo, A. R. & Koratkar, A. P. 1990, ApJ, 357, 338

Korista, T. K., Voit, G. M., Morris, S. L. & Weymann, R. J. 1993, ApJS, 88, 357

Korista, K. T., Baldwin, J. A., & Ferland, G. J. 1998, ApJ, 507, 24

Korista, K. T. 1999, in ASP Conf. Series 162, Quasars and Cosmology, ed. G. J. Ferland, & J. A. Baldwin (San Francisco: ASP), 429

Koski, A. T. 1978, ApJ, 223, 56

Kriss, G. 1994, in ASP Conf. Ser. 61, Astronomical Data Analysis Software and Systems III, ed. D. R. Crabtree, R. J. Hanisch, & J. Barnes (San Francisco: ASP), 437

Krolik J.H., McKee C.F. & Tarter C.B. 1981, ApJ, 249, 422

Krolik J. H. 2001, ApJ, 551, 72

Lacy M., Laurent-Muehleisen S.A., Ridgway S.E., Becker R.H., & White R.L., 2001, ApJ, 551, L17

Laor, A. & Draine, B. T. 1993, ApJ, 402, 441

Laor, A., Fiore, F., Elvis, M., Wilkes, B. J., & McDowell, J. C. 1994, ApJ, 435, 611

Laor, A., Fiore, F., Elvis, M., Wilkes, B. J., & McDowell, J. C. 1997, ApJ, 477, 93

Laor, A. 1998, ApJ, 505, L83

Laor, A. 2000, ApJ, 543, L111

Laor, A. & Brandt, W. N. 2002, ApJ, 569, 641

Lin, D. N. C. & Shields, G. A. 1986, ApJ, 305, 28

Low, F. J., Cutri, R. M., Huchra, J. P. & Kleinmann, S. G. 1988, ApJ, 327, L41

Marconi,A., Risaliti,G., Gilli,R., Hunt,L.K., Maiolino,R. & Salvati,M. 2004, MNRAS, 351, 169

McGowan, K. E., Priedhorsky, W. C. & Trudolyubov, S. P. 2004, ApJ, 601, 1100

McIntosh, D. H., Rieke, M. J., Rix, H. W., Foltz, C. B. & Weymann, R. J. 1999, ApJ, 514, 40

McIntosh, D. H., Rix, H.-W., Rieke, M. J., & Foltz, C. B. 1999b, ApJ, 517, L73

McLure, R. J. & Dunlop, J. S. 2001, MNRAS, 327, 199

Meyer, F., & Meyer-Hofmeister, E. 1981, A&A, 104, L10

Mushotzky, R. & Ferland, G. J. 1984, ApJ, 278, 558

Murray, N., Chiang, J., Grossman, S. A. & Voit, G. M. 1995, ApJ, 451, 498

Murray, N., & Chiang, J. 1997, ApJ, 474, 91

Murray, N., & Chiang, J. 1998, ApJ, 494, 125

Narayan, R., McClintock, J. E. & Yi, I. 1996, ApJ, 457, 821

Nelson,C.H. & Whittle,M. 1996, ApJ, 465, 96

Netzer H., 1990, In: Blandford R.D., Netzer H., Woltjer L. (eds.) Saas-Fee
Advanced Course 20: Active Galactic Nuclei. Springer, New York, 57

Netzer,Hagai, Laor,Ari & Gondhalekar,P.M. 1992, MNRAS, 254, 15

Netzer, H. 2003, ApJ, 583, L5

Neugebauer, G., Green, R. F., Matthews, K., & Schmidt, M. et al. 1987, ApJS,
63, 615

Neugebauer, G., Soifer, B. T., Matthews, K., & Elias, J. H. 1989, AJ, 97, 957

Nowak, M. A. 1995, PASP, 107, 1207

Ogle,P.M., Cohen,M.H., Miller,J.S., Tran,H.D., Goodrich,R.W. and Mar-
tel,A.R. 1999, ApJS, 125, 1

Osterbrock, D. E. 1979, AJ, 84, 901

Padovani, P. & Urry, C. M. 1992, ApJ, 387, 449

Peterson, B. M., Meyers, K. A., Carpriotti, E. R., Foltz, C. B. et al. 1985,
ApJ, 292, 164

Peterson, B. M. 1997, An Introduction to Active Galactic Nuclei, (United
Kingdom: Cambridge University Press)

Peterson, B. M. & Wandel, A. 1999, ApJ, 521, 95L

Peterson,B.M. & Horne,K. 2004, Astronomische Nachrichten, 325, 248

Pogge, R. W. 1989, ApJ, 345, 730

Pogge R. W. & Peterson B. M. 1992, AJ, 103, 1084

Popovic, L. C. 2003, ApJ, 599, 140

Rees M. J. 1987, MNRAS, 228, 47

Rees, M. J., Netzer, H. & Ferland, G. J. 1989, ApJ, 347, 640

Reichard, T. A., Richards, G. T., Hall, P. B., Schneider, D. P. et al. 2003, AJ,
126, 2594

Reichard, T. A., Richards, G. T., Schneider, D. P., Hall, P. B. et al. 2003, AJ,
125, 1711

Rokaki, E., Boisson, C., & Collin-Souffrin, S. 1992, A&A, 253, 57

Schmidt, G. D. & Hines, D. C. 1998, ApJ, 512, 125

Sergeev, S. G., Pronik, V. I., Sergeeva, E. A. & Malkov, Y. F. 1999, AJ, 118,
2658

Shakura, N. I., & Sunyaev, R. A. 1973, A&A, 24, 337

Shang, Z., Wills, B. J., Robinson, E. L., Wills, D. et al. 2003, ApJ, 586, 52

Shields, G. A. 1978, Nature, 272, 706

Shields, G. A., Gebhardt, K., Salviander, S., Wills, B. J. et al. 2003, ApJ, 583,
124

Siemiginowska, A., Czerny, B., & Kostyunin, V. 1996, ApJ, 458, 491

Smith, H. J. & Hoffleit, D. 1963, Nature, 198, 650

Sprayberry, D. & Foltz, C. B. 1992, ApJ, 390, 39

Sramek,R.A. & Weedman,D.W. 1978, ApJ, 221, 468

Steidel, C. C. & Sargent, W. L. W. 1992, ApJS, 80, 1

Steiner, J. E. 1981, ApJ, 250, 469

Stirpe, G. M. 1991, A&A, 247, 3

Stocke, J. T., Morris, S. L., Weymann, R. J. & Foltz C. B. 1992, ApJ, 396, 487

Strecker, D. W., Erickson, E. F. & Witteborn, F. C. 1979, ApJS, 41, 501

Terlevich, R., Tenorio-Tagle, G., Franco, J. & Melnick, J. 1992, MNRAS, 255, 713

Tolea, A., Krolik, J. H., & Tsvetanov, Z. 2002, ApJ, 578, L31

Turnshek, D. A. 1987, in QSO Absorption Lines: Probing the Universe ed. J. C. Blades, D. Turnshek, & C. Norman (Cambridge: Cambridge University Press)

Turnshek, D. A., Monier, E. M., Sirola, C. J. & Espey, B. R. 1997, ApJ, 476, 40

Vanden Berk, D. E., Richards, G. T., Bauer, A., Strauss, M. A. 2001, AJ, 122, 549

Veilleux, S., & Osterbrock, D. E. 1987, ApJS, 63, 295

Veron-Cetty,M.-P., Veron,P. & Gonalves,A.C. 2001, A&A, 372, 730

Vestergaard, M. 2002, ApJ, 571, 733

Voit, G. M., Weymann, R. J. & Korista, K. T. 1993, ApJ, 413, 95

Wampler, E. J. 1983, A&A, 122, 54

Wang, J. M. 2003, AJ, 125, 2859

Wandel, A. 1999, ApJ, 527, 649

Wandel, A., Peterson, B. M. & Malkan, M. A. 1999, ApJ, 526, 579

Weymann, R. J., Morris, S. L., Foltz, C. B. & Hewett, P. C. 1991, ApJ, 373, 23

White, R. L., Becker, R. H., Helfand, D. J., & Gregg, M. D. 1997, ApJ, 475, 479

Wills, B. J., Netzer, H. & Wills, D. 1985, ApJ, 288, 94

Wills, B. J. & Browne, I. W. A. 1986, ApJ, 302, 56

Wills, B. J. & Hines, D. C. 1997, Mass Ejection from Active Galactic Nuclei, ASP Conference Series, 128, 99

Wills, B. J., Laor, A., Brotherton, M. S., Wills, D., Ferland, G. J., & Shang, Z. 1999, ApJ, 515, L53

Woo, J-H. & Urry, C. M. 2002, ApJ, 579, 530

Yuan, F., Markoff, S., Falcke, H. & Biermann, P. L. 2002, A&A, 391, 139

Yuan, M. J., Tran, H., Wills, B. J. & Wills, D. 2001, Blazar Demographics and Physics, ASP Conference Series, Vol. 227. Edited by Paolo Padovani and C. Megan Urry. San Francisco: Astronomical Society of the Pacific.

Vita

Juntao Yuan was born in Chengdu, Sichuan Province, China on November 24, 1974, to Chengchang Yuan and Ming Zhang. After graduating from Chengdu Shishi High School in 1992, he entered Nanjing University, China. There he received a B.Sc. in Astrophysics in 1996. In 1997, he chose to attend The University of Texas at Austin and moved to the US to pursue a Ph.D. in Astronomy. He was also a teaching assistant and a research assistant in the Astronomy Department. He received a M.A. in Astronomy in 1999.

Permanent address: 1628 W 6th St K
Austin, Texas 78703

This dissertation was typeset with LaTeX[†] by the author.

[†]LaTeX is a document preparation system developed by Leslie Lamport as a special version of Donald Knuth's TeX Program.